University of Alberta

Intrinsic Disorder Effects and Persistent Current Studies of $YBa_2Cu_3O_{7-\delta}$ Thin Films and Superconducting Tunnel Junctions

by

Ahmad Ibrahim Mansour

A thesis submitted to the Faculty of Graduate Studies and Research
in partial fulfillment of the requirements for the degree of

Doctor of Philosophy

Department of Physics

Fall 2009
Edmonton, Alberta

Examining Committee

Prof. Kim H. Chow, Physics

Prof. Jan A. Jung, Physics

Prof. Frances Fenrich, Physics

Prof. Moritz Heimpel, Physics

Prof. Thomas H. Etsell, Chemical and Materials Engineering

Prof. David K. Christen, Superconductive and Energy Efficient Materials, Materials Science and Technology Division,Oak Ridge National Laboratory, Oak Ridge, TN 37831 USA

To

My Family

Abstract

This thesis studies the intrinsic disorder effects and the transport and magnetic properties of ring-shaped epitaxial thin films and superconducting tunnel junctions (STJs) of the high temperature superconductor $YBa_2Cu_3O_{7-\delta}$. We used an unconventional contactless technique that allows us to directly measure the persistent current of superconducting rings.

In order to study the disorder effects on the persistent current, we slowly increased oxygen vacancies in $YBa_2Cu_3O_{7-\delta}$ by changing δ from 0.03 to 0.55 in steps of $\sim$0.021. Monitoring the corresponding changes in the temperature dependence of the persistent current revealed an anomaly in its flow within a certain range of disorder. We found that this anomaly is directly related to the occurrence of a spinodal decomposition of oxygen vacancies in YBCO, which we explain as a competition between two coexisting phases, oxygen rich and oxygen deficient. The analysis of the time dependence of the persistent current revealed that increasing oxygen vacancies transforms the vortex structure from quasi-lattice into a glass and subsequently into a pinned liquid phase. Our results also exhibited the first evidence of self-organization of the vortex structure with increasing disorder.

We also performed the first direct measurement of the temperature dependence of the *c*-axis persistent current (J_c) that is purely due to tunnelling Cooper-pairs through intrinsic Josephson junctions (IJJs) of YBCO. This is made possible by incorporating IJJs of YBCO into ring-shaped films. Then, we studied the temperature dependence of the persistent current of YBCO nanowires embedded in $SrTiO_3$-barrier

integrated between two semi-ring-shaped YBCO thin films and systematically varied the nanowires length. Our observations revealed that J_c has two different temperature dependences: a GL-dependence ($J_c \propto (T_c - T)^{3/2}$) at low temperatures which we found the same in all studied samples, and another power law dependence ($J_c \propto (T_c - T)^{\alpha > 3/2}$) at high temperatures which turned out to depend on the length of the nanowires. We attribute the cross-over between these two temperature dependences to the depinning and the dissipative motion of vortices.

These experimental approaches and findings not only provide new information, but more importantly open new avenues of investigating the transport and magnetic properties of superconducting films, junctions, and nanowires.

ACKNOWLEDGEMENT

I would like to express my deep and special gratitude to my supervisor Prof. Kim Chow for his support, fruitful discussions, patience, and guidance in all my PhD research studies, and especially in the part of my research related to β-NMR and μ-SR which was a completely new field for me (not included in this thesis). Also I would like to thank him for his financial support.

I would also like to thank Prof. Jan Jung with whom I performed the research work presented in this thesis. In particular, I would like to thank him for his support and fruitful discussions in the part of my research that was related to superconductivity. In fact, his deep understanding of superconductivity greatly enriched my knowledge of this exciting field of study. Great thanks goes to all the research group members with whom I worked at the University of Alberta: Mehmet Egilmez, Rongchao Ma, Isaac Fan, and Mohamed El-Sayed for their contributions during the course of this thesis.

Also I would like to specially thank Dr. Isaac Isaac (Director of Physics Undergraduate Labs) for his invaluable and very helpful supervision of my teaching experience at the University of Alberta.

I would like to express my gratitude to Professor Vadim Kravchinsky and to my committee members: Prof. Moritz Heimpel, Prof. Frances Fenrich, and Prof. Thomas Etsell from the University of Alberta and Prof. David Christen from Oak Ridge National Laboratory, for their comments and suggestions on my research and thesis.

Very special thanks goes to Prof. Robert Kiefl and Prof. Andrew MacFarlane for their valuable help and guidance throughout my β-NMR research work that I did at TRIUMF in Vancouver. I would like to say many thanks to Dr. Gerald Morris, Dr. Zaher Salman, Dr. Bassam Hitti, and all the staff, faculty, and students for their help

and for the great time that we spent together while I was working in TRIUMF.

I would like to thank Prof. Sharon Morsink and Ms. Sarah Derr for their friendly, helpful, and excellent administrative assistance and advice.

Also, I would like to thank Mr. Donald Mullin, Mr. Greg Popowich, Mr. Tony Walford, and Mr. Bill Burris for their valuable technical support. I would like to extend my thanks to all Physics department staff, faculty, and students who have helped me directly and indirectly during my graduate studies.

Finally, I would like to thank my parents and my two brothers for their great love and endless support during all the stages of my studies.

Contents

List of Tables

List of Figures

Chapter 1

Introduction: Motivations and Goals

Superconductivity is a phenomenon that takes place at temperatures below a critical temperature T_c, and is characterized by zero electrical resistance and the exclusion of an external magnetic field from the interior of the superconducting material. The charge carriers in the superconducting state are Cooper pairs, which consist of pairs of bound electrons flowing without electrical resistance. Superconductivity was first discovered in 1911 by H. K. Onnes in mercury at $T_c = 4.2$ K. In 1986 Bednorz and Müller [1] discovered high temperature superconductors (HTSC) with $T_c > 30$ K, thus stimulating extraordinary experimental and theoretical research activities. The goal of these studies is not only to understand the basic mechanism leading to this exotic phenomenon, but also to improve the suitability of the superconducting properties of these materials for technological purposes. Superconducting thin films and tunnel junctions are inherent of a wide variety of applications such as, single photon detectors, superconducting quantum interference devices (SQUIDs), high magnetic field superconducting magnets, very high resolution x-ray sensors, quantum computing,

and terahertz imaging [2, 3, 4, 5]. The superconducting properties of interest in these systems include the transport critical current density (J_c), the dynamics and the pinning mechanism of the vortex matter, and the transition temperature (T_c); J_c is the maximum current that can be carried by a superconductor at a given temperature below T_c. Epitaxial thin-films constitute the most important form of superconductors for such technological purposes because of the flexibility they offer in devising different forms of thin films and hetrostructures, and because of their capacity to carry high critical currents compared to the bulk form. For example, an epitaxial thin film of $YBa_2Cu_3O_{7-\delta}$ (YBCO), a high temperature superconductor, can carry a critical current density $\sim 10^5$ A/cm^2 at 77 K. This is three orders of magnitude larger than the bulk form of YBCO which can handle only 10^2 A/cm^2 at similar temperature. Such a large critical current density exerts strong forces (Lorentz forces) on the magnetic vortices driving them into motion, hence causing suppression of the supercurrent through dissipation [6]. Lattice defects, however, can pin these vortices and thus hinder their dissipative motion, deform the vortex structure, and increase the critical currents. Of the many types of lattice defects, oxygen vacancies are of special importance because they are intrinsic to cuprate superconductors such as YBCO, the main material studied in this thesis.

Among the many interesting aspects of oxygen vacancies in HTSC films are their ordering tendency and their effects on the temperature dependence of the critical current. It was shown that [7] the temperature dependence of the critical current density J_c in YBCO has a Ginzburg-Landau-like (GL-like) dependence [8],

i.e. $J_c(T) \propto (1 - T/T_c)^{3/2}$, at low temperatures, and exhibits a cross-over to an Ambegaokar-Baratoff (AB) dependence at higher temperatures. The GL-like dependence was found to be related to the percolative flow of the critical current along meandered pathways, and to dominate in slightly more oxygen deficient films of YBCO [7]. It is also known that increasing the concentration of oxygen vacancies in YBCO reduces its hole doping, and consequently reduces the magnitude of the supercurrent [9, 10, 11]. Transmission electron microscopy (TEM) and magnetic hysteresis measurements of YBCO single crystals [12, 13, 14, 15], revealed that oxygen vacancies are ordered in clusters. This raises a major question regarding the interplay between oxygen vacancies, their ordering, and the flow of the critical current as the superconducting system approaches the strongly oxygen deficient limit.

Another important aspect of oxygen vacancies (disorder) is manifested by their significant effects on the vortex structure of HTSCs [9]. In defect-free superconductors, vortices arrange themselves in the form of a triangular lattice structure, known as Abrikosov lattice [16]. In oxygen deficient superconductors, oxygen vacancies act as weak pinning centers for the magnetic vortices, thus deforming the vortex structure. Previous studies of different YBCO samples [10, 11] with different concentration of disorder (different oxygen contents) reported no changes in the vortex structure, which seems to contradict existing theoretical predictions [9]. In fact, oxygen vacancies are not just expected to induce changes in the vortex structure, but more importantly, the vortex matter is believed to exhibit self-organization in the non-stationary state [17]. An important and necessary condition for the observation of

self-organization is to slowly advance the system through the disordered state [18, 19], which is an experimentally challenging task, and has not been reported yet. This motivates the search for new ways to overcome such a challenge, and subsequently to address the controversy regarding the correlation between the oxygen content and the vortex structure.

In addition to the resistance-less flow of the Cooper pairs which creates the supercurrent, Cooper pairs also exhibit another interesting behavior which is tunnelling across thin barriers, where these barriers can be natural or artificial. Superconducting systems with natural barriers are known as intrinsic Josephson junctions (IJJs), an example of which are the cuprate superconductors where the barriers arise from the weak coupling between the CuO_2 planes. As for artificial barriers, they can be found in superconducting tunnel junctions (STJs) which consist of insulating, normal, or semiconducting layers embedded between two superconducting electrodes. Whether a supercurrent tunnels through either natural or artificial barriers, both Cooper pairs and quasi-particles (broken Cooper pairs) are involved in the tunnelling process. While the tunneling of Cooper pairs and quasiparticles has been previously studied in single crystals of $Bi_2Sr_2CaCu_2O_{8+x}$ (BSCCO) [20] and thin films of $YBa_2Cu_3O_{7-\delta}$ (YBCO) [21, 22] using the four-probe transport method, this experimental method cannot separate the Cooper pairs tunnelling contribution from that of the quasiparticles tunnelling to the observed critical current [23, 24]. In fact, previous attempts at fabricating junctions that enable one to observe tunnelling of the Cooper pairs only were not successful [25]. This makes it significantly important to devise a

method that enables the study of currents which are solely due to the Cooper-pairs' tunnelling.

In this thesis, we successfully address all the above mentioned challenges as follows:

1. We investigate the effect of oxygen vacancies and their ordering on the flow of the persistent current in YBCO thin films.

2. We investigate the intrinsic disorder effects and the self-organization of the vortex structure of YBCO thin films.

3. We devise a special form of YBCO superconducting rings that allows us to measure the *c*-axis persistent current. This enables us to investigate the temperature dependence of the *c*-axis persistent current and the tunneling of Cooper pairs across intrinsic Josephson junctions of YBCO.

4. We investigate the temperature dependence of the persistent critical current of YBCO nanowires embedded in $SrTiO_3$-barrier integrated between two semi-ring-shaped YBCO thin films, and systematically vary the nanowires length.

The remaining part of this thesis is organized as follows. First a brief theoretical background related to our experimental observations is given in Chapter 2. The details of our experimental-setup and sample preparation method are presented in Chapter 3. In Chapters 4 and 5, we present our observations of the effects of oxygen vacancies and their ordering on the flow of the persistent current and on the vortex structure. Finally, the studies of the Cooper pairs' tunnelling through intrinsic

Josephson junctions of YBCO and through YBCO superconducting nanowires embedded in $SrTiO_3$ (STO) layer integrated between two semi-ring-shaped YBCO thin films are presented in Chapters 6 and 7. A summary of our findings is given in Chapter 8, and the Appendix contains an experimental study of the effects of disorder (magnesium deficiency) on the transport properties of MgB_2 superconducting rings.

Bibliography

[1] J. G. Bednorz and K. A. Müller, Z. Phys. B **64**, 189 (1986).

[2] L. Frunzio, L. Li, D. E. Prober, I. V. Vernik, M. P. Lisitskii, C. Nappi, and R. Cristiano, Appl. Phys. Lett. **79**, 2103 (2001).

[3] N. A. Miller, G. C. ONeil, J. A. Beall, G. C. Hilton, K. D. Irwin, D. R. Schmidt, L. R. Vale, and J. N. Ullom, Appl. Phys. Lett. **92**, 163501 (2008).

[4] M. Mück, M. Korn, C. G. A. Mugford, J. B. Kycia, J. Clarke, Appl. Phys. Lett. **86**, 012510 (2005).

[5] S. Ariyoshi, C. Otani, A. Dobroiu, H. Sato, K. Kawase, H. M. Shimizu, T. Taino, and H. Matsuo, Appl. Phys. Lett. **88**, 203503 (2006).

[6] Y. B. Kim, C. F. Hempstead, and A. R. Strnad, Phys. Rev. **139,** A1163 (1965).

[7] H. Darhmaoui and J. Jung, Phys. Rev. B **57,** 8009 (1998).

[8] J. R. Clem, B. Bumble, S. I. Raider, W. J. Gallagher, and Y. C. Shih, Phys. Rev. B **35,** 6637 (1987).

[9] G. Blatter, M. V. Feigel'man, V. B. Geshkenbein, A. I. Larkin, and V. M. Vinokur, Rev. Mod. Phys. **66,** 1125 (1994).

[10] J.G. Ossandon, J. R. Thompson, D. K. Christen, B. C. Sales, H. R. Kerchner, J. O. Thomson, Y. R. Sun, K. W. Lay and J. E. Tkaczyk, Phys. Rev. B **45**, 12534 (1992).

[11] J.G. Ossandon, J. R. Thompson, D. K. Christen, B. C. Sales, Yangren Sun, and K. W. Lay, Phys. Rev. B **46**, 3050 (1992).

[12] J.L. Vargas and David C. Larbalestier, Appl. Phys. Lett. **60,** 1741 (1992).

[13] C.L. Johnson, Jan K. Bording, and Yimei Zhu, Phys. Rev. B **78,** 014517 (2008).

[14] R. Beyers, B. T. Ahn, G. Gorman, V. Y. Lee, S. S. P. Parkin, M. L. Ramirez, K. P. Roche, J. E. Vazquez, T. M. GÜr, and R. A. Huggins, Nature **340,** 619 (1990).

[15] R. J. Cava, A. W. Hewat, E. A. Hewat, B. Batlogg, M. Marezio, K. M. Rabe, J. J. Krajewski, W. F. Peck Jr., and L. W. Rupp Jr., Physica C **165,** 419 (1990).

[16] A. A. Abrikosov, Rev. Mod. Phys. **76,** 975 (2004).

[17] V.M. Vinokur, M. V. Feigel'man, and V. B. Geshkenbein, Phys. Rev. Lett. **67,** 915 (1991).

[18] C. M. Aegerter, M. S. Welling, and R. J. Wijngaarden, Europhys. Lett. **65,** 753 (2004).

[19] C. M. Aegerter, M. S. Welling, and R. J. Wijngaarden, Europhys. Lett. **74,** 397 (2006).

[20] G. Oya, N. Aoyama, A. Irie, S. Kishida, and H. Tokutaka, Jpn. J. Appl. Phys., Part 2 **31**, L829 (1992).

[21] H. Arie, K. Yasuda, H. Kobayashi, I. Iguchi, Y. Tanaka, and S. Kashiwaya, Phys. Rev. B **62**, 11864 (2000).

[22] A. S. Katz, A. G. Sun, S. I. Woods, and R. C. Dynes, Appl. Phys. Lett. **72**, 2032 (1998).

[23] J. J. Toppari, T. Kühn, A. P. Halvari, J. Kinnunen, M. Leskinen, and G. S. Paraoanu, Phys. Rev. B **76**, 172505 (2007).

[24] A. Odagawa, M. Sakai, H. Adachi, and K. Setsune, Jpn. J. App. Phys. **37**, 486 (1998).

[25] S. -J. Kim, Yu. I. Latyshev, T. Yamashita, and S. Kishida, Physica C **362**, 150 (2001).

Chapter 2

Theory

In this chapter, we discuss theoretical models and mechanisms that control the temperature dependence of the critical current, its dissipation rate, and the associated vortex dynamics. We also discuss Maley's scheme which we used to extract information about the vortex structure from the time dependence of the current density. Finally, we explain the phenomenon of Cooper pairs tunnelling in superconducting tunnel junctions.

2.1 Temperature dependence of the critical current

2.1.1 Ambegaokar-Baratoff temperature dependence

In 1962, Josephson [1, 2] predicted that a supercurrent of the form $I_s = I_c \sin(\Delta\varphi)$ should flow between two superconducting electrodes at zero voltage separated by a thin insulating barrier. Here I_c is the critical (maximum) current the junction can support, and $\Delta\varphi$ is the difference in the phase of the Ginzburg-Landau wavefunction ($\psi = |\psi| e^{i\varphi}$) in the two superconducting electrodes. Due to the short coherence

length of high-temperature superconductors, the grain boundaries of these materials can serve as weak links [4], and thus intrinsically exhibit the Josephson effect.

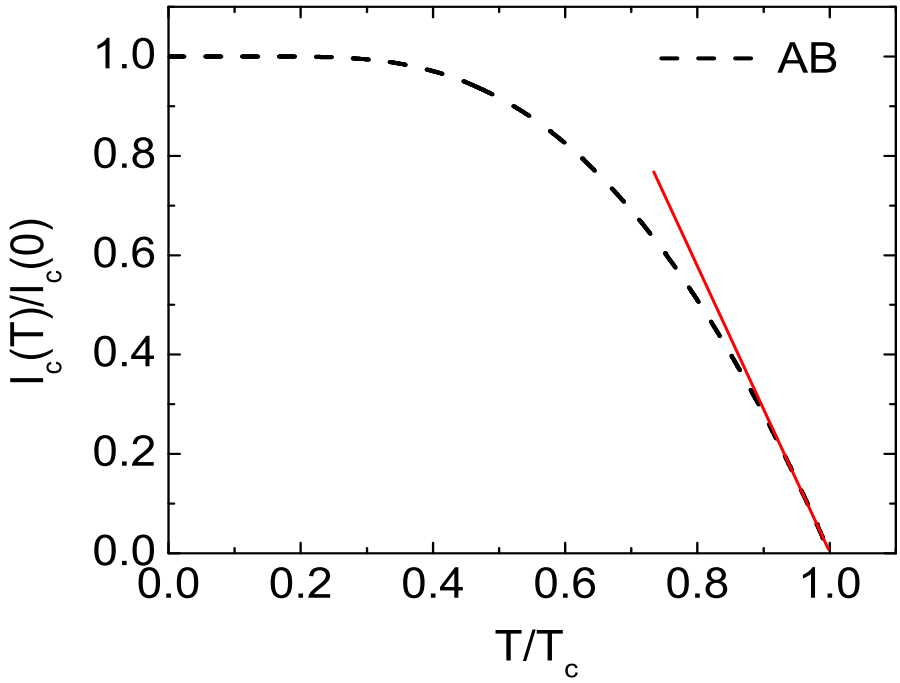

Figure 2.1: Normalized Josephson current $I_c(T)/I_c(0)$ as a function of the reduced temperature T/T_c as derived by Ambegaokar and Baratoff. The dependence is linear ($I_c \propto (1 - T/T_c)$) close to T_c (see red solid line).

Josephson's prediction was latter generalized by Ambegaokar and Baratoff [3] who derived an exact form for the temperature dependence of the critical current across superconductor-insulator-superconductor (SIS) junctions. According to their calculations, $I_c(T)$, shown in Fig.2.1, is given by

$$I_c(T) = \left(\frac{\pi\Delta(T)}{2eR_n}\right) \tanh\left(\frac{\Delta(T)}{2k_BT}\right) \tag{2.1}$$

assuming that the two superconducting electrodes are equivalent (i.e. they have the same Δ). Here, Δ is the BCS superconducting energy gap, R_n is the normal state resistance of the junction, e is the electronic charge, and k_B is the Boltzmann constant.

2.1.2 Clem's model (GL-like temperature dependence)

Kampwirth and Gray [5] have modeled conventional granular superconductor as an array of Josephson-coupled superconducting grains. Later on, Clem *et al.* [6] incorporated the Josephson-coupling model [5] into the Ginzburg-Landau theory [4, 7] of granular superconductors and calculated the temperature dependence of the critical current density ($J_c(T)$), where $J_c = I_c/A$ and A is the cross-sectional area of the of the sample. The advantage of this approach is that it accounts for the ability of the supercurrent to suppress the superconducting gap parameter, which was not taken into account in the Ambegaokar-Baratoff model [3].

In Clem's model, a new dimensionless parameter $\varepsilon = \frac{E_J}{2E_s}$ is introduced, where $E_J = I_0 \left(\hbar/2e\right)$ is the Josephson-coupling energy of the junction between two grains, $E_s = \left(\frac{H_c^2}{8\pi}\right) V$ is the superconducting condensation energy of a grain, $I_0(T) = \frac{\pi\Delta^2(T)}{4eR_n k_B T_c}$ is the Ambegaokar-Baratoff current close to T_c, and V is the average volume of a grain. In the weak coupling limit ($\varepsilon \ll 1$), the condensation energy E_s of a grain is much larger than the Josephson-coupling energy E_J. Therefore, the critical current I_c is not strong enough [6] to induce significant suppression of the superconducting gap parameter and it can be represented by the AB dependence as in Eq. (2.1). However, in the strong coupling limit, the condensation energy E_s of a grain is much smaller

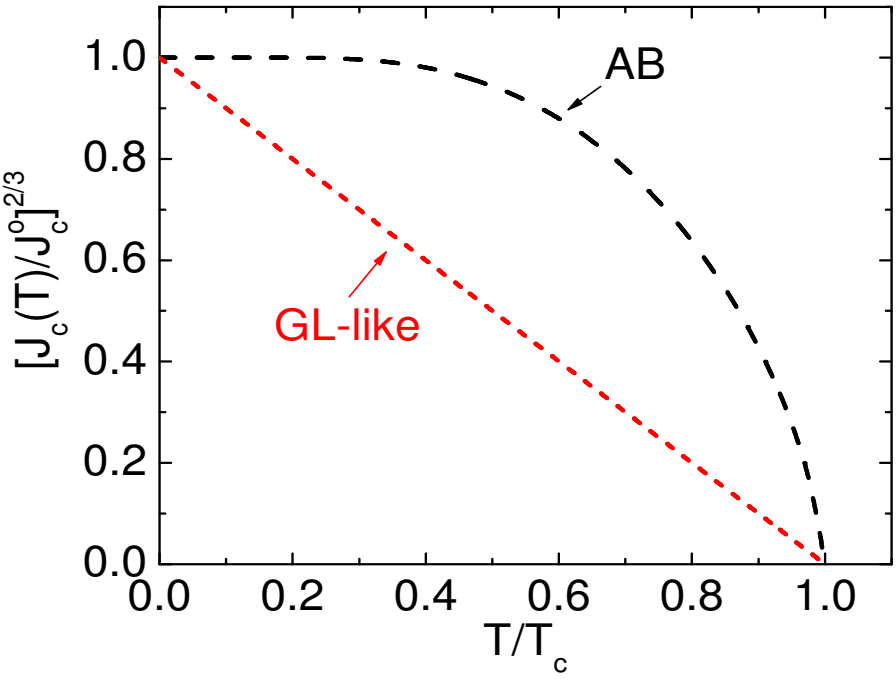

Figure 2.2: Normalized temperature dependence of the normalized critical current densities for both the AB (Eq. (2.1)) and the GL-like (Eq. (2.2)) models raised to the power 2/3. (J_c^o is the normalization factor of the critical current densities at $T = 0$).

than the Josephson-coupling energy E_J, and the parameter $\varepsilon \gg 1$. This results in a significant current-induced gap suppression [6], and the temperature dependence of the normalized critical current density reduces to

$$\frac{J_c(T)}{J_c^o} = \left(1 - \frac{T}{T_c}\right)^{3/2} \tag{2.2}$$

which is the Ginzburg-Landau current density in the dirty limit close to T_c, and J_c^o is the normalization factor of the GL critical current density at $T = 0$. In Figure 2.2, we show the normalized critical current densities of both the AB (Eq. (2.1)) and the

GL-like (Eq. (2.2)) models raised to the power 2/3 as a function of T/T_c. One can see that the GL-like temperature dependence is linear unlike the AB-dependence.

2.2 Vortex motion and the dissipation of the persistent current

In this section, we describe the internal structure of vortices in superconductors. Then, we explain the types of interactions and forces that act on the vortices and the resulting dissipative motion. We finally discuss relevant theoretical models used in explaining the magnetic relaxations in HTSC.

2.2.1 Vortices in the mixed state of type-II superconductors

In the mixed state of type-II HTSC superconductors, magnetic flux lines penetrate the bulk of the superconductor in the form of magnetic vortices. Each vortex carries a quantum of flux

$$\Phi_0 = \frac{hc}{2e} = 2.07 \times 10^{-7} Gauss.cm^2 \tag{2.3}$$

and is surrounded by a supercurrent (j) that concentrates the flux toward the center (core) of the vortex (see Fig. 2.3) [4]. The core of a vortex is non-superconducting (normal) and has a radius in the order of the Ginzburg-Landau coherence length ξ, which is the distance over which the number density of the superelectrons (n_s) decreases to its value of zero at the center of the vortex core. The magnetic flux

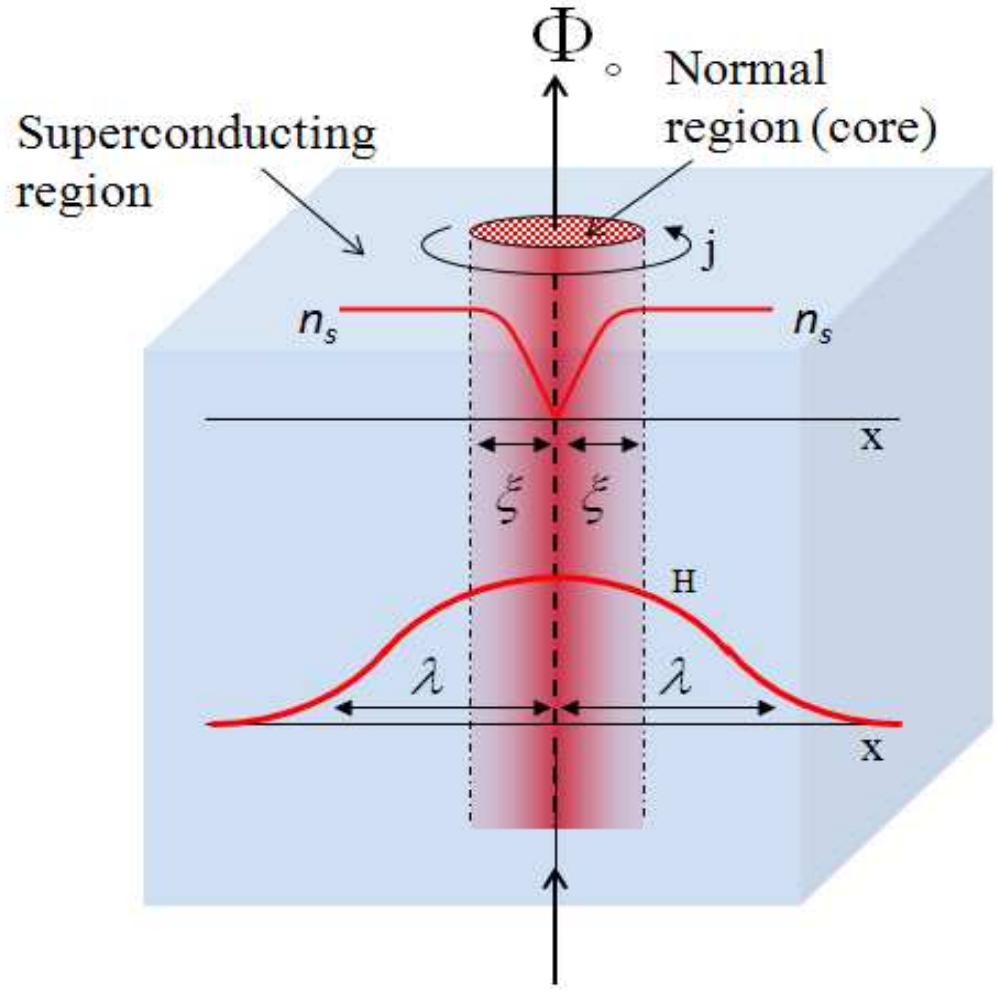

Figure 2.3: Detailed schematic of a vortex. The top curve depicts the variation of the number density of the superconducting electrons n_s, which decreases substantially to zero in a distance ξ. The bottom curve represents the penetration of the magnetic field into the superconducting region over a distance λ.

at the vortex core penetrates a distance λ (penetration depth) into the surrounding superconducting region. The two parameters, ξ and λ, are characteristics of the superconducting material and diverge close to the transition temperature T_c as follows

$$\xi \propto \frac{1}{\left(1-\frac{T}{T_c}\right)^{1/2}} \tag{2.4}$$

$$\lambda \propto \frac{1}{\left(1-\left(\frac{T}{T_c}\right)^4\right)^{1/2}} \tag{2.5}$$

2.2.2 Vortex-vortex and vortex-current interactions

The fact that each vortex has its own supercurrent (j) circulating around it and that it carries non-zero magnetic flux has significant macroscopically detectable consequences. In Fig. 2.4(a) we show two magnetic vortices in close proximity. There is a force resulting from the interaction between the magnetic flux line Φ_0 of one vortex and the supercurrent density j_1 of the other vortex. This Lorentz force is repulsive according to the relation

$$\vec{f}_{12} = \vec{j}_1(\vec{x}_2) \times \frac{\vec{\Phi}_0}{c} \tag{2.6}$$

where Φ_0 is the magnetic flux quantum defined in Eq.(2.3). Additionally, there is another Lorentz force (repulsive) acting on the vortices, which arises from the interaction between any transport current and the magnetic vortices. In Fig. 2.4(b) we consider a superconducting slab with the magnetic vortices in the page and their flux

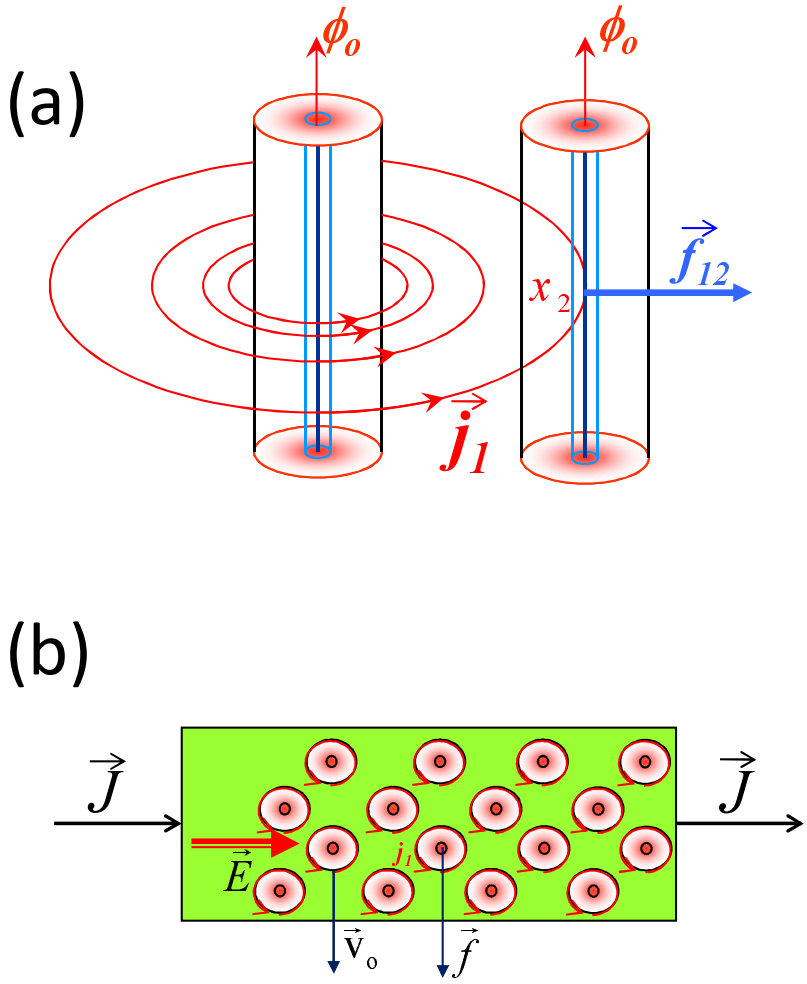

Figure 2.4: Different types of interactions in a superconductor carrying a transport current and magnetic vortices. (a) Vortex-vortex interaction results in a repulsive force f_{12}. (b) Vortex-current interaction exerts driving force f on the vortices. The resulting motion of the vortices with velocity v_o induces an electric field E and dissipates the supercurrent J according to Eq. (2.8) (see text).

lines are pointing out of the page. The transport current density (J) is flowing from the left to the right of the superconducting slab. According to the Lorentz relation $\vec{f} = \vec{J}(\vec{x}) \times \frac{\vec{\Phi}_0}{c}$, there will be a driving force directed downwards, as indicated in Fig. 2.4(b). If the resultant of the forces f_{12} and f is strong enough to overcome the pinning forces, then the vortices start to move with a certain velocity $\vec{v}_0$, and their motion generates an electric field $\vec{E}$

$$\vec{E} = \vec{\Phi}_0 \times \frac{\vec{v}_0}{c} \tag{2.7}$$

in a direction parallel to that of the transport current density $\vec{J}$ (see Fig. 2.4(b)). This causes Ohmic losses given by

$$\vec{J} \cdot \vec{E} = J v_0 \frac{\Phi_0}{c} \tag{2.8}$$

in the superconductor, and leads to the dissipation of the supercurrent.

2.2.3 Magnetic relaxation

As we discussed in the previous section, the stimulated motion of the vortices generates losses in the supercurrent. This motion can, however, be hindered by the presence of strong pinning sites which create potential barriers U opposing the flux motion. There exist many experimental and theoretical works that study the problem of flux pinning and dynamics [4, 8, 9, 10, 11, 12, 13, 14, 15, 16, 17, 18, 19]. Here, we will discuss the interplay between the current densities and the energy barriers in the

context of relevant theories.

The simplest form of the energy barrier $U(J) = U_0(1 - J/J_c)$ against the motion of the vortices in the presence of a current density J was proposed in the Anderson-Kim model [11], with no rigorous justifications. (J_c is the critical current density.) Within this theory, a normalized relaxation rate S was defined as $S = -\frac{d\ln(J)}{d\ln(t)}$. Later on, it was realized that the dependence of U on J is far from being linear [4], and the following more general form of U was suggested

$$U(J) = U_0 \left(1 - \frac{J}{J_c}\right)^{\alpha} \tag{2.9}$$

where, U_0 is the energy barrier in the absence of any current and α is a positive number. Both of the above forms are good approximations for conventional type-II superconductors only, and they simply assume that U is a constant U_0 for J well below J_c [4]. However, this assumption is not valid for the case of HTSC (unconventional type-II superconductors), thus further theoretical considerations were needed. In the limit $J \ll J_c$, the weak collective pinning theory [8, 13, 20, 21] leads to an effective energy barrier of the form

$$U(J) \propto U_c \left(\frac{J_c}{J}\right)^{\mu} \tag{2.10}$$

where U_c is the characteristic pinning energy and μ is a positive number [8].

A significant amount of information about the vortex structure can be extracted from the value of the critical exponent μ appearing in Eq. (2.10). However, the calculation of μ requires knowledge of U, which cannot be measured directly, but

rather can be obtained from the time dependence of the magnetic relaxation data, according to Maley's scheme [14]. Nideröst *et al.* [16] have extended Maley's scheme to the case of remnant magnetization relaxations, which is similar to the case of current density J in zero external magnetic field. Nideröst *et al.* [16] found the following master equation

$$U(J,T) \simeq -k_B T\{\ln|(dJ/dt)/J_o| - C\} \tag{2.11}$$

correlating U, J, and the temperature T, where k_B is the Boltzmann constant, and J_o is the current density close the critical value. The constant C is related to the hopping distance and to the attempt frequency of a vortex, and can be adjusted in order to ensure that $U(J,T)$ is a continuous function of J at low temperatures [14]. The temperature dependence of $U(J,T)$ can be separated by dividing it by the so-called thermal factor $g(T)$ suggested by Thompson *et al.* [15]. In this way, the energy barrier U can be calculated and thus the value of the critical exponent μ can be extracted. This approach will be used in the analysis of the persistent current relaxation data presented in Chapter 5.

2.3 Superconducting tunnel junctions

Superconducting tunnel junctions (STJs) represent an important type of Josephson junctions and are made up of two superconducting electrodes separated by a thin insulating layer. If the insulating layer is thin enough, then the wavefunctions of the

superelectrons (Cooper pairs) of the two superconducting electrodes can overlap in the junction area. Hence, upon applying a bias voltage (V) across the junction, there is a non-zero probability for having Cooper pairs tunnelling from the first superconducting electrode (S_1) to the second superconducting electrode (S_2). This results in the so-called tunnelling current. In Fig. 2.5 we show a schematic of the energy levels of two identical superconducting electrodes [9], hence having the same energy gap 2Δ, in the two cases where $V = 0$ and V is larger than the gap voltage (V_g). One can see that, at $V = 0$ (Fig. 2.5(a)), the system is at equilibrium with the electronic energy diagrams of S_1 and S_2 being the same. If a voltage $V > V_g$ is applied across the junction, the equilibrium is lifted and the tunnelling of the Cooper pairs is triggered. This process is shown in three steps in Figs. 2.5(b-d). First, a Cooper pair in S_1 breaks up and one of the electrons of the pair tunnels to the excited states of S_2 (see process 1 in Fig. 2.5(b)), thereby releasing an energy greater than or equal to V_g. This released energy is large enough to excite the second electron of the broken pair so that it becomes a quasiparticle in an excited state of its own superconductor S_1 (see process 2 in Fig. 2.5(b)). The result of these two processes is shown in Fig. 2.5(c). The first electron of the broken Cooper pair that tunneled to S_2, then pairs up with another electron (quasiparticle) in the excited state of S_2, and relaxes back to the ground state of S_2 to become a Cooper pair (see process 3 in Fig. 2.5(d)). The $I - V$ characteristic curve for two identical superconductors is shown in Fig. 2.6, where it is evident that the tunnelling current increases as the bias voltage is increased beyond the gap voltage, and that the curve is antisymmetric (odd), i.e. when $V \longrightarrow -V$

we will have $I \longrightarrow -I$. At voltages much higher than the gap voltage, the junction approaches its normal metal behavior (see dashed straight line in Fig. 2.6). This basic idea clarifies the understanding of the tunnelling phenomenon presented in Chapters 6 and 7.

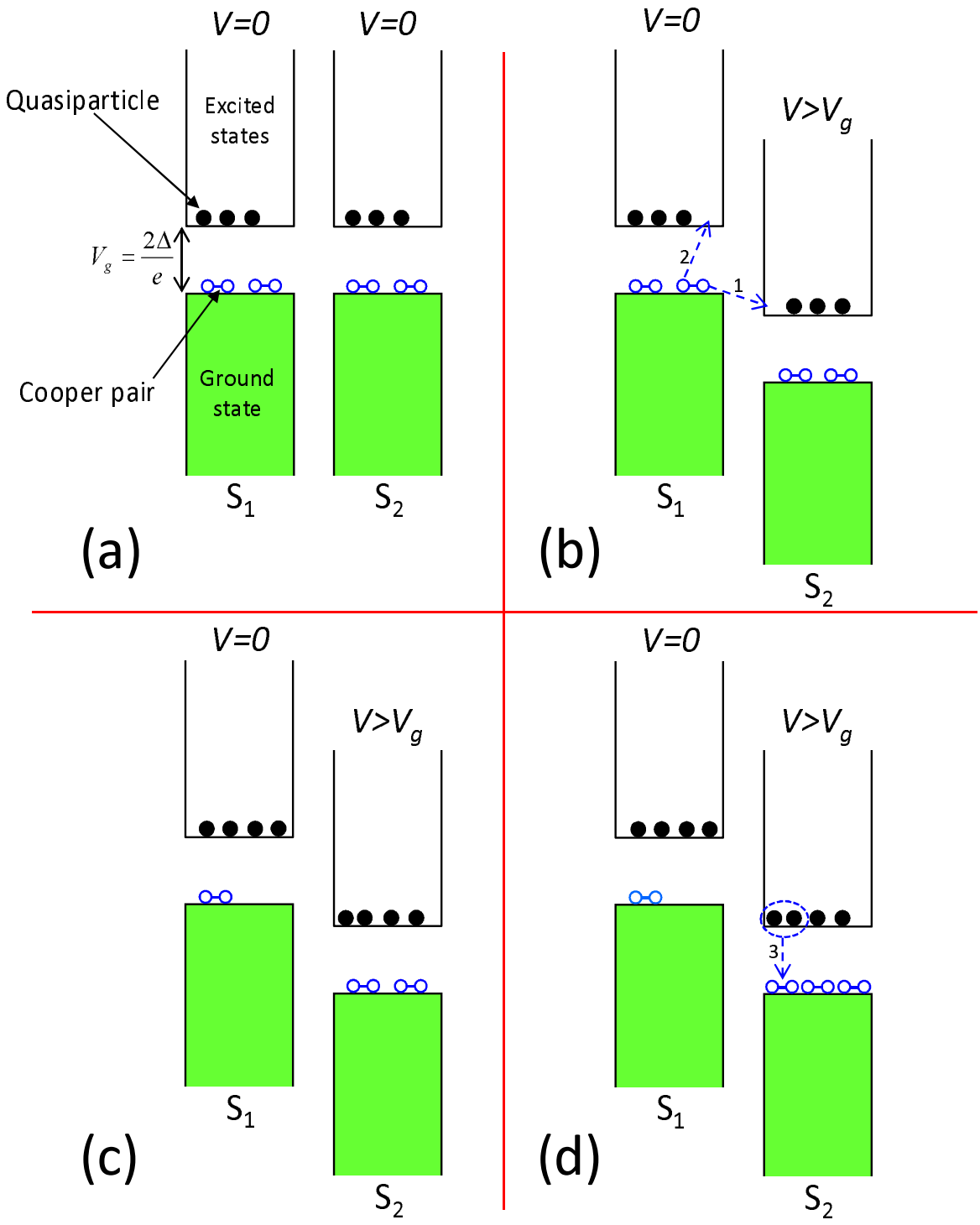

Figure 2.5: Tunnelling between two identical superconductors (S_1 and S_2) at $T \neq 0$.

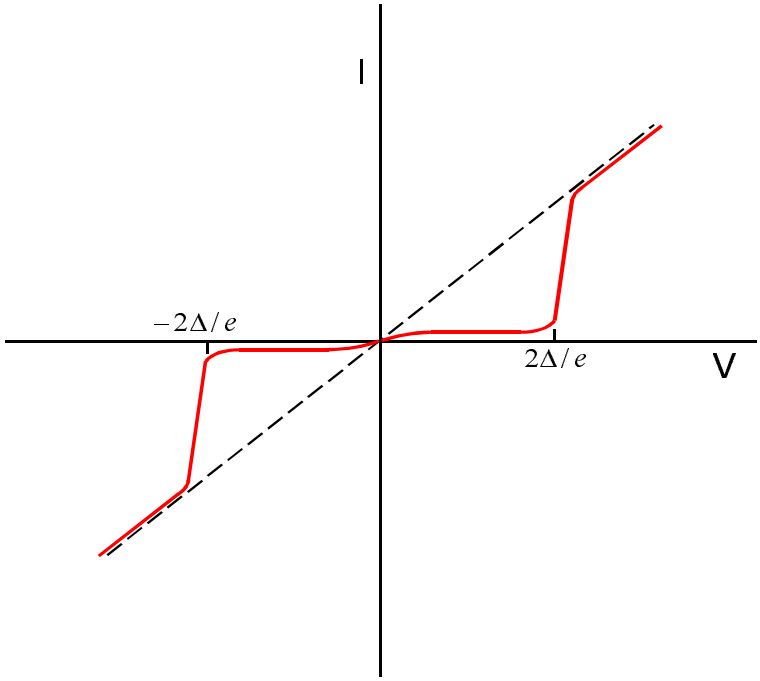

Figure 2.6: Tunnelling current (I) as a function of bias voltage (V) between two identical superconductors (S_1 and S_2) at $T \neq 0$.

Bibliography

[1] B. D. Josephson, Phys. Lett. **1,** 251 (1962).

[2] B. D. Josephson, Adv. Phys. **14,** 419 (1965).

[3] Vinay Ambegaokar and Alexis Baratoff, Phys. Rev. Lett. **10,** 486 (1963); Phys. Rev. Lett. **11,** 104 (1963).

[4] M. Tinkham, *Introduction to Superconductivity* (McGraw-Hill, New York, 1996) 2nd edition.

[5] R. T. Kampwirth and K. E. Gray, IEEE Trans. Magn. MAG- **17,** 565 (1981).

[6] J. R. Clem, B. Bumble, S. I. Raider, W. J. Gallagher, and Y. C. Shih, Phys. Rev. B **35,** 6637 (1987).

[7] G. Deutscher, Y. Imry and L. Gunther, Phys. Rev. B **10,** 4598 (1974).

[8] G. Blatter, M. V. Feigel'man, V. B. Geshkenbein, A. I. Larkin, and V. M. Vinokur, Rev. Mod. Phys. **66,** 1125 (1994).

[9] Charles P. Poole, H. A. Farach, and R. J. Crewswick, *Superconductivity* (Academic Press, San Diego, 1995) 1st edition.

[10] P. W. Anderson, Phys. Rev. Lett. **9,** 309 (1962).

[11] P. W. Anderson and Y. B. Kim, Rev. Mod. Phys. **36,** 39 (1964).

[12] M. R. Beasley, R. Labusch, and W. W. Webb, Phys. Rev. **181,** 682 (1969).

[13] A. I. Larkin and Yu. N. Ovchinnikov, J. Low Temp. Phys. **34,** 409 (1979).

[14] M. P. Maley, J. O. Willis, H. Lessure, and M. E. McHenry, Phys. Rev. B **42,** 2639 (1990).

[15] J. R. Thompson, L. Krusin-Elbaum, L. Civale, G. Blatter, and C. Feild, Phys. Rev. Lett. **78,** 3181 (1997).

[16] M. Nideröst, A. Suter, P. Visani, and A. C. Mota, G. Blatter, Phys. Rev. B **53,** 9286 (1996).

[17] T. Aytug, M. Paranthaman, K. J. Leonard, S. Kang, P. M. Martin, L. Heatherly, A. Goyal, A. O. Ijaduola, J. R. Thompson, D. K Christen, R. Meng, I. Rusakova, and C. W. Chu, Phys. Rev. B **74,** 184505 (2006).

[18] S. Doniach, Seungoh Ryu, and A. Kapitulnik, J. Low Temp. Phys. **95,** 353 (1994).

[19] A. Goyal, S. Kang, K. J. Leonard, P. M. Martin, A. A. Gapud, M. Varela, M. Paranthaman, A. O. Ijaduola, E. D. Specht, J. R. Thompson, D. K. Christen, S. J. Pennycook, and F. A. List, Supercond. Sci. Technol. **18,** 1533 (2005).

[20] V. M. Vinokur, M. V. Feigelman, V. B. Geshkenbein, and A. I. Larkin, Phys. Rev. Lett. **65,** 259 (1990).

[21] D. R. Nelson and M. Vinokur, Phys. Rev. B **48,** 13060 (1993).

[22] V. L. Ginzburg and L. D. Landau, Zh. Eksperim. i. Teor. Fiz. **20**, 1064 (1950).

Chapter 3

Experimental Aspects

3.1 Introduction

The critical current density (J_c) is one of the main superconducting properties of high temperature superconductors (HTSCs) that determine the usefulness of these materials for applications. Hence, it is very important to be able to measure this quantity with high accuracy. There exist several standard techniques for measuring the critical current I_c, from which one can calculate J_c by knowing the dimensions of the sample. These standard measurement techniques include: dc transport, pulse transport, and dc magnetization.

In the dc transport technique, an I-V curve is obtained by measuring the voltage across the superconductor while applying a direct current. The critical current I_c is defined as the value of the applied current that gives rise to a non-zero voltage across the superconductor, where the non-zero voltage criterion is determined by the sensitivity of the instrument (voltmeter) being used. This sensitivity imposes limitations on the accuracy of measuring I_c and usually overestimates it. In the pulse transport technique, short duration current pulses are applied to the superconductor across

which the voltage is measured using an oscilloscope. The non-zero voltage criterion is also involved in this techniques leading to similar limitations on the accuracy of the measured I_c. Moreover, both of these techniques require direct contact with the superconducting sample, resulting in a considerably high resistance at the interface between the sample and the contacts. The heating power at this interface is very large and can easily reach several hundreds of Watts [1]. This can locally increase the sample's temperature, thus leading to an underestimation of the actual critical current.

In the dc magnetization measurement technique, the critical current density J_c is indirectly estimated from the measured width ΔM of the magnetization hysteresis using Bean's model [2, 3]. According to this model, a surface critical current density $J_c = 2\Delta M/D$ (in SI units) is induced in a superconducting grain of size D upon the application of a particular external magnetic field at which there is full magnetic flux penetration into the superconducting grain. There are two disadvantages for this technique. Not only does it estimate J_c indirectly, but it also assumes that all the grains of the sample are aligned together, with an average grain size D.

In all the experimental work presented in this thesis, we used an unconventional technique that avoids all the problems common to the above mentioned standard techniques. Our technique is direct, in the sense that what we measure is a magnetic field due to a persistent current circulating in a superconducting ring in zero external magnetic field. It is also contactless, and hence avoids the heating effects and the non-zero voltage criterion. Note that our experimental setup based on this technique

is capable of acquiring persistent current relaxation data in a time as short as 0.6 sec per data point. Therefore, our measured critical current values are within 0.6 sec of the actual I_c.

In the remaining part of this chapter, we discuss the details of our experimental setup, and we show the crystal structure and phase diagram of YBCO, the superconducting material investigated in this thesis. Then, we discuss the sample preparation and characterization methods. Finally, we describe the procedures for measuring the temperature and time dependences of the persistent current.

3.2 Experimental setup

The experimental setup consists of a Cryogenic refrigerator (cold head), vacuum chamber, copper solenoid, scanning Hall probe sensor, and the complementary electronics and software for data acquisition. In Fig. 3.1, we show a schematic of the experimental setup, where the sample is mounted inside a copper sample holder and is placed in good thermal contact with the top part of the cold head. The cold head cools the sample down to 8.5 K from room temperature at a rate of 2°C/min. Temperature sensors are placed close to the sample and are connected to a Keithley temperature controller which reads and controls the temperature of the sample with a resolution of 0.1°C. The vacuum chamber containing this setup can be pumped down to a pressure of 10-20 mTorr using an Alcatel roughing pump. The sample, whether a thin film or bulk, is mounted such that its surface is only 2.5 mm below the active

area of a Hall sensor positioned in air at room temperature. This 2.5 mm distance was needed in order to detect the strongest possible magnetic field of the sample. The active area of the Hall probe sensor is around 0.4 mm^2, has a sensitivity of ± 2 mGauss, and is connected to a LakeShore Model 450 Gaussmeter. Using a controlled stepper motor, we can move the Hall probe across the sample surface and scan a horizontal distance of 21 mm. A Mutotoyo digital micrometer reads the position of the Hall probe with a resolution of 0.01 mm. A software stores the position of the scanning Hall probe and the corresponding magnetic field in a time as short as 0.6 s per data point. A water-cooled copper solenoid is placed around this setup (Fig. 3.1) so that it creates a uniform magnetic field across the sample, and it can generate a maximum field of 1.5 kGauss. There are many advantages of using a copper solenoid as a source of magnetic field instead of using a superconducting magnet. One advantage is that the process of applying/changing/removing the magnetic field in a copper solenoid is almost instantaneous (response time < 0.6 s) compared to the long response time (about minute) of a superconducting magnet. Another advantage is that the copper solenoid dose not suffer from the trapped magnetic field problem as a superconducting magnet does.

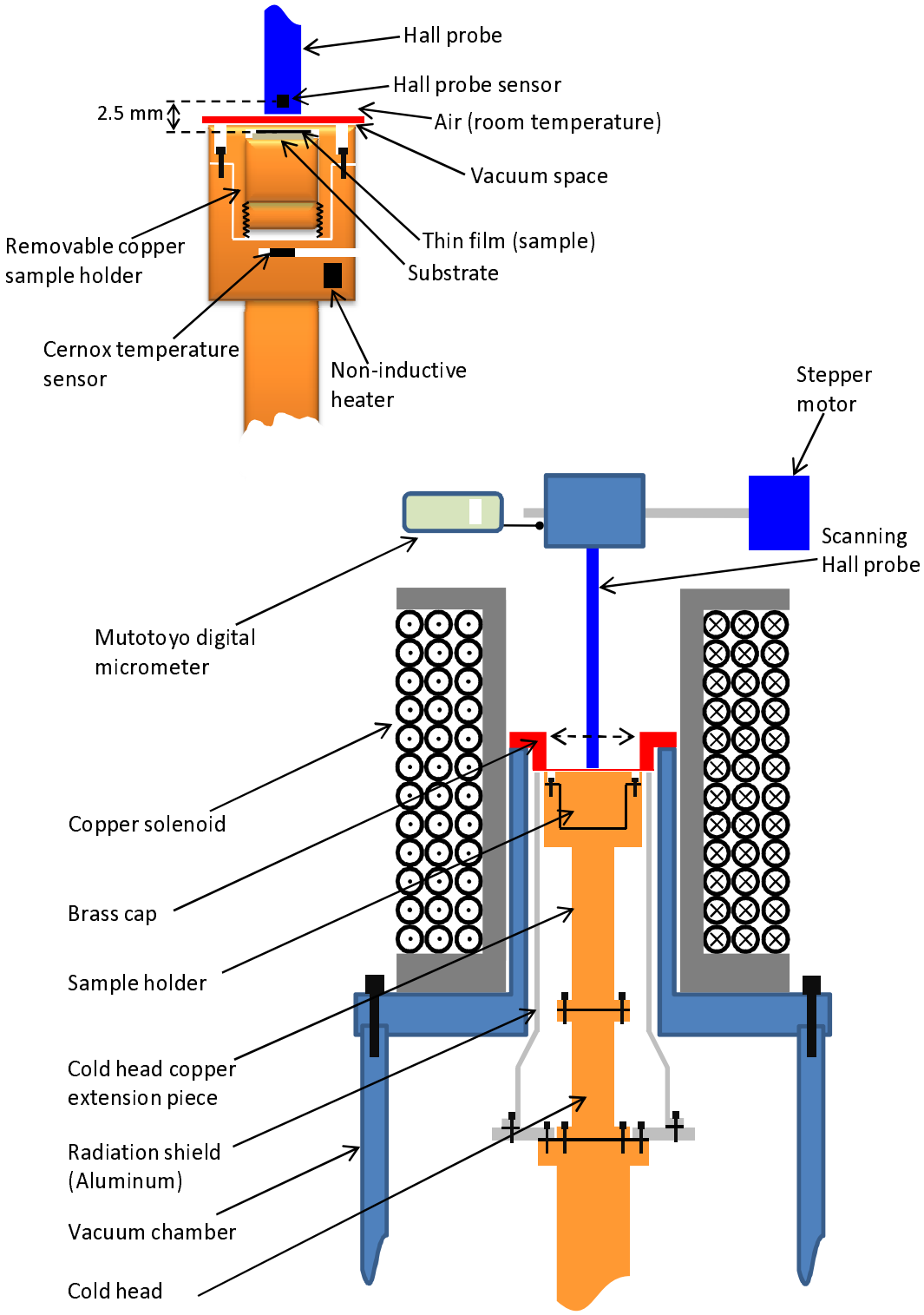

Figure 3.1: Schematic of the measurement system. Top left: details of the sample holder, the position of the sample and the Hall probe sensor.

3.3 $YBa_2Cu_3O_{7-\delta}$ crystal structure and phase diagram

$YBa_2Cu_3O_{7-\delta}$, also called Y-123 or YBCO, is a high-temperature superconductor with transition temperature $T_c = 92$ K in the optimally doped phase, coherence lengths $\xi_{ab} = 1.2$ nm and $\xi_c = 0.3$ nm, and penetration depths $\lambda_{ab} = 89$ nm and $\lambda_c = 550$ nm [3]. It is superconducting in the orthorhombic form, belongs to the perovskite family, and has a layered crystal structure as sketched in Fig. 3.2. Because of the insulating/semiconducting nature of the Y and Ba oxide planes, the conduction electrons flowing along the c-axis (perpendicular to these oxide planes) experience a resistance higher than what they experience while flowing in the ab-plane (parallel to these oxide planes). This gives YBCO a quasi-two dimensional property and makes it anisotropic. YBCO also belongs to the family of cuprate superconductors, because it contains CuO_2 planes in which the superconducting phenomenon is believed to be confined. In the CuO_2 planes [3], each copper cation (Cu^{2+}, $3d_{x^2-y^2}$) has four oxygen nearest neighbors and each oxygen anion (O^{2-}, $2p_x$ or $2p_y$) has two copper nearest neighbors. The orbital lobes in the CuO_2 planes are depicted in Fig. 3.3 and their signs chosen so as to make all of the overlaps of the bonding type. YBCO has a unique property among the cuprate superconductors, in that it contains CuO chains which dope the CuO_2 with holes, and a large enough hole doping level gives rise to the superconducting state. (Note that, the undoped CuO_2 planes are antiferromagnetic insulators.) In Fig. 3.4, we show the phase diagram [4] of YBCO, where the superconducting phase manifests itself as a dome extending over a restricted

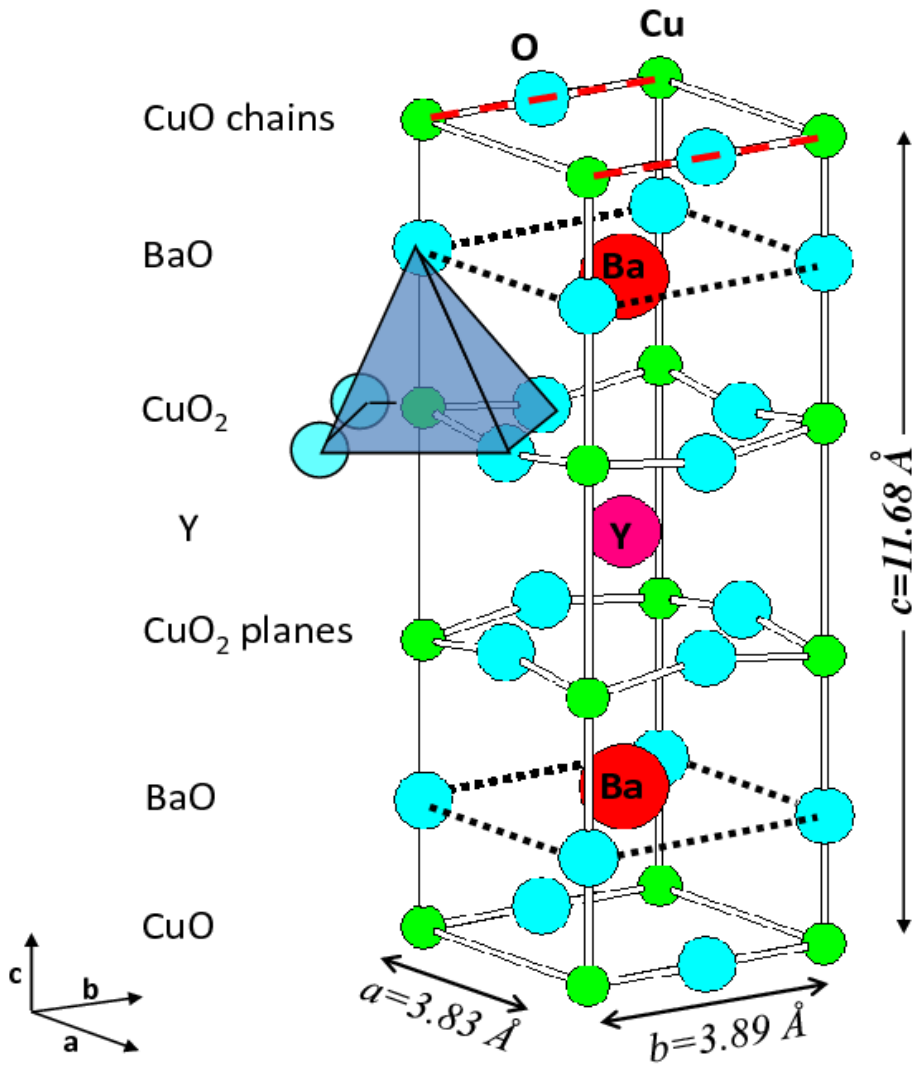

Figure 3.2: Crystal structure of $YBa_2Cu_3O_7$.

range of the hole doping level.

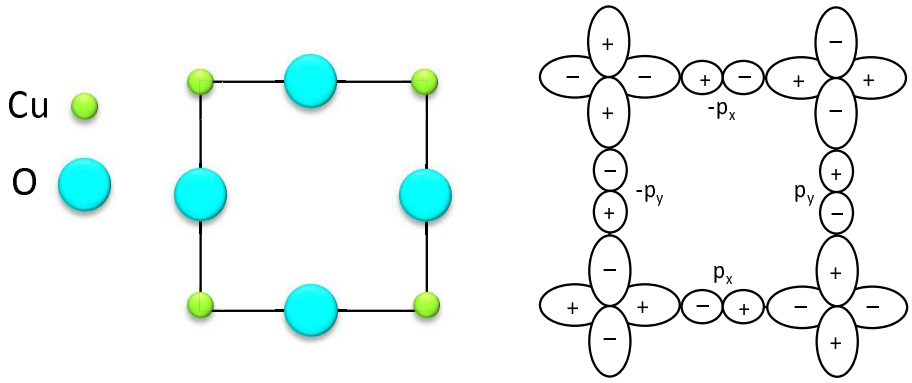

Figure 3.3: Detailed schematic of the CuO_2 square planes structure (left) and overlapping orbitals (right). The d and p orbitals of Cu^{2+} and O^{2-}, respectively, are shown with signs on the orbitals selected so that all of the overlaps are of the bonding type [3].

3.4 Sample preparation and characterization

The overriding concern in the preparation of high temperature superconducting thin films is their quality and the ability to control their superconducting properties. The increasing interest in superconducting thin films, compared to bulk and single crystals, is mainly due to their usefulness in many applications [6, 7, 8, 9], their ability to carry high currents, and to the flexibility of engineering them in different forms like junctions (inherent component of SQUIDS) and multilayers. There exist numerous deposition techniques that can be used to prepare HTSC thin films, and there are also many choices of substrates and buffer layers. The existing deposition techniques include laser ablation of stoichiometric ceramic pellets, rf and dc magnetron sputtering, MetalOrganic Chemical Vapor Deposition (MOCVD), and Molecular Beam Epitaxy (MBE). It is the purpose of the study to be conducted that determines the choice of the deposition method and the substrate type. In fact, the type of studies

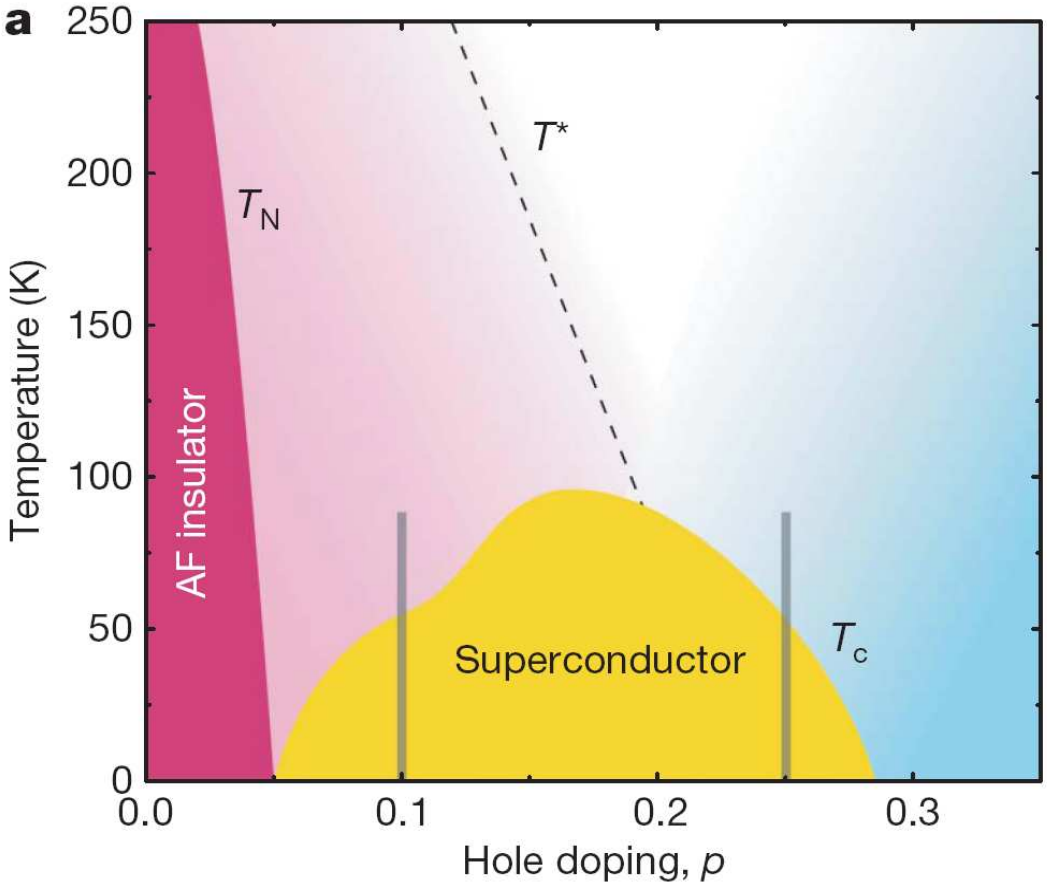

Figure 3.4: $YBa_2Cu_3O_{7-\delta}$ phase diagram showing the antiferromagnetic region and the superconducting dome. This figure as is taken from Leyraud *et al.* Nature **447,** 565 (2007).

that we conduct in this thesis requires films that are uniform over an area as large as 25-100 mm^2, and rf off-axis magnetron sputtering is considered to be the most appropriate technique for producing such uniform thin films [5, 10]. For this reason, we used the rf-magnetron sputtering technique in all the studies reported in this thesis, to deposit YBCO thin films on $\langle 100 \rangle$ oriented $LaAlO_3$ (LAO) or $SrTiO_3$ (STO) single crystal substrates, which were chosen because of their relatively small lattice mismatch ($\sim$+1.5% for LAO and $\sim$-1.5% STO) with YBCO.

The ceramic YBCO targets used in the deposition process were prepared following the standard solid-state reaction method. First, the desired proportions of Y_2O_3, $BaCO_3$, and CuO powders were mixed and pressed into pellet form of 1 inch diameter. The pellet was then calcined in air at 900°C for 24 hours. The resulting material was then crushed, pressed, and calcined two more times under the same conditions. Finally, the YBCO pellet was sintered in air at a temperature of 950°C for 24 hours.

As for the YBCO thin film deposition process, it was carried out in an atmosphere of oxygen-argon mixture (100 mTorr of O_2 and 20 mTorr of Ar), while the substrate temperature was set to 750°C. The deposited film was then cooled down to 500°C at an O_2 gas pressure of $\sim$ 1 atm, and the film was annealed under these conditions for 2 hours. Finally, the film was cooled down to room temperature at a rate of $\sim$8°C/min. X-ray diffraction measurements were first carried out in order to verify that the deposited film is epitaxial, i.e. *c*-axis oriented. In Figure 3.5 we show the diffraction patterns of YBCO thin films deposited on LAO and STO substrates. The observed peaks correspond to the $\langle 100 \rangle$ orientation of the deposited YBCO films,

thus confirming the epitaxial nature of the films. The substrate's peaks can be also observed in the x-ray diffraction patterns. After the x-ray diffraction measurements were complete, the YBCO thin films were patterned into ring-shaped form using a photolithography technique.

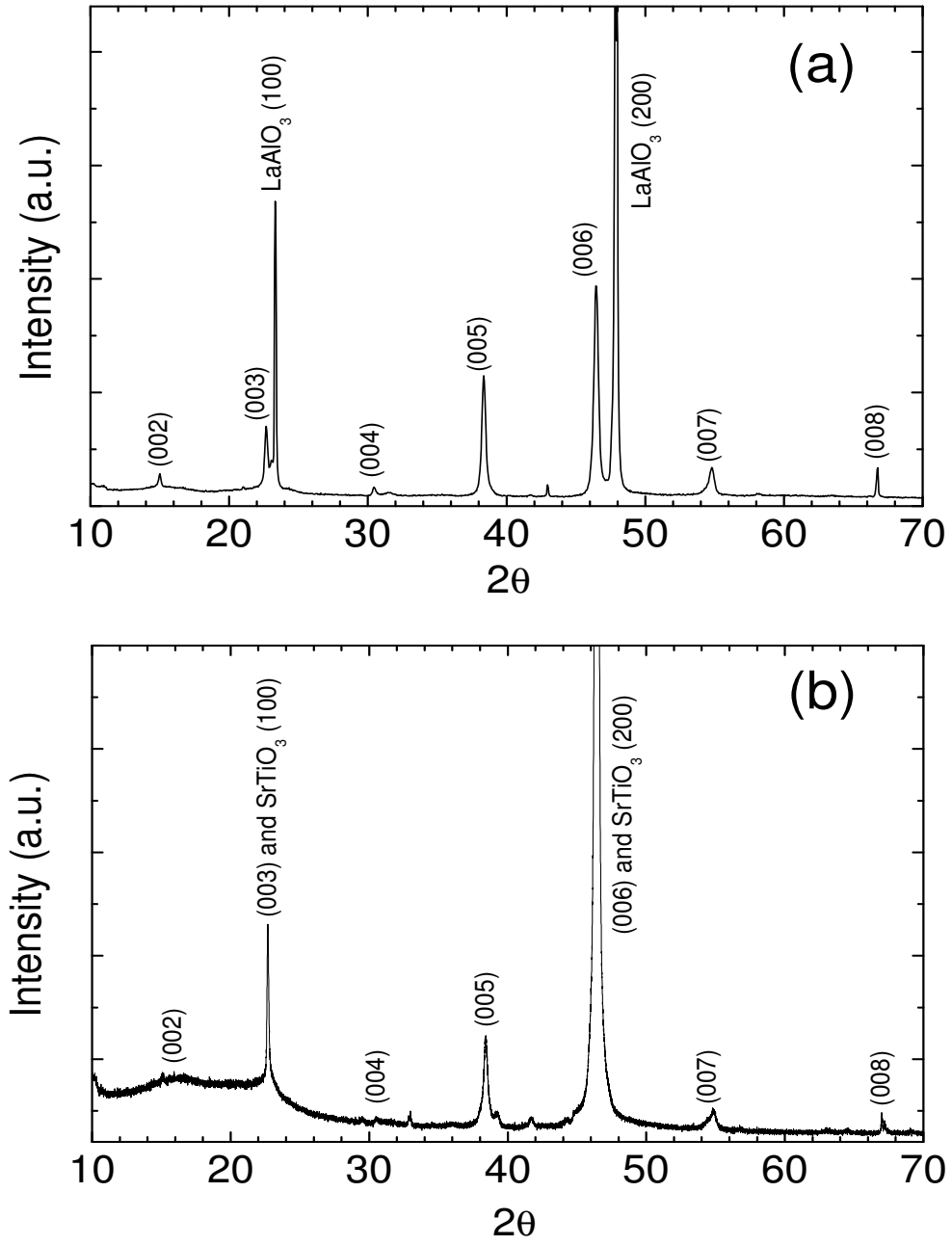

Figure 3.5: Typical x-ray diffraction pattern of $YBa_2Cu_3O_{7-\delta}$ epitaxial thin films deposited on (a) $LaAlO_3$ and (b) $SrTiO_3$ substrates.

3.5 Measurements of the critical persistent current

In this section, we describe in detail the previously mentioned contactless measurement technique, which enables the distinction between the magnetic field due to the circulating persistent current and that due to the trapped vortices in the rings bulk [5]. Using the experimental setup shown in Fig. 3.1, we induced a persistent current in the ring by cooling it in a zero-field to the temperature of interest below T_c. Then we applied an external magnetic field along the ring's axis, and subsequently reduced it to zero. The axial profile of the magnetic self-field $B_z(r)$ (see Fig. 3.6) of the persistent current was then measured across the ring with a traveling Hall sensor [11, 12]. The critical value of the persistent current I_c is reached when $B_z(r)$ becomes independent of the applied magnetic field as shown in Fig. 3.7. The magnitude of I_c at a particular temperature, was obtained from $B_z(r)$ using the Biot-Savart's law. In order to measure I_c at a different temperature, the sample was warmed above its transition temperature so that we get rid of all the trapped flux, and then was zero-field cooled again to another temperature below T_c. This procedure was repeated for temperatures ranging from 10 K up to T_c, in order to obtain the temperature dependence of I_c, and the temperature dependence of the critical current density J_c shown in Fig. 3.8 was calculated using the dimensions of the sample.

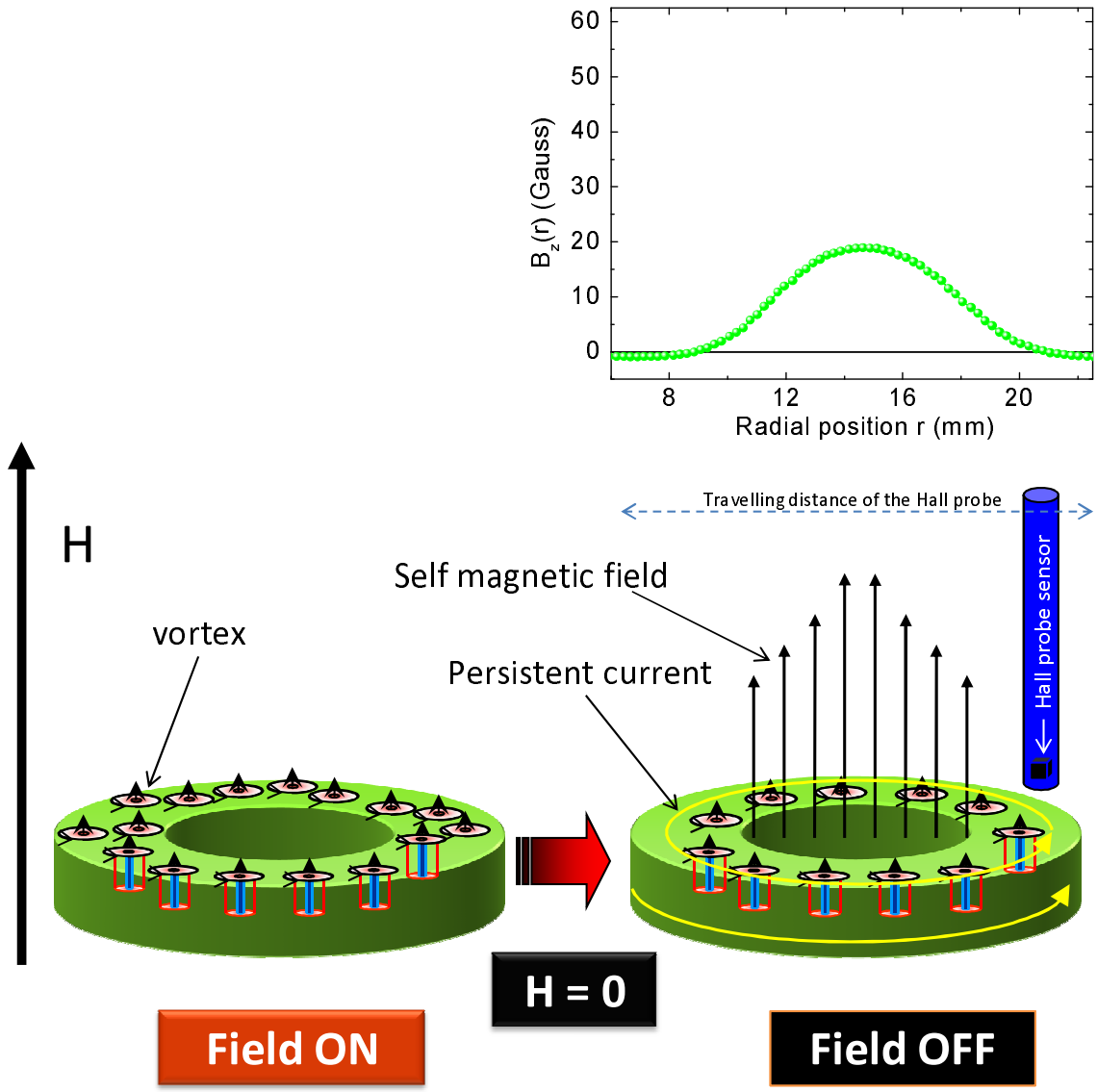

Figure 3.6: Schematic representation of a superconducting ring. The method used for inducing a persistent current in the ring is illustrated. The sample is first zero-field cooled, then an external field (**H**) is applied (such that H > H_{c_1}) and switched off suddenly. The magnetic field B_z due to the induced persistent current is measured using a traveling Hall probe, where a software records the measured magnetic field profile $B_z(r)$ and the corresponding radial position of the probe. Typical $B_z(r)$ profile is also shown. (The shown internal magnetic fields are simplified compared to the real situation.)

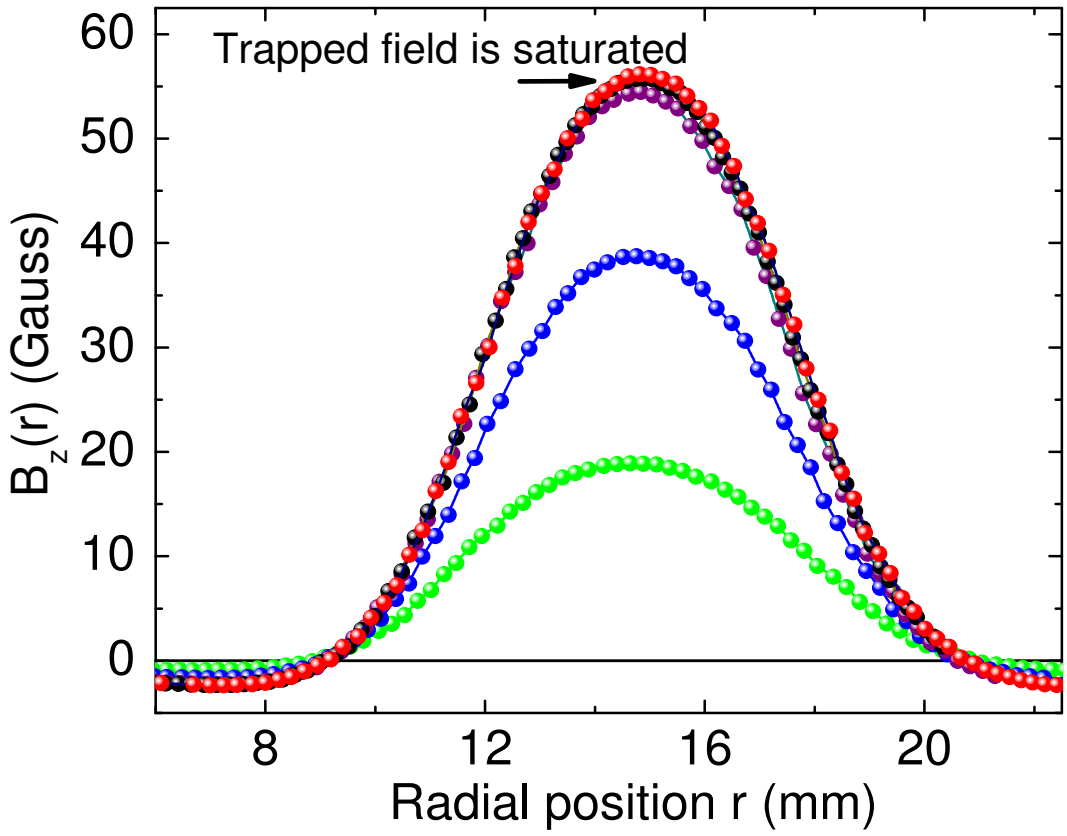

Figure 3.7: Typical scan of the self-field $B_z(r)$ of a persistent current generated in a ring-shaped film as shown in Fig. 3.6. Here, the externally pulsed magnetic field was increased until $B_z(r)$ showed no further increase. This means that the persistent current induced in the superconducting ring is at its critical level.

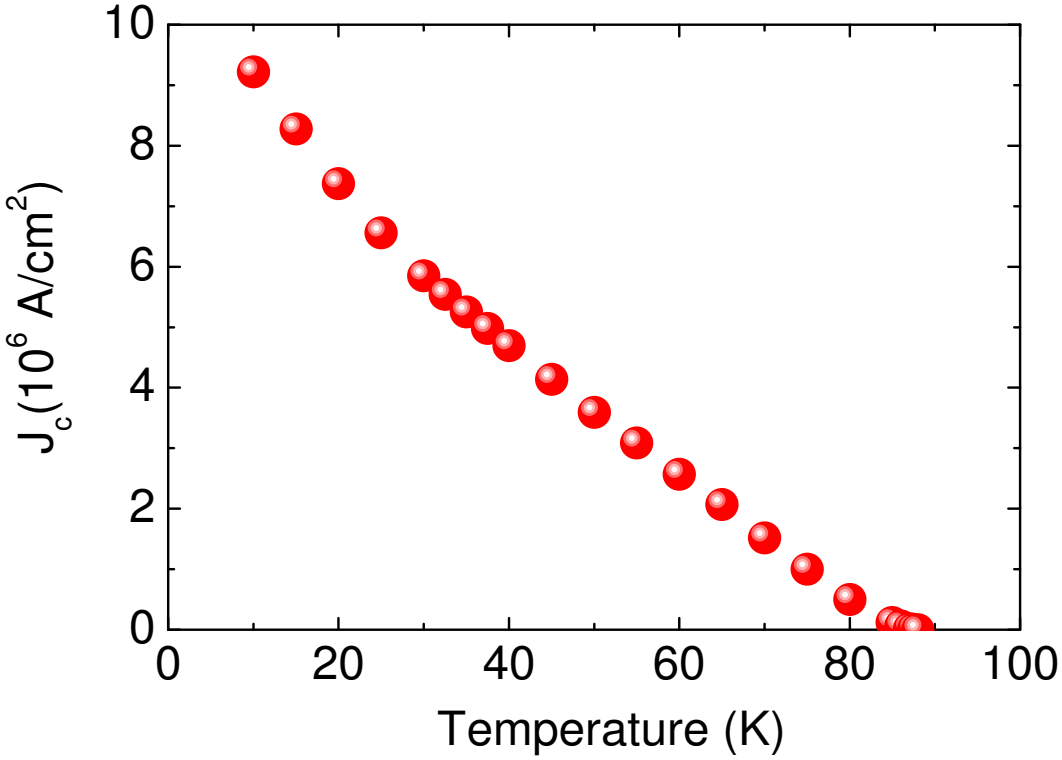

Figure 3.8: Temperature dependence of the persistent critical current density J_c. Each value of the critical current I_c was calculated from the measured maximum value $B_z(r)$ at the center of the ring using Biot-Savart's law. The measurements of the dimensions of the ring (thickness, internal and external diameters) allowed us to convert I_c into critical current density J_c.

3.6 Measurements of the persistent current dissipation

As we explained in Section 2.2, vortex-vortex and vortex-current interactions lead to the dissipative motion of the magnetic vortices. In a ring geometry, the net of these two Lorentz forces is a centrifugal force pushing the vortices radially out of the superconducting ring, as shown in Fig. 3.9.

The measurement of the time dependence of the persistent current density was made possible by the instantaneous turn-off response (<0.6 sec) of the copper solenoid used to generate the external magnetic field, and by the high speed of data points acquisition. First the Hall probe was placed above the center of the ring which can be determined from the maximum value of $B_z(r)$ (see Fig. 3.7). Then, the critical persistent current was induced at a particular temperature as explained in Sec. 3.5, and its relaxation (time dependence) was recorded over a time range of 1-10000 sec at a particular temperature. The relaxation measurements were performed for temperatures ranging from 10 K up to temperatures close to T_c (see Fig. 3.10(a)). The measured time dependence of the persistent current density is logarithmic [5, 11, 12], and its normalized decay rate is given by $S = -\frac{d\ln(J)}{d\ln(t)}$. In Fig. 3.10(b), we show a typical plot for the temperature dependence of the dissipation rate S.

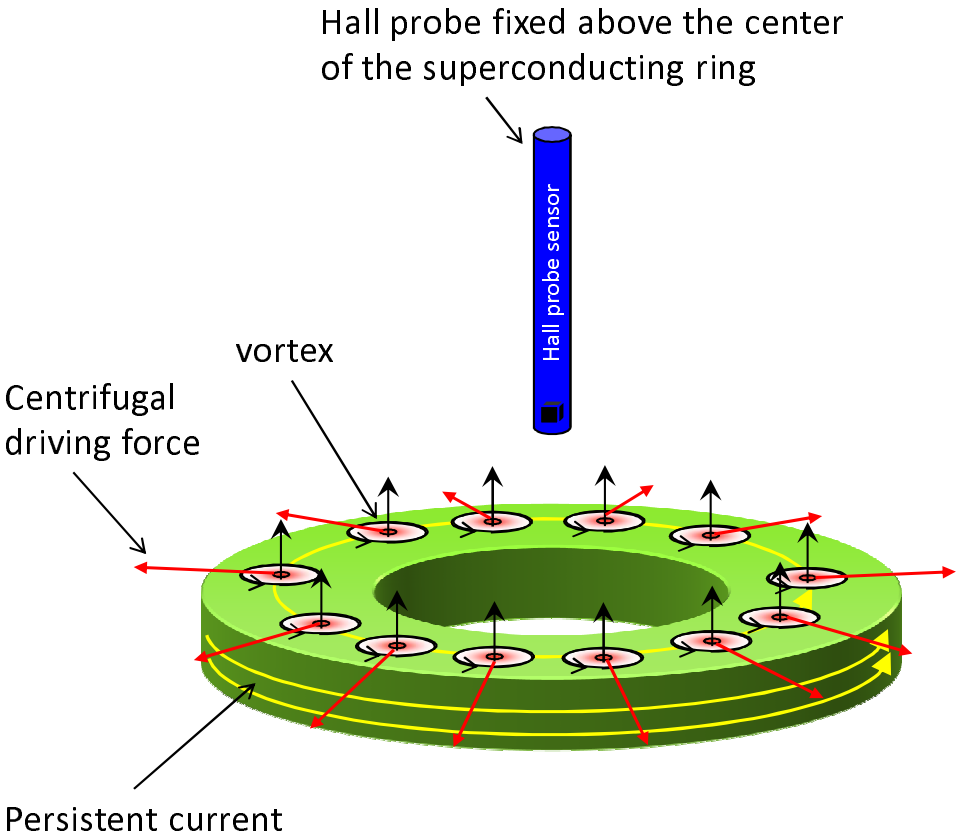

Figure 3.9: Schematic of the superconducting ring with the persistent current induced and the Hall probe fixed above its center. The direction of the driving forces on the vortices are shown as red arrows pointing radially out of the ring.

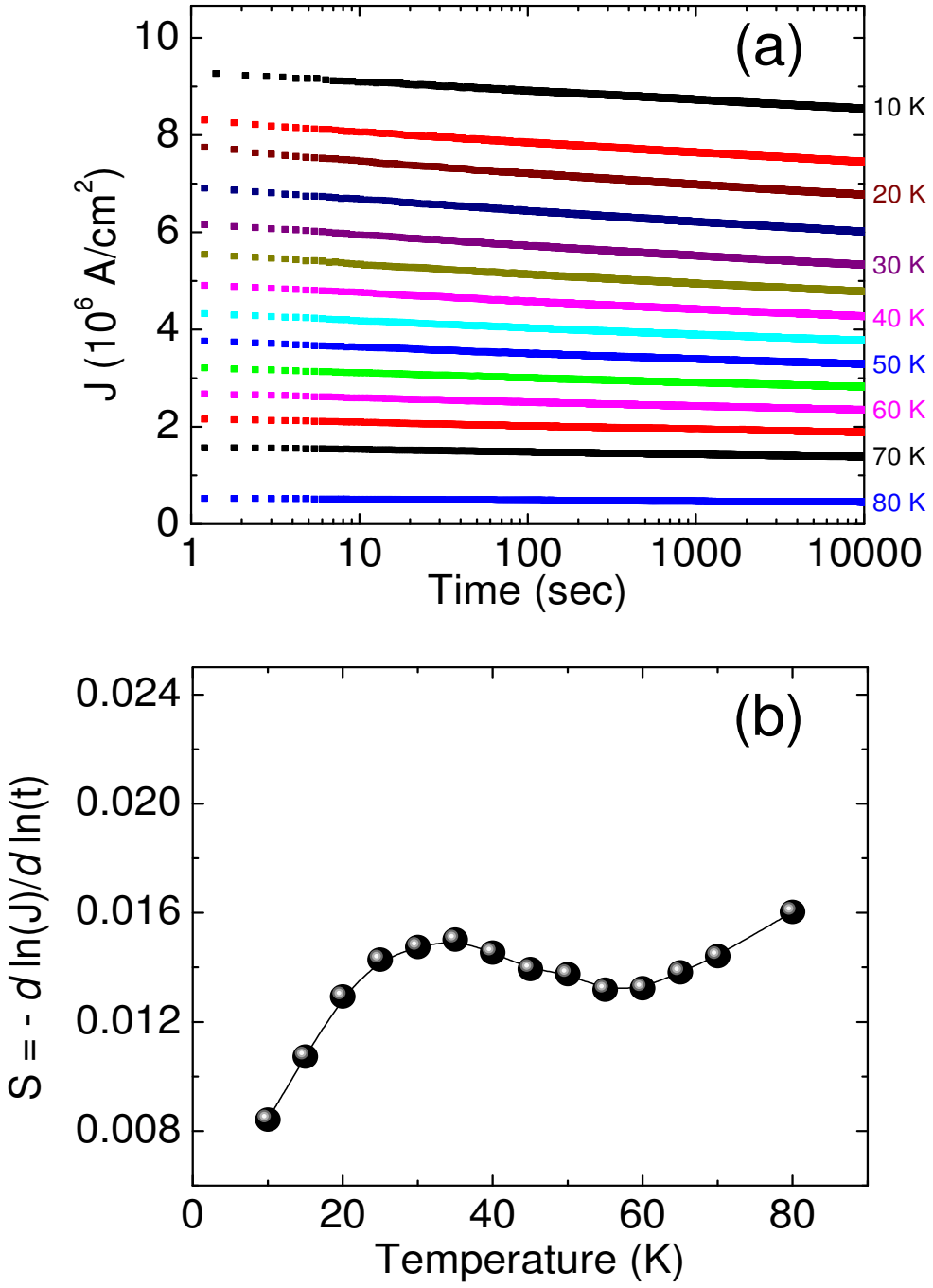

Figure 3.10: (a) Time dependence of the persistent current density J for temperatures ranging from 10 K up to 80 K. (b) Temperature dependence of the dissipation rate S extracted from (a) as explained in the text.

Bibliography

[1] Lei Wang and Shirshak K. Dhali, Supercond. Sci. Technol. **6,** 199 (1993).

[2] C.P. Bean, Rev. Mod. Phys. **36,** 31 (1964).

[3] Charles P. Poole, H. A. Farach, and R. J. Crewswick, *Superconductivity* (Academic Press, San Diego, 1995) 1st edition.

[4] Nicolas Doiron-Leyraud, Cyril Proust, David LeBoeuf, Julien Levallois, Jean-Baptiste Bonnemaison, Ruixing Liang, D. A. Bonn, W. N. Hardy, and Louis Taillefer, Nature **447,** 565 (2007).

[5] H. Darhmaoui, *Critical currents and intrinsic properties in YBCO thin films*, Ph.D. thesis, University of Alberta (1997).

[6] X. Li, M. W. Rupich, T. Kodenkandath, Y. Huang, W. Zhang, E. Siegal, D. T. Verebelyi, U. Schoop, N. Nguyen, C. Thieme, Z. Chen, D. M. Feldman, D. C. Larbalestier, T. G. Holesinger, L. Civale, Q. X. Jia, V. Maroni, and M. V. Rane IEEE Trans. Appl. Supercond. **17,** 3553 (2007).

[7] D. Larbalestier, A. Gurevich, M. Feldmann, and A. Polyanskii, Nature (London) **414,** 368 (2001).

[8] X. Xiong, K. P. Lenseth, J. L. Reeves, A. Rar, Y. Qiao, R. M. Schmidt, Y. Chen, Y. Li, Y. Xie, and V. Selvamanickam, IEEE Trans. Appl. Supercond. **17,** 3375 (2007).

[9] P. N. Barnes, M. D. Sumption, and G. L. Rhoads, Cryogenics **45,** 670 (2005).

[10] T. R. Lamberger, *Physical properties of high temperature superconductors III*, ed. by D. M. Ginsberg (World Scientic, Singapore 1992).

[11] A. I. Mansour, M. Egilmez, I. Fan, K. H. Chow, J. Jung, E. M. Choi, H. S. Lee, S. I. Lee, and H. Darhmaoui, Appl. Phys. Lett. **90,** 162511 (2007)

[12] A. I. Mansour, M. M. Saber, K. H. Chow, and J. Jung, Appl. Phys. Lett. **93,** 142509 (2008).

Chapter 4

Anomalous persistent current flow in underdoped $YBa_2Cu_3O_{7-\delta}$ superconductor

4.1 Introduction

The ability of high temperature superconductors (HTSCs) to carry critical current densities (J_c) as large as 50-70 MA/cm^2 (in modern optimized HTSC epitaxial coatings), makes them of particular interest for technological applications, such as power transmission lines and high magnetic field devices. This has stimulated numerous experimental and theoretical studies [1, 2, 3, 4, 5, 6, 7, 8, 9, 10] aiming at understanding the intrinsic behavior of J_c and its response to the presence of disorder. In cuprate superconductors, such as $YBa_2Cu_3O_{7-\delta}$ (YBCO), oxygen vacancies are an important type of intrinsic disorder [6]. The ordering nature of oxygen vacancies was revealed in the measurements of transmission electron microscopy (TEM) and magnetic hysteresis of YBCO single crystals [11, 12, 13, 14]. The analysis of neutron and infrared vibrational spectra confirm earlier filamentary structural models [7, 15] that the CuO_2 planes contain ferroelastic domains 3-4 nm in diameter. It is believed that these nan-

odomains are responsible for the changes in the electronic and vibronic properties of the material [15]. Previous transport measurements [16] in slightly oxygen deficient YBCO films revealed that, the persistent supercurrent follows filamentary pathways due to the increase in the ferroelastic forces resulting from increasing oxygen vacant sites [15]. This raises a major question about the interplay between oxygen vacancies, their ordering, and the flow of the persistent current as the superconducting system approaches the strongly oxygen deficient limit.

In this study, we report our observation of an anomalous behavior of the persistent current flow in oxygen deficient $YBa_2Cu_3O_{7-\delta}$ ring-shaped thin film. This anomaly was observed within a certain range of oxygen vacancies concentration, and is found to be directly related to the appearance of a spinodal decomposition phase of the oxygen content of YBCO. This study was made possible by carefully and incrementally changing the oxygen content of the same sample, while keeping all other types of disorder intact.

4.2 Experimental details

The measurements of the temperature dependence of the persistent critical current were performed on ring-shaped sample in order to provide direct information about the persistent current density. The experiments were done on a $YBa_2Cu_3O_{7-\delta}$ (slightly over-doped $T_c \approx 88$ K) ring-shaped 0.2 μm thick film of inner and outer diameters 4.6 and 7.2 mm, respectively. The film was deposited on a $\langle 100 \rangle$ oriented $LaAlO_3$ substrate using the rf-magnetron sputtering technique. X-ray diffraction revealed a highly epitaxial film. (Refer to Fig. 3.5 in Sec.2.3 for more details.) A persistent circulating supercurrent was induced in the ring by cooling it in a zero-field to the temperature of interest below T_c, then applying an external magnetic field along the ring's axis and subsequently reducing it to zero. The axial profile of the magnetic self-field $B_z(r)$ of the persistent current was then measured across the ring with a traveling Hall sensor positioned in air at room temperature at a distance of 2.5 mm above the sample surface [17]. The magnitude of the current was obtained from $B_z(r)$ using the Biot-Savart's law. The critical value of the persistent current is reached when $B_z(r)$ becomes independent of the applied magnetic field. (Refer to Chapter 3 for more details about the experimental technique and setup.) This contactless technique enabled us to distinguish between the magnetic field due to the circulating persistent current, and that due to the trapped vortices in the ring's bulk [17, 18]. Hence, we could distinguish between two transition temperatures: (1) the percolative critical temperature (T_c) above which the persistent supercurrent stops to flow in the ring (Fig. 4.1(b)), and (2) the bulk critical temperature (T_c^b) above

which bulk superconductivity ceases to exist in the whole sample (Fig. 4.1(c)), where $T_c \leq T_c^b$. These microscopic transitions are schematically illustrated and explained in Fig. 4.1.

In our experiments, we gradually increased δ and reduced the hole doping, i.e. the number of holes per Cu atom of the CuO_2 planes, by annealing the film in argon gas flow at a temperature of 175°C. This was done a number of times in steps of a few hours each. So, we were able to study 24 different oxygen concentrations of YBCO with T_c reduced from 88 K down to 36 K, while T_c^b reduced from 88 K down to 55.5 K. We used a relatively low annealing temperature in order to ensure that we are removing oxygen from YBCO without affecting its extended defects, such as dislocations and grain boundaries. The measurements of the persistent current density, were performed at temperatures between 10 K and T_c, after each annealing step. The ratio (J_1^o/J_1) increases with an increasing annealing time, and thus was used as an indicator of the disorder level in the material [6, 19]. J_1^o and J_1 are the current densities measured after 1 sec at 10 K in the as-grown and annealed films, respectively.

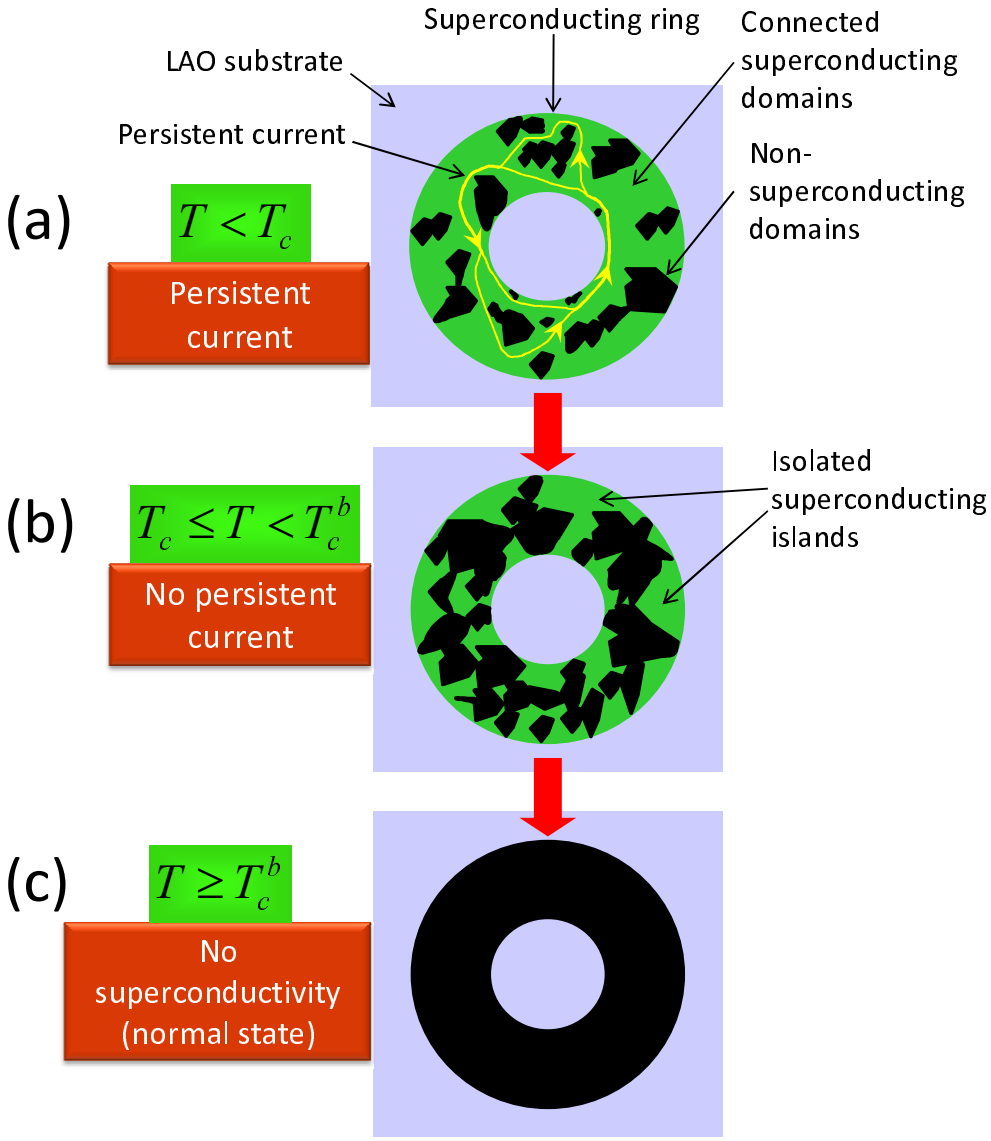

Figure 4.1: Schematic representation of the transitions in the superconducting state of the oxygen deficient ring as we are warming up to higher temperatures. (a) At $T < T_c$, the superconducting domains are connected allowing the flow of the persistent current around the superconducting ring. (b) At $T_c \leq T < T_c^b$, the superconducting domains get isolated hindering the flow of any persistent current. (c) At $T \geq T_c^b$, superconductivity ceases to exist in the whole ring.

4.3 Results and discussion

4.3.1 Temperature dependence of the critical persistent current

In Figure 4.2(a), we show the typical temperature dependence of the normalized critical current density $(J_c(T)/J_c(10K))^{2/3}$ of the YBCO sample at different annealing steps (indicated by the annealing time in hours). The linearity in this dependence is shown as solid straight lines. It indicates a Ginzburg-Landau-like (GL-like) temperature dependence [20], i.e. $\left(\frac{J_c(T)}{J_c(10K)}\right)^{2/3} \propto \left(1 - \frac{T}{T_c}\right)$, and is related to the filamentary flow of the persistent current in the superconductor [15, 18, 20, 21]. The deviation from the GL-like temperature dependence is marked as a cross-over temperature T_{cr}. We used the ratio T_{cr}/T_c, see Fig. 4.2(b), as measure of the percolative flow of the persistent current in the superconductor, where $T_{cr}/T_c \leq 1$. A value of $T_{cr}/T_c = 1$ means that the persistent current is flowing in filamentary (meandered) pathways over the whole temperature range.

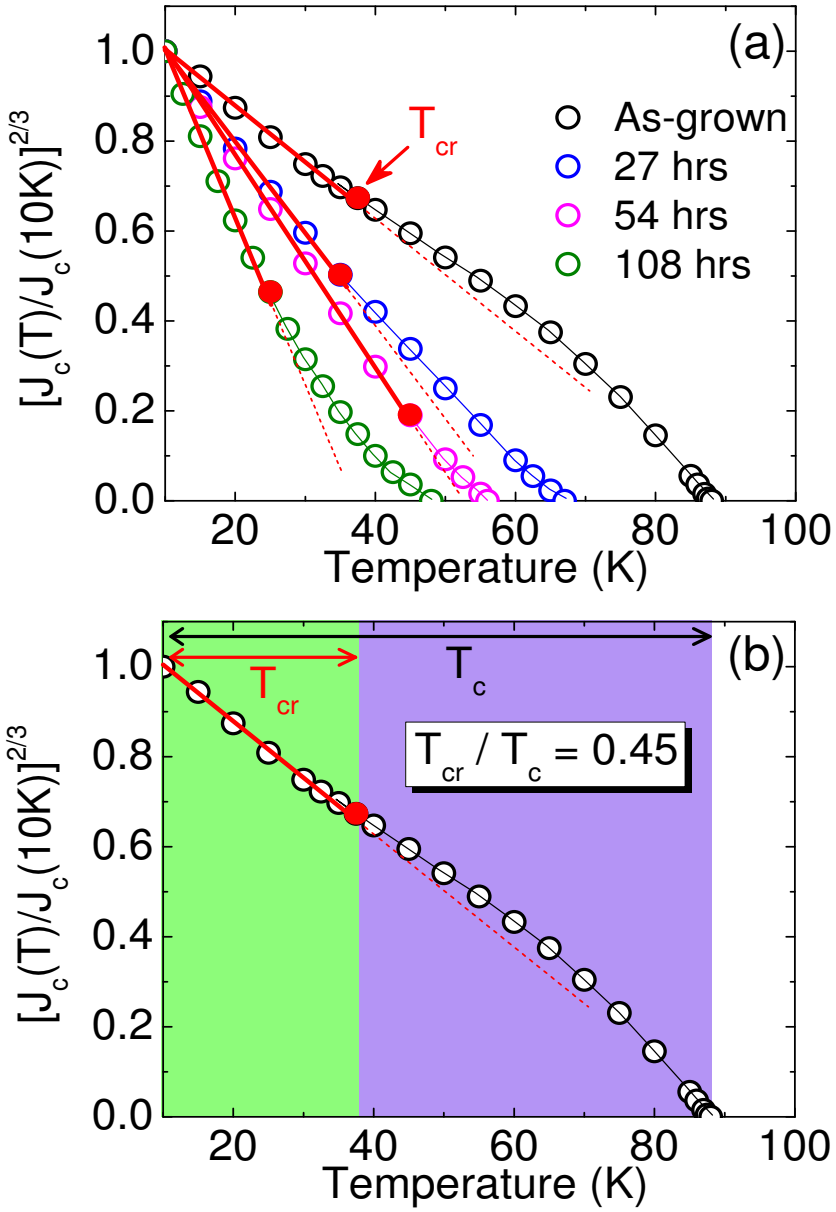

Figure 4.2: (a) Typical Temperature dependence of the normalized persistent critical current density $[J_c(T)/J_c(10K)]^{2/3}$ at different annealing times. The solid straight lines represent the GL-like dependence as explained in the text. The cross-over temperatures T_{cr} are marked as solid circles. (b) An illustration of the use of the ratio T_{cr}/T_c as a measure of the percolative flow of the persistent current in the superconductor (see text).

4.3.2 Disorder dependence of the percolative flow of the persistent current

A plot of percolation (T_{cr}/T_c) as a function of increasing disorder (J_1^o/J_1) is shown in Fig. 4.3. In the first stages of disorder (regions I and II), YBCO gets more percolative where the ratio T_{cr}/T_c increases. This is in agreement with previous observations of increasing percolation in slightly oxygen deficient YBCO thin films [18]. At more oxygen deficient stages (region III), the percolative flow of the persistent current exhibits a sharp dip and rise, followed by a monotonic decrease at very high disorder levels (strongly oxygen deficient) in region IV. The important observation here, is the anomaly revealed in region III of Fig. 4.3. In fact, we can rule out the possibility that the $J_c(T)$ anomaly is due to changes in the pinning mechanism of the vortices in the GL region, i.e. at $T \leq T_{cr}$. In Fig. 4.4(a) we show the temperature dependence of the dissipation rate ($S = -dlnJ/dlnt$) at different disorder levels and we indicate the cross-over temperature T_{cr} that was concluded from $J_c(T)$. The analysis of the variation of the dissipation rate ($S = -dlnJ/dlnt$) at $0.9T_{cr}$, T_{cr}, and at $1.1T_{cr}$ reveals that S has the same trend as a function of disorder (see Fig. 4.4(b)). This means that the increasing disorder has the same effect on the pinning of the vortices whether we are in the GL-regime (at $0.9T_{cr}$ and T_{cr}) or above it (at $1.1T_{cr}$). This leaves us with one possibility that the observed changes in $J_c(T)$ (specifically region III of of Fig. 4.3) are solely due to changes in the pathways of the flowing persistent current.

In order to explain the source of this behavior, we need to look at what is happening at the microscopic level of YBCO as we are removing oxygen. This can be

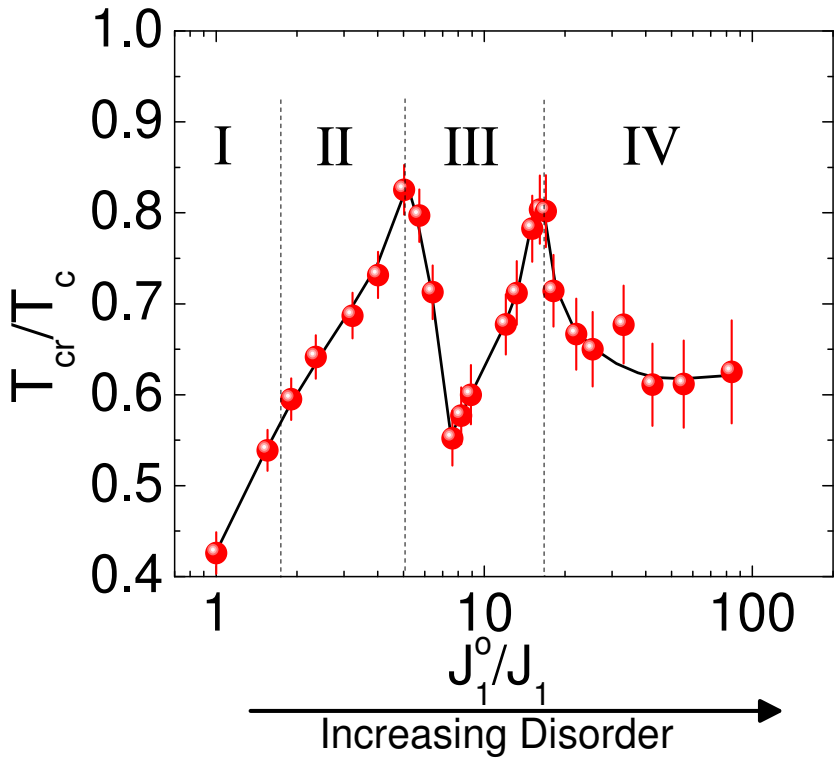

Figure 4.3: Disorder dependence of the percolative flow of the persistent current. The anomaly revealed in region III is explained in the text. The solid curve is a guide for the eye.

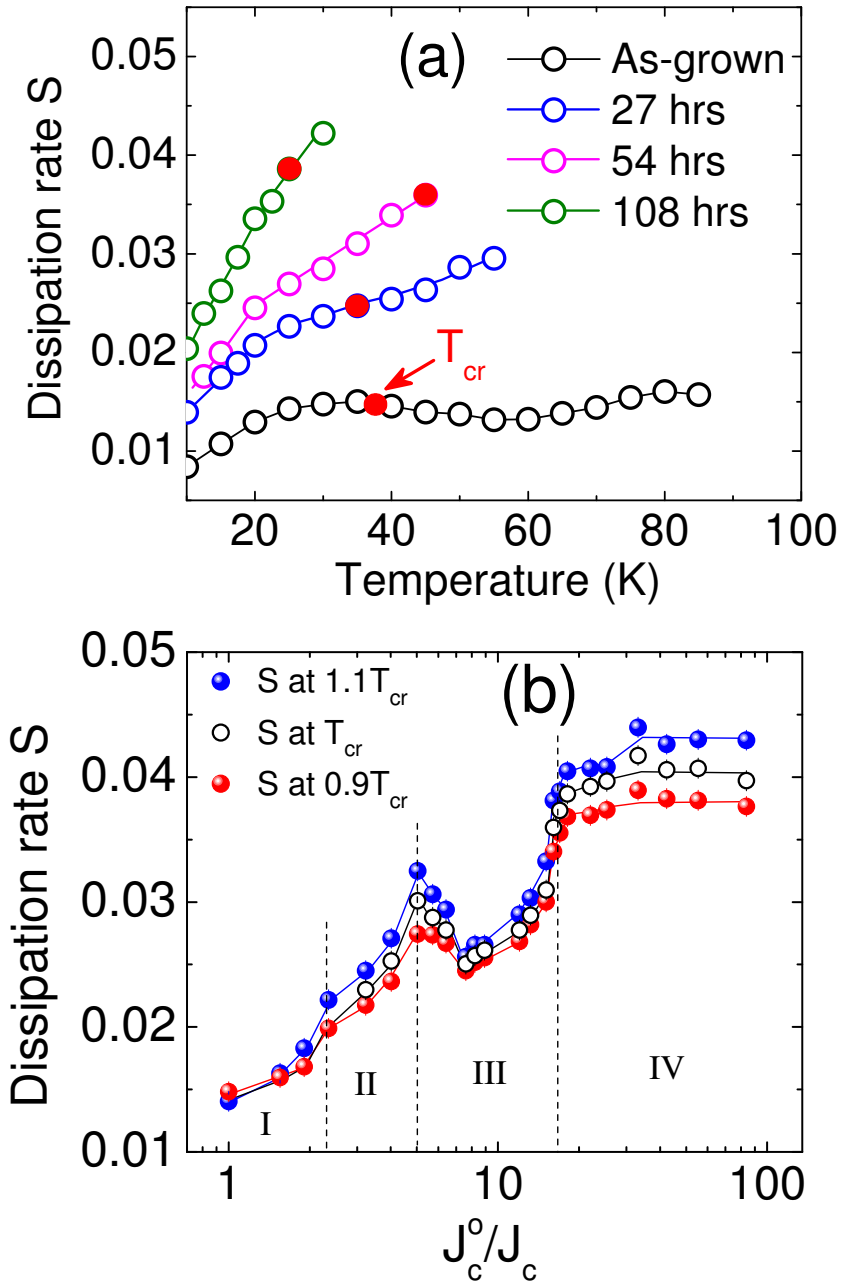

Figure 4.4: (a) Typical temperature dependence of the normalized dissipation rate $S = -dlnJ/dlnt$ for the same annealing times shown in Fig. 4.2, where the values of the crossover temperature T_{cr} are obtained from $J_c(T)$ (see text). (b) Disorder dependence of the dissipation rate at T_{cr}, $0.9T_{cr}$, and $1.1T_{cr}$. The solid curves are guides for the eye.

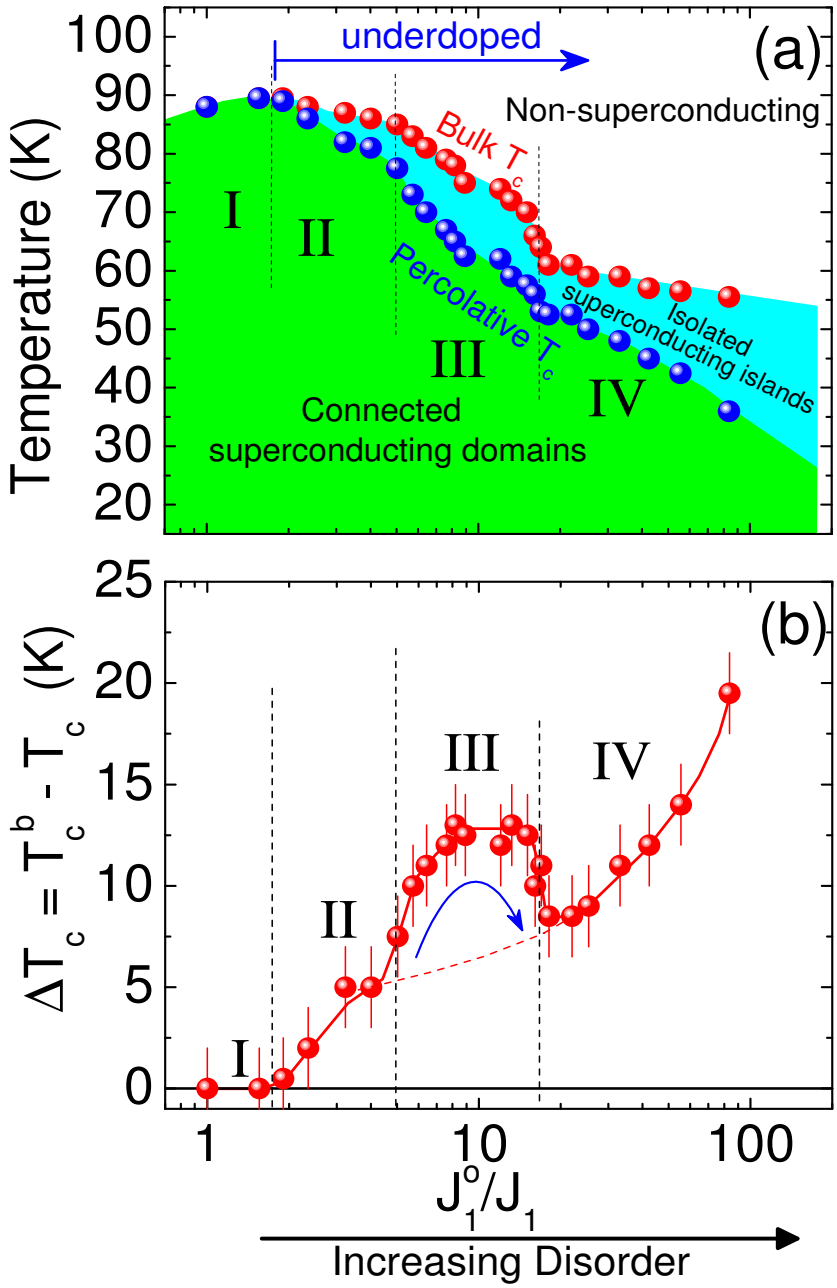

Figure 4.5: Disorder dependence of; (a) the bulk and percolative transition temperatures T_c^b and T_c, respectively, and (b) their difference $\Delta T_c = T_c^b - T_c$. The solid curves are guides for the eye.

attained, indirectly, by monitoring the changes in the bulk and percolative transition temperatures (T_c^b and T_c) as the concentration of oxygen vacancies is being increased. In Figure 4.5(a), we plot T_c^b and T_c as function of disorder. The difference between these two temperatures ($\Delta T_c = T_c^b$ - T_c) versus disorder is shown in Fig. 4.5(b). The value of ΔT_c reveals the difference in the hole doping level between the oxygen rich domains (superconducting grains SGs), and the oxygen deficient domains (grain boundaries or weak links WLs). It is known that oxygen vacancies segregate into the grain boundaries [22, 23, 24], which makes them more oxygen deficient than the bulk grains. The as-grown YBCO film is expected to be uniform with the same hole doping level over all the sample. This is verified in the zero value of ΔT_c, where the two temperatures T_c^b and T_c are the same. Also, this seems to be valid in the first annealed sample (see region I of Fig. 4.5(a-b)). At higher levels of disorder (region II), ΔT_c starts to increase revealing a significant difference in the hole doping of the SGs and WLs. Removing oxygen further from YBCO leads to a distinctive behavior of ΔT_c in region III, after which it increases monotonically in region IV.

At this point, we will focus our analysis on region III in Fig. 4.5(b). The flat trend of ΔT_c followed by a sharp decrease means that there is oxygen redistribution inside the sample, in addition to the global decrease of the oxygen content. This redistribution can be explained as an internal flow of oxygen atoms from the oxygen rich domains (SGs) to the oxygen deficient domains (WLs). In fact, this is a signature of a spinodal decomposition mechanism [7, 8, 9, 10], where there is a competition between two coexisting phases, oxygen rich and oxygen deficient, as the concentration

of oxygen vacancies is being increased. This also agrees with the proposition that [8] transient ordered phases of local oxygen vacancy concentrations may form during the spinodal decomposition in YBCO. If we now combine the picture in region III of both Figures 4.3 and 4.5(b), we can infer that the anomaly revealed in the percolative flow of the persistent current was a direct response to the occurrence of the spinodal decomposition of oxygen vacancies in YBCO. This represents strong evidence that the persistent current flow is very sensitive to both the oxygen content and distribution mechanisms in high temperature superconductors, such as YBCO.

4.4 Conclusion

In conclusion, we observed an anomalous behavior of the persistent current flow within a certain range of oxygen vacancies concentration in $YBa_2Cu_3O_{7-\delta}$. The anomaly in the persistent current flow is found to be directly related to the appearance of a spinodal decomposition phase of the oxygen content of YBCO. This observation was made possible, by carefully and incrementally changing the oxygen content of the same sample. These results reveal the sensitivity of the persistent current to the oxygen content and distribution in YBCO, and provide useful information for applications that require better understanding of the behavior of the supercurrent.

Bibliography

[1] J. Halbritter, J. Supercond.: Incorporating Novel Magnetism **16,** 833 (2003); Phys. Rev. B **48,** 9735 (1993).

[2] J. D. Jorgensen, B. W. Veal, A. P. Paulikas, L. J. Nowicki, G. W. Crabtree, H. Claus, and W. K. Kwok, Phys. Rev. B **41**, 1863 (1990).

[3] Y. Zhu, Z. X. Cai, R. C. Budhani, M. Suenaga, and D. O. Welch, Phys. Rev. B **48,** 6436 (1993).

[4] L. Civale, A. D. Marwick, M. W. McElfresh, T. K. Worthington, A. P. Malozemoff, F. H. Holtzberg, J. R. Thompson, and M. A. Kirk, Phys. Rev. Lett. **65,** 1164 (1990).

[5] J.J. Calabrese , M. A. Dubson, and J. C. Garland, J. Appl. Phys. **72,** 2958 (1992); G. Xiao, F. H. Streitz, M. Z. Cieplak, A. Bakhshai, A. Gavrin, and C. L. Chien, Phys. Rev. B **38,** 776 (1988); H. Ikuta, and D.M. Ginsberg, J. Supercond. **9,** 259 (1996); E. Gaganidze and J. Halbritter, Supercond. Sci. Technol. **17,** 1346 (2004); J. Kurian, P. R. S. Wariar, P. K. Sajith, and J. Koshy, J. Supercond. **11,** 683 (1998); K.V. Paulose, M. K. Jayarajt, J. Koshy, and A. D. Damodaran, Supercond. Sci. Technol. **6,** 257 (1993).

[6] G. Blatter, M. V. Feigel'man, V. B. Geshkenbein, A. I. Larkin, and V. M. Vinokur, Rev. Mod. Phys. **66,** 1125 (1994).

[7] J.C. Phillips, Phys. Rev. Lett. **64,** 1606 (1990); J. Supercond.: Incorporating Novel Magnetism **15,** 393 (2002); Phys. Rev. Lett. **88,** 216401 (2002)

[8] A.G. Khachaturyan and J.W. Morris, Phys. Rev. Lett. **61,** 215 (1988); A. G. Khachaturyan, S. V. Semenovskaya, and J. W. Morris, Phys. Rev. B **37,** 2243 (1988).

[9] D. de Fontaine, G. Ceder, and M. Asta , Nature **343,** 544 (1990).

[10] L. T. Wille, A. Berera, and D. de Fontaine, Phys. Rev. Lett. **60,** 1065 (1988).

[11] J.L. Vargas and David C. Larbalestier, Appl. Phys. Lett. **60,** 1741 (1992).

[12] C.L. Johnson, Jan K. Bording, and Yimei Zhu, Phys. Rev. B **78,** 014517 (2008).

[13] R. Beyers, B. T. Ahn, G. Gorman, V. Y. Lee, S. S. P. Parkin, M. L. Ramirez, K. P. Roche, J. E. Vazquez, T. M. Gür, and R. A. Huggins, Nature **340,** 619 (1990).

[14] R.J. Cava, A.W. Hewat, E.A. Hewat, B. Batlogg, M. Marezio, K.M. Rabe, J.J. Krajewski, W.F. Peck Jr., and L.W. Rupp Jr., Physica C **165,** 419 (1990).

[15] J.C. Phillips and J. Jung, Phil. Mag. B **81,** 745 (2001); Phil. Mag. B **82,** 1163 (2002).

[16] J. Jung, K.H. Chow, M. Egilmez, and A. Welsh, Appl. Phys. Lett. **87,** 262506 (2005).

[17] A.I. Mansour, M. M. Saber, K. H. Chow, and J. Jung, Appl. Phys. Lett. **93,** 142509 (2008).

[18] H. Darhmaoui, J. Jung, J. Talvacchio, M. A-K. Mohamed, and L. Friedrich, Phys. Rev. B **53,** 12330 (1996).

[19] A.I. Mansour, R. Ma, M. Egilmez, M.M. Saber, I. Fan, K.H. Chow, and J. Jung, Phys. Rev. B **79**, 172504 (2009).

[20] J. R. Clem, B. Bumble, S. I. Raider, W. J. Gallagher, and Y. C. Shih, Phys. Rev. B **35,** 6637 (1987).

[21] A.I. Mansour, M. Egilmez, I. Fan, K. H. Chow, J. Jung, E. M. Choi, H. S. Lee, S. I. Lee, and H. Darhmaoui, Appl. Phys. Lett. **90**, 162511 (2007).

[22] R. F. Klie, J. P. Buban, M. Varela, A. Franceschetti, C. Jooss, Y. Zhu1, N. D. Browning, S. T. Pantelides, and S. J. Pennycook, Nature **435,** 475 (2005).

[23] N. D. Browning, J. P. Bubana, P. D. Nellist, D. P. Nortonb, M. F. Chisholmb, and S. J. Pennycookb, Physica C **294,** 183 (1998).

[24] Y. Zhu, J. M. Zuo, A. R. Moodenbaugh, and M. Suenaga, Phil. Mag. A **70,** 969 (1994).

Chapter 5

Evolution of self-organized bulk vortex structure induced by hole doping in the high-temperature superconductor $YBa_2Cu_3O_{7-\delta}$

5.1 Introduction

Vortex matter in high temperature superconductors, including the interaction of magnetic vortices with impurities, as well as the response of these vortices to external magnetic fields, has been intensively investigated, both theoretically and experimentally [1, 2, 3, 4, 5]. In defect-free superconductors an electric current flowing inside the sample induces vortex motion, causing resistance and subsequent dissipation of the supercurrent [2]. Pinning the vortices by lattice defects hinders this dissipative process, deforms the vortex structure, and increases the critical currents. Studies of the (H,T) phase diagram of the vortex structure have been conducted using the (equilibrium) thermodynamical approach, i.e., by probing the response of the vortex structure to external magnetic fields (H) applied at different temperatures below T_c [4, 5, 6]. It has been shown by equilibrium magnetization and specific heat measure-

ments [4] that high magnetic fields can melt the vortex lattice. These measurements have identified lattice, glass, and liquid vortex phases at some fixed defect concentration levels. However, the nature of the vortex phase diagram, and especially the significance of scaling exponents, remains controversial. Recently, it was suggested that a good description of the phase diagram would utilize scaling exponents from smectic liquid crystalline phases, which produces resistivity-electric field exponents that vary by a factor of 15 [7].

The response of the vortex structure to successive infinitesimal disorder levels in the $J << J_c$ limit [3] is of considerable interest to theorists who study vortex pinning in superconductors since it is one of the key elements that determines the statistical mechanics and the dynamics of the vortex system. Although there were many studies of vortex creep in granular structures in the early 1990's, Blatter *et al.* [3] suggested in 1994 that "A systematic experimental study of the correlation between oxygen defect concentration and the critical current density [in single crystals] would be highly desirable."

Oxygen vacancies are an important example of intrinsic disorder, and can be created in a superconductor by annealing, for example. The vacancies change the hole doping level of the material, which in turn determines the superconducting order parameter of the sample and, therefore, its properties such as the transition temperature (T_c) and the superfluid density, as well as the vortex structure. This implies that one way to investigate the intrinsic disorder-induced vortex structure in bulk superconductors is to study the time evolution, i.e., relaxation, of the persistent current

generated in the superconductor in samples with different oxygen defect concentrations [3]. The nature of the vortex structures and their pinning in the presence of the persistent current can be inferred from the value of the exponent μ, a parameter in the scaling relation [3, 8, 9] between the effective energy barrier against vortex motion U_{eff} and the persistent current density J, i.e. $U_{eff}(J) \propto (J_c/J)^{\mu}$, where J_c is the critical current density. Furthermore, the critical current density ratio in the as-grown and annealed samples can be used as an indicator of the strength of the disorder [3].

In this study, we investigated the evolution of the vortex structure inferred from measurements of the persistent current relaxations of 24 different oxygen contents (with δ changing from 0.03 to 0.55 in steps of about 0.021) of the same $YBa_2Cu_3O_{7-\delta}$ ring-shaped epitaxial films. This type of measurement is equivalent to that of the remanent magnetization trapped in a superconductor at a zero external magnetic field. This has enabled us to map out the phase diagram of the vortex structure (the vortex structure exponent μ versus δ) in $YBa_2Cu_3O_{7-\delta}$. We found that an increase of disorder (increase of δ) leads to the transformation of the vortex quasi-lattice into a glass and subsequently into a pinned liquid. These vortex phases self-organize and produce relaxation plateaus in regions between step-like changes in the dependence of the relaxation kinetics on the hole doping, showing an important correlation between the vortex structure and the hole-doping level in $YBa_2Cu_3O_{7-\delta}$ films.

5.2 Experimental Details

The relaxation of the persistent current was measured on ring-shaped samples in order to provide the information on both the vortex-motion-induced persistent current decay and the persistent current density. The experiments were done on $YBa_2Cu_3O_{7-\delta}$ (slightly over-doped with $T_c \approx 88$ K) ring-shaped 0.2 μm thick films of inner and outer diameters 4.6 and 7.2 mm, respectively. The films were deposited on a $\langle 100 \rangle$ oriented $LaAlO_3$ substrate using the rf-magnetron sputtering technique. X-ray diffraction revealed highly epitaxial films. A persistent circulating supercurrent was induced in the ring by cooling it in a zero-field to the temperature of interest below T_c, then applying an external magnetic field along the ring's axis and subsequently reducing it to zero. The axial profile of the magnetic self-field $B_z(r)$ of the persistent current was then measured across the ring with a traveling Hall sensor positioned in air at room temperature at a distance of 2.5 mm above the sample surface [10]. The magnitude of the current was obtained from $B_z(r)$ using the Biot-Savart's law. The critical value of the persistent current is reached when $B_z(r)$ becomes independent of the applied magnetic field. This is a contactless technique which allows one to distinguish between the magnetic field due to the circulating persistent current and that due to the trapped vortices in the rings bulk [11].

In our experiments, we gradually increased δ and reduced the hole doping p, i.e., the number of holes per Cu atom of the CuO_2 planes, by annealing the film in flowing argon at a temperature of 175°C. This was done a number of times in steps of a few hours each so that T_c was reduced from 88 K down to 55.5 K. The relatively

low annealing temperature ensured the reduction of the hole doping by removing oxygen from YBCO without affecting extended defects, such as dislocations, grain boundaries, etc. The measurements of the persistent current density and its time dependence up to 10^4 seconds, were performed at temperatures between 10 K and T_c in 5 K steps, after each annealing step. The ratio (J_1^o/J_1), where J_1^o and J_1 are the current densities measured after 1 sec at 10 K in the as-grown and annealed films, respectively, has been used as an indicator of the disorder level in the material [3]. (J_1^o/J_1) increases with an increasing annealing time.

5.3 Results and Discussion

5.3.1 Effect of disorder on the temperature dependence and the dissipation rate of the persistent current

Figure 5.1(a) shows selected $J(T,t)$ curves for the YBCO thin-film-ring at different levels of disorder J_1^o/J_1. The length of the vertical traces of J at each temperature in Fig. 5.1(a) indicates the decay of J at a specific disorder level over a time interval between 1 and 3600 sec. The time dependence of the persistent current density $J(t)$ at different temperatures was used to calculate the dependence of the normalized decay rate (the creep rate) $S = -dln(J)/dln(t)$ on temperature, which is a result of the dissipative motion of the vortices over an effective energy barrier U_{eff}. Fig. 5.1(b) shows selected curves of $S(T)$ demonstrating the change of $S(T)$ with an increasing disorder. Typical dependence of S on the disorder level is shown in Fig. 5.1(c) for a constant temperature of 20 K. The increase of S with the disorder indicates an

ongoing softening process of the vortex structure and the resulting creep of vortices.

5.3.2 Disorder effects on the vortex structure

In order to obtain information about the vortex structure at different levels of disorder, Maley's scheme [8] could be applied to calculate the critical exponent μ in the dependence of the energy barrier on the current density $U_{eff}(J) \propto (J_c/J)^{\mu}$. The decay rate of the persistent current dJ/dt from the critical level in a zero external magnetic field (which is equivalent to the decay rate of the remanent magnetization) depends on the energy barrier $U(J)$ as $dJ/dt \propto -J_o \exp[-U(J)/k_BT]$, where J_o is the current density close to the critical current value [12]. The energy barrier could then be extracted from this equation as $U(J,T) \simeq -k_BT\{\ln|(dJ/dt)/J_o| - C\}$, where k_B is the Boltzmann constant. C is a constant that can be adjusted in order to ensure that $U(J)$ is a continuous function of J at low temperatures [8]. In order to find U, the decay rate dJ/dt was first calculated from the measured decay of the current density $J(t)$ over a time interval of 60-3600 sec. J_o was selected as the experimentally accessible current density recorded 1 second after the critical state was established in the ring. Then a factor $-k_BTln[|(dJ/dt)/J_o|]$ in $U(J,T)$ was plotted as a function of J (see Fig. 5.2(a)). Multiple segments seen in this plot were measured at different temperatures between 10 K and T_c. By choosing an appropriate value of a constant C (≈ 21.5, for all doping levels $C = 20 \pm 3$) it was possible to align these segments at low temperature (see Fig. 5.2(b)). Subsequent division of $U(J,T)$ by a thermal factor $g(T) \leq 1$ [12, 9], gave a piecewise continuity of all the segments (see

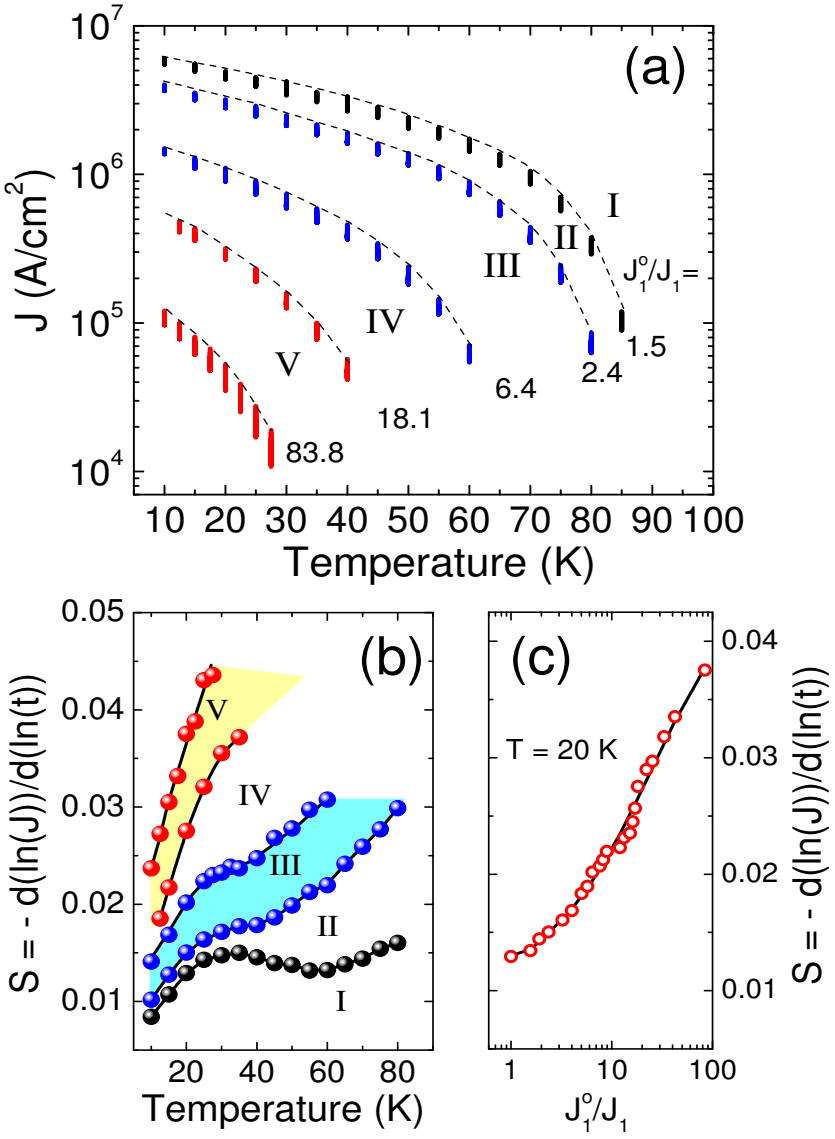

Figure 5.1: (a) Temperature dependence of the persistent current density J at selected levels of disorder indicated by the ratio (J_1^o/J_1) (thin dashed lines). The vertical traces show the dependence of $J(T,t)$ on time. (b) Temperature dependence of the normalized decay rate S of the persistent current density corresponding to the same disorder levels as in (a). Regions I-V are explained in the text. (c) S as a function of (J_1^o/J_1) for a constant temperature of 20 K. (The lines are guides to the eye).

Fig. 5.2(c)). The thermal factor $g(T)$ was found to be almost the same irrespective of the doping level (see the inset in Fig. 5.2(c)). The resulting effective energy barrier $U_{eff}(J) = U(J,T)/g(T) \propto (J_c/J)^{\mu}$ has been used to calculate the critical exponent μ.

For each value of the doping level, the value of μ was calculated from the dependence $U_{eff} \propto (J_c/J)^{\mu}$ for current densities less than $0.7J_c$. This range of J was selected in order to ensure that the Lorentz force on the vortex structure is relatively low and the above equation is satisfied [3, 13, 12].

Selected curves of $U_{eff}(J) = U(J,T)/g(T)$ (the Maley plots) labelled I to V are shown in Fig. 5.3(a) for different levels of disorder. The analysis of the persistent current relaxations enabled us to construct the phase diagram (δ,μ) of the vortex structure shown in Fig. 5.3(b). It shows the evolution of the vortex structure and the hole doping level p as a function of an increasing disorder level. In order to calculate the value of the hole doping of the disordered film, we used the dependence of p on T_c which was measured for YBCO single crystals [14]. Vortex-phases in this diagram are identified by the value of the critical exponent (the vortex-structure-order parameter) μ [3, 13], obtained as described above. Vortices in the as-grown film are expected to be arranged in a quasi-long range ordered lattice [15]; therefore we have assigned this state, and hence Region I in Fig. 5.3(b), accordingly (the Bragg "lattice" phase).

As mentioned in the introduction, it is well known that an increasing magnetic field can produce changes in the vortex phase [4]. Interestingly, we observed that even in the absence of an applied magnetic field, the original vortex structure in

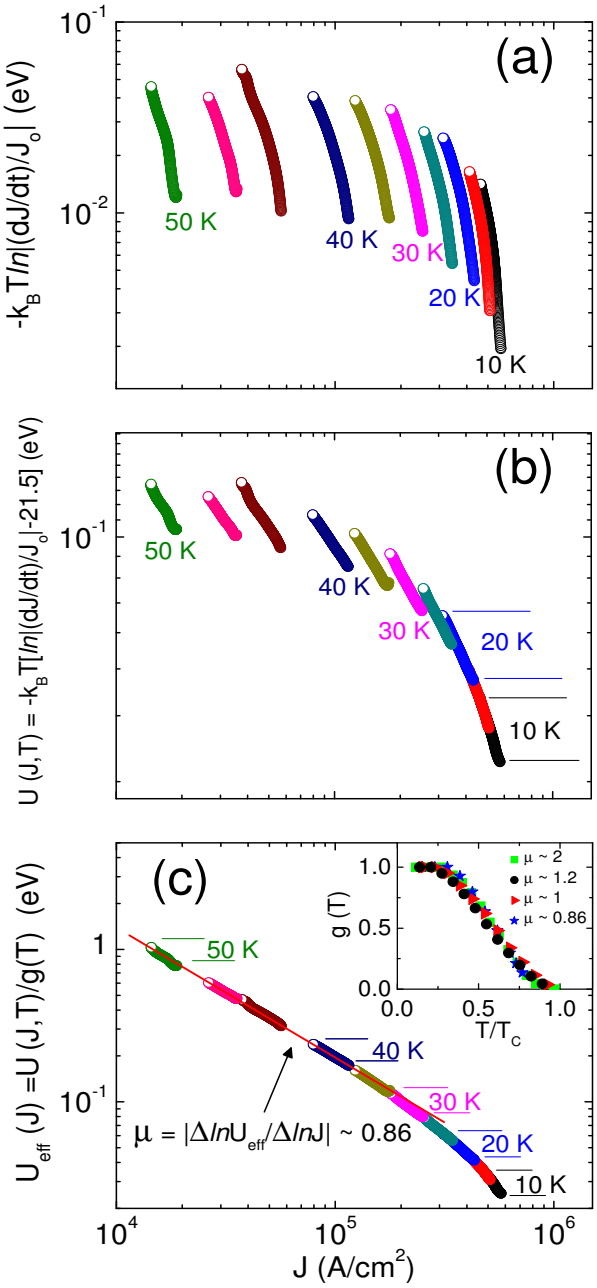

Figure 5.2: (a) Plot of the expression $-k_BTln|(dJ/dt)/J_o|$ as a function of the current density J, which displays vertically shifted segments (see text). (b) Plot of $U(J,T) \simeq -k_BT[ln|(dJ/dt)/J_o|-21.5]$ as a function of J, for a constant C adjusted to 21.5 which aligns the low temperature segments. (c) The effective energy barrier $U_{eff}(J) = U(J,T)/g(T) \propto (J_c/J)^{\mu}$ versus J. Inset: thermal factors $g(T)$ corresponding to several different doping levels and $\mu \sim 2$, 1.2, 1, and 0.86.

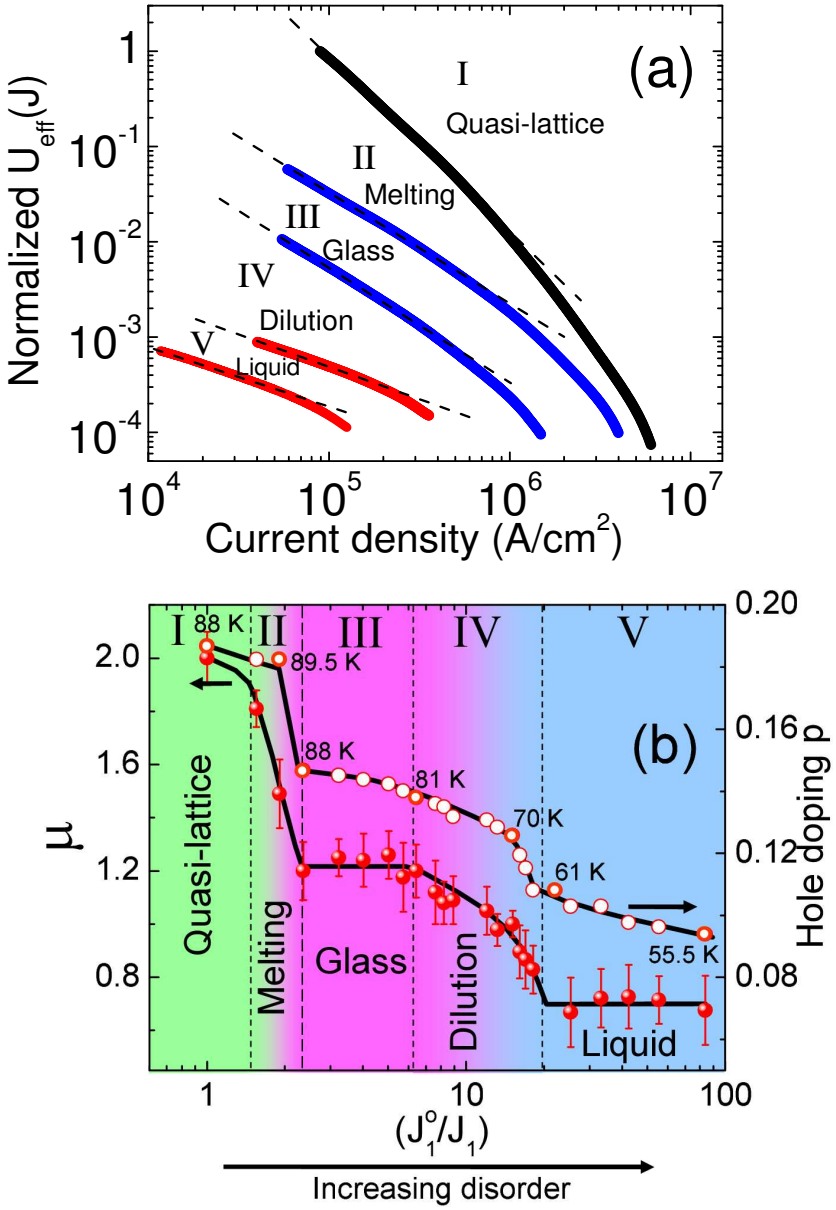

Figure 5.3: (a) Maley's plots showing the dependence of $U_{eff}(J)$ (normalized to that of the as grown sample at $J \sim 10^5$ A/cm^2) on the current density for different disorder levels. The dashed lines indicate the regions of J for which μ was calculated (see text). (b) Evolution of the vortex structure represented by the change of the critical exponent μ (solid spheres) and hole doping number p (open circles) as a function of disorder J_1^o/J_1 in YBCO. Three different vortex-phases as well as two transition stages (melting and dilution) are shown. Temperatures mark T_c's for selected hole-doping numbers. Solid lines are guides to the eye.

the film can be subsequently deformed/melted upon increasing the intrinsic lattice disorder in the sample. In particular, Figure 5.3(b) shows that μ strongly depends on the disorder level in YBCO film. We measured μ in two films with similar results obtained. Starting with the vortex quasi-lattice in the as-grown film with $\mu_c \sim 2.0 \pm 0.1$ (region I), a small change of the disorder level (J_1^o/J_1) causes a dramatic drop (region II) in the critical exponent down to $\mu_g \sim 1.22 \pm 0.04$. The latter value is consistent with $\mu \sim 1$ of the glass phase observed in YBCO [16]. We attribute this drop to a melting transition of the vortex quasi-lattice phase into a glass-like phase (region III) which has shorter range order. The glass phase persists over a wider range of intrinsic disorder than the quasi-lattice phase. As the level of disorder is increased further, the value of μ drops monotonically (region IV) until it eventually plateaus at a sublinear value of $\mu_l \sim 0.71 \pm 0.03$ (region V). We assign Region V to a pinned liquid phase and therefore in Region IV, a dilution process is taking place where both vortex glass and liquid phases coexist. The assignment of $\mu_l \sim 0.71$ to a liquid phase (Region V) is made because of comparisons with theory, such as the calculations from a Gibbsian droplet nucleation model of bulging elastic vortices [3]. Similar values of $\mu_l \sim 0.77$ have been reported for magnetic relaxation in a vortex liquid in $HgBa_2Ca_2Cu_3O_{8+\delta}$ thin films [17].

An increase of the concentration of oxygen vacancies reduces the coupling between the CuO_2 planes [18] and leads to a "monotonic" increase of the anisotropy of YBCO [19]. Hence the changes of anisotropy can not be correlated with the observed plateaus in μ. Moreover, in the range of T_c's between 86.8 K and 92 K (for $\delta \leq 0.11$), where

dramatic changes in μ are observed (see regions I-III in Fig. 5.3(b)), the changes in anisotropy are very small [20].

Upon re-oxygenating the film, μ recovers to a value of 1.98 ± 0.11 which is close to that of $\sim 2.0 \pm 0.1$ found in the as-grown sample prior to deoxygenation. This indicates that our observations are reversible. The results for μ_c, μ_g, and μ_l imply that an important correlation exists between the vortex structure and the hole doping of the CuO_2 planes. The hole doping decreases gradually with an increasing disorder level in a step-like manner. The steps occur at the boundaries between regions II and III, and between regions IV and V, i.e., at the onsets of the formation of the vortex-glass and vortex-liquid phases. Power-law scaling (characteristic of self-organized structures [21]) is not predicted by recent formal theories based on collective pinning by randomly distributed dopants [22], but it is predicted, with a sublinear scaling exponent of the liquid phase ($\mu_l \sim 0.71$), by nucleation of vortex bulges [3], which gives $\mu_l = (6 - d)/4$, or 0.75 for d=3, i.e. three-dimensional vortices (with kinks). So far, nucleation theory has no explanation for the superlinear exponents reported here for the strongly correlated (self-organized) lattice ($\mu_c \sim 2$) and glass ($\mu_g \sim 1.22$) phases. The wide region corresponding to the glass phase, with its constant μ_g, is not predicted by most theories, but a similarly wide region has been observed in the phase diagrams of network glasses, where it was called the intermediate phase [23, 24]. This self-organized phase has special elastic and thermal properties [25] analogous to the creep of glassy vortex arrays in high temperature superconductors.

5.4 Conclusion

We found that the evolution of the vortex structure of $YBa_2Cu_3O_{7-\delta}$ correlates with the changes in the hole doping level in the CuO_2 planes. As δ increases the collective lattice self-organization of the as-grown sample decreases, leading to the formation of vortex-glass and vortex-liquid phases. These vortex phases form in regions between step-like changes in the dependence of the hole doping on disorder, corresponding to mixed phases. The fundamental results of our studies should stimulate further development and renewed interest of theories of the vortex structure and its response to intrinsic lattice disorder and/or a hole doping level in high temperature superconductors.

Bibliography

[1] A. A. Abrikosov, Rev. Mod. Phys. **76,** 975 (2004).

[2] Y. B. Kim, C. F. Hempstead, and A. R. Strnad, Phys. Rev. **139,** A1163 (1965).

[3] G. Blatter , M. V. Feigel'man, V. B. Geshkenbein, A. I. Larkin, and V. M. Vinokur, Rev. Mod. Phys. **66,** 1125 (1994).

[4] F. Bouquet, C. Marcenat, E. Steep, R. Calemczuk, W. K. Kwok, U. Welp, G. W. Crabtree, R. A. Fisher, N. E. Phillips, and A. Schilling, Nature **411,** 448 (2001).

[5] J. Kierfeld and V. Vinokur, Phys. Rev. B **69,** 024501 (2004); Phys. Rev. B **61,** R14928 (2000).

[6] H. Beidenkopf, N. Avraham, Y. Myasoedov, H. Shtrikman, E. Zeldov, B. Rosenstein, E. H. Brandt, and T. Tamegai, Phys. Rev. Lett. **95,** 257004 (2005).

[7] S. A. Baily, B. Maiorov, H. Zhou, F. F. Balakirev, M. Jaime, S. R. Foltyn, and L. Civale, Phys. Rev. Lett. **100,** 027004 (2008).

[8] M. P. Maley, J. O. Willis, H. Lessure, and M. E. McHenry, Phys. Rev. B **42,** 2639 (1990).

[9] J. R. Thompson, L. Krusin-Elbaum, L. Civale, G. Blatter, and C. Feild, Phys. Rev. Lett. **78,** 3181 (1997).

[10] A. I. Mansour, M. Egilmez, I. Fan, K. H. Chow, J. Jung, E. M. Choi, H. S. Lee, S. I. Lee, and H. Darhmaoui, Appl. Phys. Lett. **90,** 162511 (2007); A. I. Mansour, M. M. Saber, K. H. Chow, and J. Jung, Appl. Phys. Lett. **93,** 142509 (2008).

[11] H. Darhmaoui, J. Jung, J. Talvacchio, M. A-K. Mohamed, and L. Friedrich, Phys. Rev. B **53,** 12330 (1996).

[12] M. Nideröst, A. Suter, P. Visani, and A. C. Mota, G. Blatter, Phys. Rev. B **53,** 9286 (1996).

[13] C. J. van der Beek, P. H. Kes, M. P. Maley, M. J. V. Menken, and A. A. Menovsky, Physica C **195,** 307 (1992).

[14] R. Liang, D. A. Bonn, and W. N. Hardy, Phys. Rev. B **73,** 180505(R) (2006).

[15] R.H. Koch, V. Foglietti, W. J. Gallagher, G. Koren, A. Gupta, and M. P. A. Fisher, Phys. Rev. Lett. **63,** 1511 (1989).

[16] A. P. Malozemoff and M. P. A. Fisher, Phys. Rev. B **42,** 6784 (1990).

[17] M. H. Kim, S. I. Lee, M. S. Kim, and W. N. Kang, Supercond. Sci. Tech. **18,** 835 (2005).

[18] W. Lang, W. Gob, W. Kula, and R. Sobolewski, Z. Phys. B **98**, 453 (1995).

[19] T.R. Chien, W. R. Datars, B. W. Veal, A. P. Paulikas, P. Kostic, Chun Gu, and Y. Jiang, Physica C **229**, 273 (1994); M. Putti, M. R. Cimberle, C. Ferdeghini, G. Grassano, D. Marrè, A. S. Siri, A. A. Varlamov, and L. Correra, Physica C **314**, 247 (1999).

[20] J.G. Ossandon, J. R. Thompson, D. K. Christen, B. C. Sales, H. R. Kerchner, J. O. Thomson, Y. R. Sun, K. W. Lay and J. E. Tkaczyk, Phys. Rev. B **45**, 12534 (1992); J.G. Ossandon, J. R. Thompson, D. K. Christen, B. C. Sales, Yangren Sun, and K. W. Lay, Phys. Rev. B **46**, 3050 (1992).

[21] V.M. Vinokur, M. V. Feigel'man, and V. B. Geshkenbein, Phys. Rev. Lett. **67,** 915 (1991).

[22] B. Rosenstein and V. Zhuravlev, Phys. Rev. B **76,** 014507 (2007).

[23] K. Rompicharla, D. I. Novita, P. Chen, P. Boolchand, M. Micoulaut, and W. Huff, J. Phys. Cond. Matt. **20,** 202101 (2008).

[24] J.C. Phillips, Proc. Nat. Acad. Sci.(USA) **105**, 9917 (2008); Phys. Rev. B **75**, 214503 (2007).

[25] S. Chakravarty, D. G. Georgiev, P. Boolchand, and M. Micoulaut, J. Phys. Cond. Matt. **17,** L1 (2005).

Chapter 6

C-axis persistent current and Cooper-pair tunnelling through intrinsic Josephson junctions in a ring-shaped $YBa_2Cu_3O_{7-\delta}$ film

6.1 Introduction

The weak coupling between the CuO_2 planes of cuprate high-temperature superconductors (HTSCs) creates a natural tunneling barrier (intrinsic Josephson junction) for the charge carriers along the c-axis of these materials. The tunneling of quasiparticles and Cooper pairs through the c-axis intrinsic Josephson junctions have been studied in HTSC single crystals of $Bi_2Sr_2CaCu_2O_{8+x}$ (BSCCO) [1] and in $YBa_2Cu_3O_{7-\delta}$ (YBCO) [2, 3] thin films using the four-probe transport method. However, this technique cannot separate the Cooper-pair tunnelling contribution from that of the quasiparticle tunnelling to the observed critical current [4, 5]. In fact, previous attempts at fabricating junctions that enable one to only observe tunnelling of the Cooper pairs were not successful [6]. Moreover, this technique does not give a reliable estimation of the absolute value and the temperature dependence of the junction's critical current

I_{cj}. One of the problems is a non-zero voltage criterion that has to be applied to determine the value of I_{cj}, consequently leading to an overestimation of the magnitude of I_{cj}. The other problem is the Joule heating effects at the electrical contacts, which may contribute to an underestimation of I_{cj}. In order to circumvent the problems described above, we develop a method that enables the study of currents due to the Cooper-pair tunnelling *only*. The measurement of the junction's I_{cj} is contact-less, and is determined from the magnitude of the self-magnetic field of the persistent supercurrent flowing through the junction, detected by a magnetic sensor positioned some distance away.

In this study, we performed the first direct measurement of the temperature dependence of I_{cj} due to the Cooper pair tunnelling along the c-axis intrinsic Josephson junctions in $YBa_2Cu_3O_{7-\delta}$(YBCO). These measurements were performed on stacks of the c-axis intrinsic Josephson junctions incorporated into a ring-shaped thin film. The measured critical persistent current I_{cj} through these junctions decreases linearly with temperature. We observed this linear dependence of $I_{cj}(T)$ in different samples revealing the reproducibility of the fabrication and the results. The I-V tunneling experiments revealed the single c-axis stacks of c-axis intrinsic Josephson junctions has a gap ratio $2\Delta_c(0)/k_BT_c \simeq 2.22$.

6.2 Experimental details

6.2.1 Fabrication of Intrinsic Josephson Junctions integrated into ring-shaped thin film

In order to integrate the intrinsic Josephson junctions into the c-axis oriented YBCO ring-shaped thin film, we deposited two semi-ring-shaped YBCO films on (100) oriented $SrTiO_3$(STO) substrates, which overlap each other over an area of about 1 mm^2 (see Fig. 6.1). The junction area was made large enough to enable a detectable persistent current to flow through the ring. A three-step procedure and the rf-magnetron sputtering technique have been used to produce these junctions. The deposition has been carried out in an atmosphere of argon-oxygen mixture (20 mT of Ar and 100 mT of O_2) at a temperature of 750°C. At first a 145 nm thick STO step was deposited over half of the STO substrate area. Then a 145 nm thick YBCO film was grown on the STO substrate after masking the STO step. This film was then almost completely masked, except for regions of appropriate dimensions close to the STO step. The second 145 nm thick YBCO film was grown on the STO step and the un-masked region of the first YBCO film. The YBCO films overlap each other over a distance of 1 mm. After deposition the film was patterned in the form of a ring with inner and outer diameters of 2.8 mm and 4.8 mm, respectively. X-ray diffraction revealed a highly epitaxial YBCO film. Hence, there are two stacks of intrinsic Josephson junctions, located on opposite sides of the ring (see Fig. 6.1). Each stack has a thickness of 290 nm and thus contains about 248 intrinsic junctions. The T_c of the junctions is about 87 K.

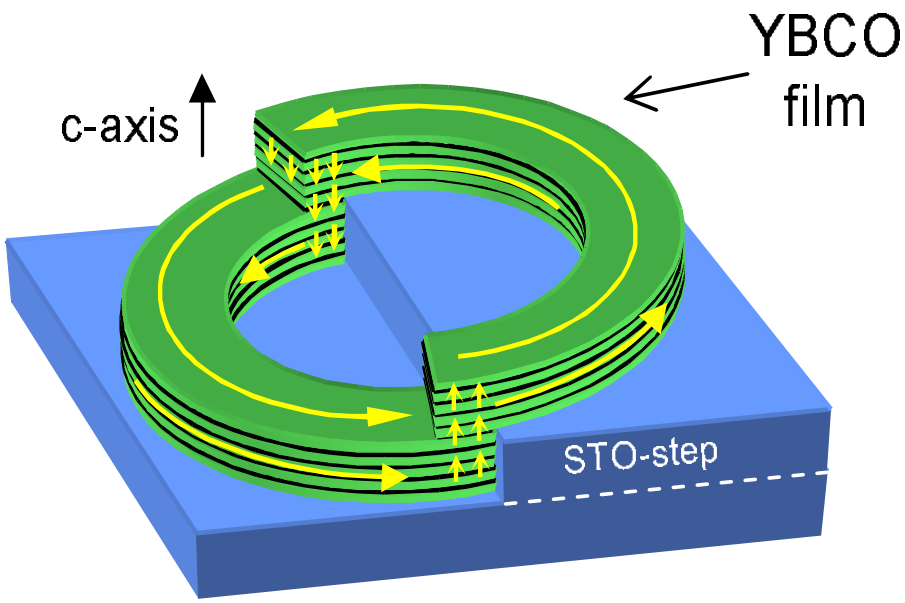

Figure 6.1: Schematic of the fabricated YBCO ring-shaped thin film integrated with two stacks of the c-axis intrinsic Josephson junctions (see text). The arrows show the flow of the circulating persistent current.

6.2.2 Measurements of the c-axis persistent current

A persistent circulating supercurrent was induced and measured in the ring using the following procedure: The ring was first cooled in a zero-field to the temperature of the measurement (below T_c). Then an external magnetic field was applied along the ring's axis and subsequently reduced to zero. The field trapped in the ring is a superposition of the magnetic field generated by the persistent current circulating around the ring and the field due to magnetic vortices trapped in the ring's bulk. At higher applied fields the trapped field saturates indicating that the critical value of the persistent current has been reached. The axial profile $B_z(r)$ of this magnetic field trapped in the ring (see Figure 6.2(a)) was measured across the ring with a

travelling Hall sensor positioned in air at room temperature at a distance of 2.5 mm above the sample surface (see Ref. [7, 8] for more details), over a temperature range from 10 K up to T_c. In order to separate the self-magnetic field due to the critical persistent current from that due to the trapped vortices in the ring's bulk, the ring was cut (hence preventing the flow of persistent current, see Fig. 6.3) and the measurements were repeated at the same value of the external applied magnetic field (see the bottom curve in Figure 6.2(a)). The difference of these trapped fields gives the self-field $B_z^p(r)$ of the pure critical persistent current (see Figure 6.2(b)). The obtained $B_z^p(r)$ is symmetric with respect to the ring's center and agrees very well with that obtained from a computer simulation, using the Biot-Savart's law, of the magnetic field generated by the current circulating in the ring, assuming a uniform current flow. The temperature dependence of the obtained magnetic field generated by the pure c-axis persistent current is shown in Figure 6.2(c). The value of the critical current was obtained from $B_z^p(r)$ using the Biot-Savart's law. This contact-less technique allows one to probe the properties of the c-axis intrinsic Josephson junctions (IJJ) in the presence of the Cooper-pair tunneling along the c-axis direction. The critical persistent current flowing in the ring is determined by the critical current I_{cj} of the stack of the IJJ.

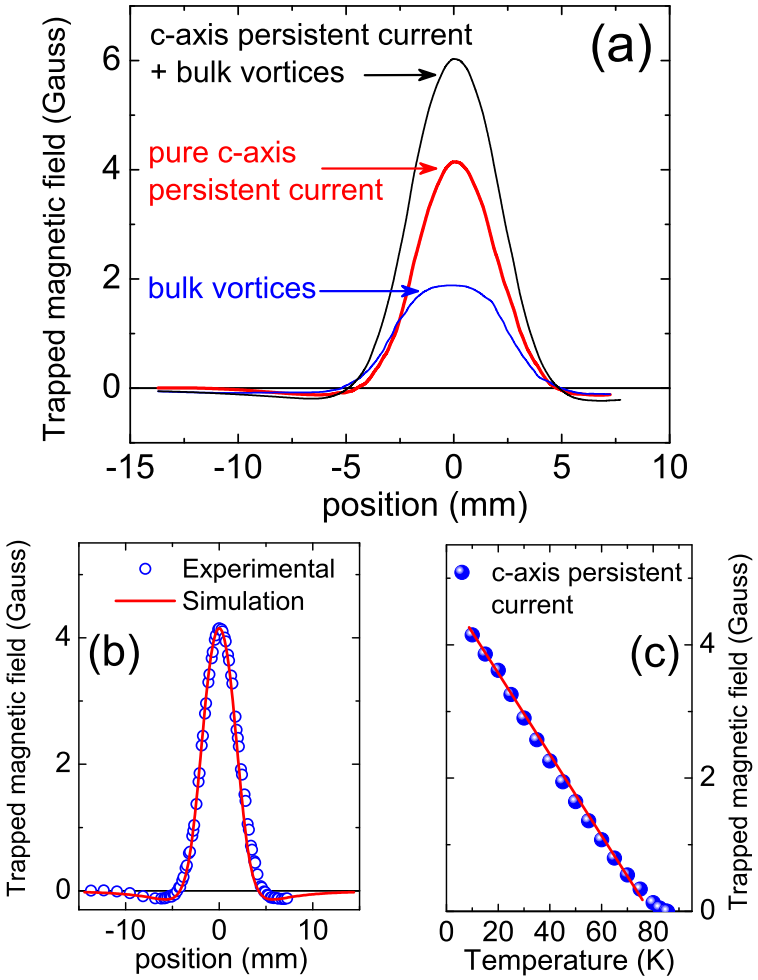

Figure 6.2: (a) The profile of the axial field B_z(r) (measured at 10 K) generated by the c-axis critical persistent current (middle curve), the bulk vortices (bottom curve) and the combined field of both (top curve). (b) The profile of the axial self-field B_z^p(r) induced by the c-axis critical persistent current. The solid line is the self-field of the circulating current calculated from the Biot-Savart law. (c) Temperature dependence of the self-field of the c-axis critical persistent current.

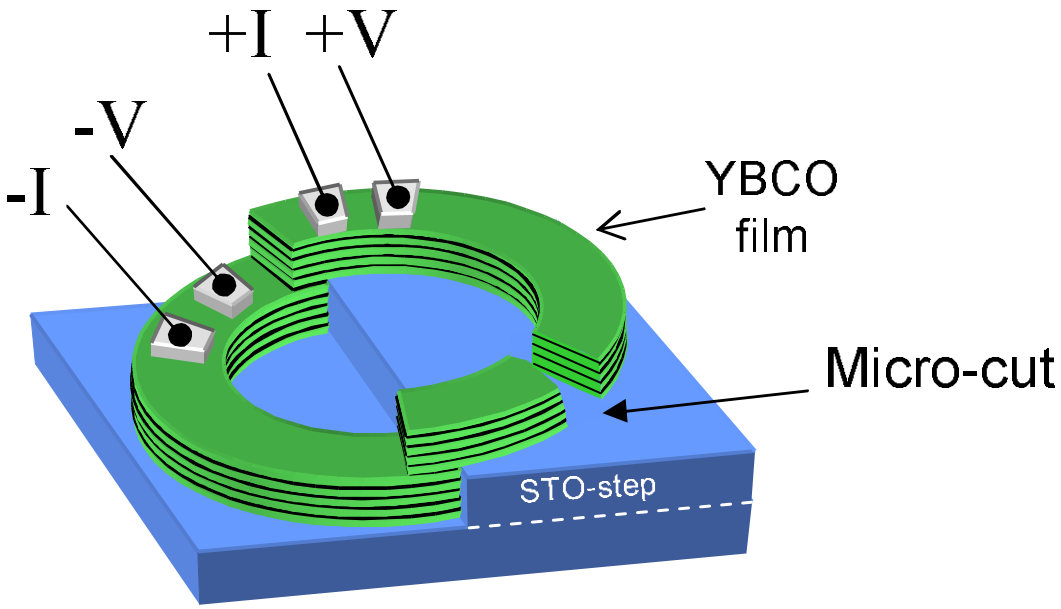

Figure 6.3: Schematic of the configuration of the electrical contacts made on the cut-ring for measuring the tunneling current. (The +I and +V contacts are switched for the resistivity measurements.)

6.3 Results and discussion

6.3.1 Temperature dependence of the *c*-axis persistent critical current

The temperature dependence of the c-axis critical current I_{cj} is shown in Figure 6.4. This dependence is linear over a wide range of temperatures, showing a clear deviation from the Ambegaokar-Baratoff [9] (AB) dependence (dashed curve in Figure 6.4) that has been observed in Josephson junctions of other superconductors, such as BSCCO [10], Sn and Pb [11]. The linear temperature dependence of critical currents is usually observed close to T_c in granular superconductors and is attributed to the percolating network of Josephson-coupled superconducting grains [9]. Similar linear dependence was also observed in films with the anti-phase boundaries [12] and correlated to the

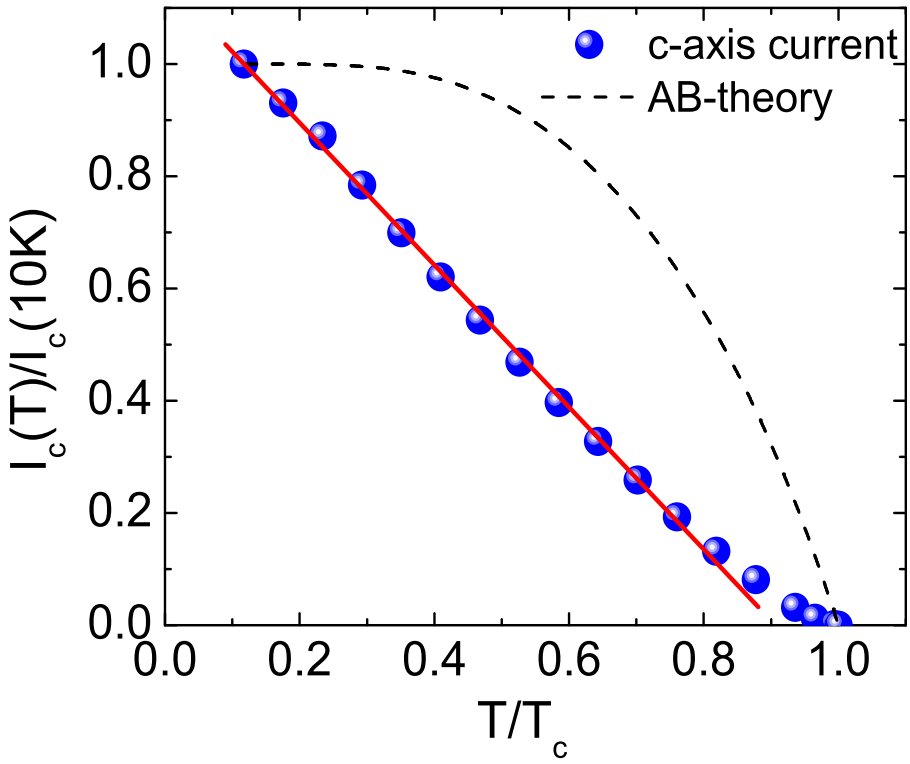

Figure 6.4: The temperature dependence of the c-axis critical current ($I_c(T)/I_c(10K)$) (solid spheres) showing a clear deviation from the Ambeagokar-Baratoff dependence (dashed curve).

pinning of the magnetic vortices. In one-dimensional films of tin [13] and indium [14] the linear dependence of $I_{cj}(T)$ on temperature was attributed to the pair breaking. The observation of the linear dependence of $I_{cj}(T)$ over a wide range of temperatures well below T_c in our ring-shaped sample could indicate the SNS-type [15] of the intrinsic Josephson junctions of YBCO. (The observed linear $I_{cj}(T)$ is also similar to the temperature dependence of narrow critical currents in narrow metallic bridges [16]

6.3.2 Characterization of the IJJs

After the ring was cut, the standard four-probe technique was used to characterize the IJJ's and the bulk film. The two stacks of IJJ's show similar behavior. Figure 6.5 shows the temperature dependence of the measured resistance of the bulk film and the junction. The temperature dependence of the junction resistance is found consistent with the c-axis resistance measurements reported by Rapp *et al.* [17]. The resistance of the junction is higher than that of the bulk film. The transition temperature of the junction resistance (86 K) is lower than that of the bulk (87.5K) (see the inset of Fig. 6.5(a)). The I-V_{bias} characteristics of the IJJ's show a gap structure at 0.4 V at a temperature of 84 K (see Figure 6.5(b)). The I_{bias}-V measurement gives I_{cj} $\sim$ 7 mA at this temperature. This is much larger than $I_{cj} \sim 2.3$ mA obtained from the self-field of the critical persistent current. This indicates that the quasiparticle current contributes to the magnitude of I_{cj} measured using the four-probe technique, in contrast to the (more accurate) persistent current method. In the former case the estimation of the critical current was based on the voltage criterion (about 1 μV) which led to an overestimation of the critical current. The measurements of the I-V_{bias} characteristics revealed the dependence of the gap voltage (V_g) of the IJJ on temperature (see the inset in Figure 6.5(b)). These values of V_g correspond to a superconducting gap of $N = 248$ junctions connected in series [18, 6]. An extrapolation of V_g(T) to a zero temperature gives $V_g(0) \sim 4.056$ V. Hence, the single junction gap $2\Delta_c/e = V_g/N \simeq 16.35$ mV and the c-axis gap ratio $2\Delta_c/k_BT_c \simeq 2.22$, where k_B is the Boltzmann constant and T_c is the transition temperature of the

IJJ. The small c-axis gap ratio, compared to the BCS result ($2\Delta_c/k_BT_c = 3.52$), is consistent with that obtained by other methods such as the infrared reflectivity [19].

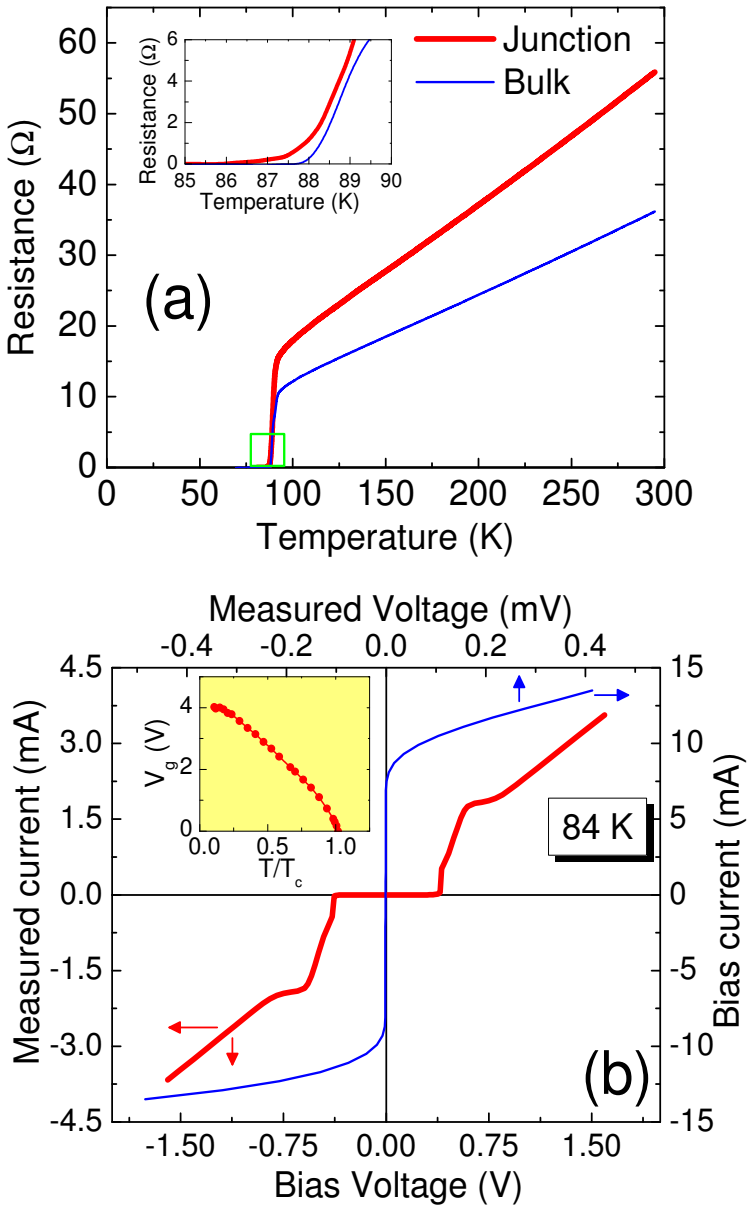

Figure 6.5: (a) The temperature dependence of the resistance of the IJJ and the bulk film. The inset shows the magnified region close to T_c. (b) I-V characteristics of the stack of the IJJ's at 84 K. The thick solid curve shows the dependence of the tunneling current on the bias voltage across the junction. The thin solid curve is the dependence of the voltage across the junctions as a function of the bias current. The insets show the temperature dependence of the gap voltage of the IJJ's.

6.4 Conclusion

We manufactured stacks of c-axis intrinsic Josephson junctions incorporated into a ring-shaped YBCO film. The contact-less and resistance-less technique allowed us to measure the c-axis critical persistent current due to the Cooper pair tunnelling through these junctions, which exhibits a linear dependence on temperature in clear contrast with the AB-dependence. We observed the linear dependence of I_{cj} on temperature in different samples which confirms the reproducibility of the fabrication and the results.

Bibliography

[1] G. Oya, N. Aoyama, A. Irie, S. Kishida, and H. Tokutaka, Jpn. J. Appl. Phys., Part 2 **31**, L829 (1992).

[2] H. Arie, K. Yasuda, H. Kobayashi, I. Iguchi, Y. Tanaka, and S. Kashiwaya, Phys. Rev. B **62**, 11864 (2000).

[3] A. S. Katz, A. G. Sun, S. I. Woods, and R. C. Dynes, Appl. Phys. Lett. **72**, 2032 (1998).

[4] J. J. Toppari, T. Kühn, A. P. Halvari, J. Kinnunen, M. Leskinen, and G. S. Paraoanu, Phys. Rev. B **76**, 172505 (2007).

[5] A. Odagawa, M. Sakai, H. Adachi, and K. Setsune, Jpn. J. App. Phys. **37**, 486 (1998).

[6] S. -J. Kim, Yu. I. Latyshev, T. Yamashita, and S. Kishida, Physica C **362**, 150 (2001).

[7] A. I. Mansour, M. Egilmez, I. Fan, K. H. Chow, J. Jung, E. M. Choi, H. S. Lee, S. I. Lee, and H. Darhmaoui, Appl. Phys. Lett. **90**, 162511 (2007).

[8] J. Jung, K. H. Chow, M. Egilmez, and A. Welsh, Appl. Phys. Lett. **87**, 262506 (2005).

[9] V. Ambegaokar and A. Baratoff, Phys. Rev. Lett. **10**, 486 (1963); V. Ambegaokar and A. Baratoff, Phys. Rev. Lett. **11**, 104 (1963).

[10] R. Kleiner, F. Steinmeyer, G. Kunkel, P. Müller, Phys. Rev. Lett. **68**, 2394 (1992).

[11] M. D. Fiske, Rev. Mod. Phys. **36**, 221 (1964).

[12] Ch. Jooss, R. Warthmann, H. Kronmller, T. Haage, H.-U. Habermeier, and J. Zegenhagen, Phys. Rev. Lett. **82**, 632 (1999).

[13] V. P. Andratskii, L. M. Grundel, V. N. Gubankov, and N. B. Pavlov, Zh. Eksp. Teor. Fiz. **65**, 1591 (1973) [Soy. Phys.-JETP **38**, 794 (1974)].

[14] L. G. Neumann and Y. H. Kao, J. Low Temp. Phys. **48**, 321 (1982).

[15] T. Kawae, M. Nagao, Y. Takano, H.B. Wang, T. Hatano, and T. Yamashita, Physica C **426**, 1479 (2005).

[16] M. Tinkham, *Introduction to Superconductivity* (McGraw-Hill, New York, 1996) 2nd edition.

[17] M. Rapp, A. Murk, R. Semerad, and W. Prusseit, Phys. Rev. Lett. **77**, 928 (1996).

[18] K. Tanabe, Y. Hidaka, S. Karimoto, and M. Suzuki, Phys. Rev. B **53**, 9348 (1996).

[19] R. T. Collins, Z. Schlesinger, F. Holtzberg, and C. Feild, Phys. Rev. Lett. **63**, 422 (1989).

Chapter 7

Temperature dependence of the persistent critical current of $YBa_2Cu_3O_{7-\delta}$ superconducting nanowires

7.1 Introduction

There has been an enormous, and still growing, research interest [1, 2, 3, 4, 5, 6, 7, 8, **?**, 10, 11] in superconducting nanowires motivated by their crucial role in superconducting nanoelectronic devices such as single-photon detectors [2, 3] and high-speed digital circuit testing [12]. The superconducting nanowires in these systems behave in a similar fashion as Josephson junctions, where the main quantity of interest is the tunnelling critical supercurrent (J_c) and its temperature dependence. Despite the fact that high temperature superconductors (HTSC's) such as YBCO can operate above liquid nitrogen temperature (77 K), nanowires of low temperature superconductors are more studied and involved in applications than their HTSC's counterparts. This is due to the difficulty in synthesizing and characterizing the transport properties of high quality nanowires of HTSC's, as well as to the absence of theoretical predictions

of their $J_c(T)$.

The characterization of superconducting nanowires is traditionally based on the four-probe technique, i.e., on the measurements of the I-V curves or on the temperature dependence of the resistance [1, 4, 5, 6, 7, 8, **?**, 10, 11, 13]. In spite of the valuable information offered by this technique, it does not provide enough insight about the transport properties in the pure superconducting state of the nanowires. In particular, by using the four-probe technique, it is not possible to measure the temperature dependence of the persistent critical supercurrent ($J_c(T)$) of superconducting nanowires, especially HTSC's, nor is it possible to directly observe the effect of the nanowire's length on its persistent supercurrent. The main goal of the current study is address these issues by first synthesizing YBCO nanowires suitable for transport characterization, and then using an unconventional (contactless) technique to characterize their persistent critical currents. This technique is based on measuring the self-magnetic field of the persistent current in ring-shaped superconducting films. This contactless technique [17] is superior to the four-probe transport method that suffers from the non-zero voltage criterion and Joule heating effects. Moreover, the latter technique was proven unable to separate the Cooper-pair tunnelling contribution from that of the quasiparticle tunnelling in the observed critical current [17, 18, 19]. Thus we first incorporate YBCO nanowires into YBCO rings, where we take advantage of the fact that YBCO nanowires form through pinholes [14] of an STO-layer [15] in YBCO/STO/YBCO systems, thus connecting the top and bottom YBCO films as confirmed by transmission electron microscopy (TEM) measurements

[16]. Then, we use the contactless technique to investigate the persistent critical current of the YBCO nanowires, and explore the effects of the nanowires' length on their transport properties.

In this study, we investigate the persistent critical current (J_c) tunnelling through YBCO nanowires integrated into ring shaped YBCO thin films. These measurements were performed on four samples of YBCO nanowires with nominal lengths 20, 30, 40, and 64 nm. Our observations reveal that J_c has two different temperature dependences; a GL-dependence at low temperatures which is found the same in all the studied nanowires' lengths, and a different power law temperature dependence at high temperatures which is found dependent on the length of the nanowires. The crossover between these two dependences is attributed to an onset of vortex dissipative motion across the nanowires leading to J_c suppression.

7.2 Experimental details

7.2.1 Fabrication of the YBCO nanowires embedded in an STO-layer integrated between two semi-ring-shaped YBCO thin films

The experiments were performed on YBCO nanowires integrated into *c*-axis oriented YBCO ring-shaped thin films (see Fig. 7.1(a)) with different nanowire lengths. Each sample consists of two semi-ring-shaped YBCO films deposited on (100) oriented STO substrates, with an STO-layer sandwiched in the overlapping area (~ 1 mm^2) between the two YBCO films. The junction area was made large enough to enable the formation of a large number of nanowires [16] allowing a detectable persistent current to flow through the ring. A four-step procedure and the rf-magnetron sputtering technique was used to produce each sample. The deposition was carried out in an atmosphere of argon-oxygen mixture (20 mT of Ar and 100 mT of O_2) at a temperature of 750°C. First, a 145 nm thick STO-step was deposited over half of the STO substrate area. Then, a 145 nm thick YBCO film was grown on the second half of the STO substrate while masking the STO-step. This first YBCO film was then almost completely masked, except for regions of appropriate dimensions close to the STO-step. Then an STO-layer of thickness L was deposited on both the exposed area of the first YBCO film and the whole area of the STO-step. Finally, a second 145 nm thick YBCO film was grown on the STO-layer. (Note that a small area of the deposited STO-layer was masked before depositing the second YBCO film in order to avoid direct contact between the two YBCO films, see Fig. 7.1(a).) After deposi-

tion, the film was patterned in the form of a ring with inner and outer diameters of 2.8 mm and 4.8 mm, respectively. X-ray diffraction revealed highly epitaxial YBCO films. Scanning electron microscope (SEM) measurements of the exposed area of the STO-layer (see Fig. 7.1(b)) of all samples revealed the presence of pinholes through which nanowires (nanobridges) can grow, thus connecting the top and bottom YBCO layers as confirmed by previous TEM measurements [16]. Four samples were grown with nominal nanowires lengths (concluded from the thickness of the STO-layer) of 20, 30, 40, and 64 nm. The T_c was determined from the condition that J_c=0 (no persistent current) of the four samples and found to be 86 ± 1 K.

7.2.2 Measurements of the persistent current of the YBCO nanowires

A persistent circulating supercurrent was induced and measured in the ring using the following procedure: The ring was first cooled in a zero-field to the temperature of the measurement (below T_c). Then an external magnetic field was applied along the ring's axis and subsequently reduced to zero. The field trapped in the ring is a superposition of the magnetic field generated by the persistent current circulating around the ring and the field due to magnetic vortices trapped in the ring's bulk. At higher applied fields, the trapped field saturates indicating that the critical value of the persistent current has been reached. The axial profile B_z(r) of this magnetic field trapped in the ring was measured across the ring with a traveling Hall sensor positioned in air at room temperature at a distance of 2.5 mm above the sample surface [25], over a

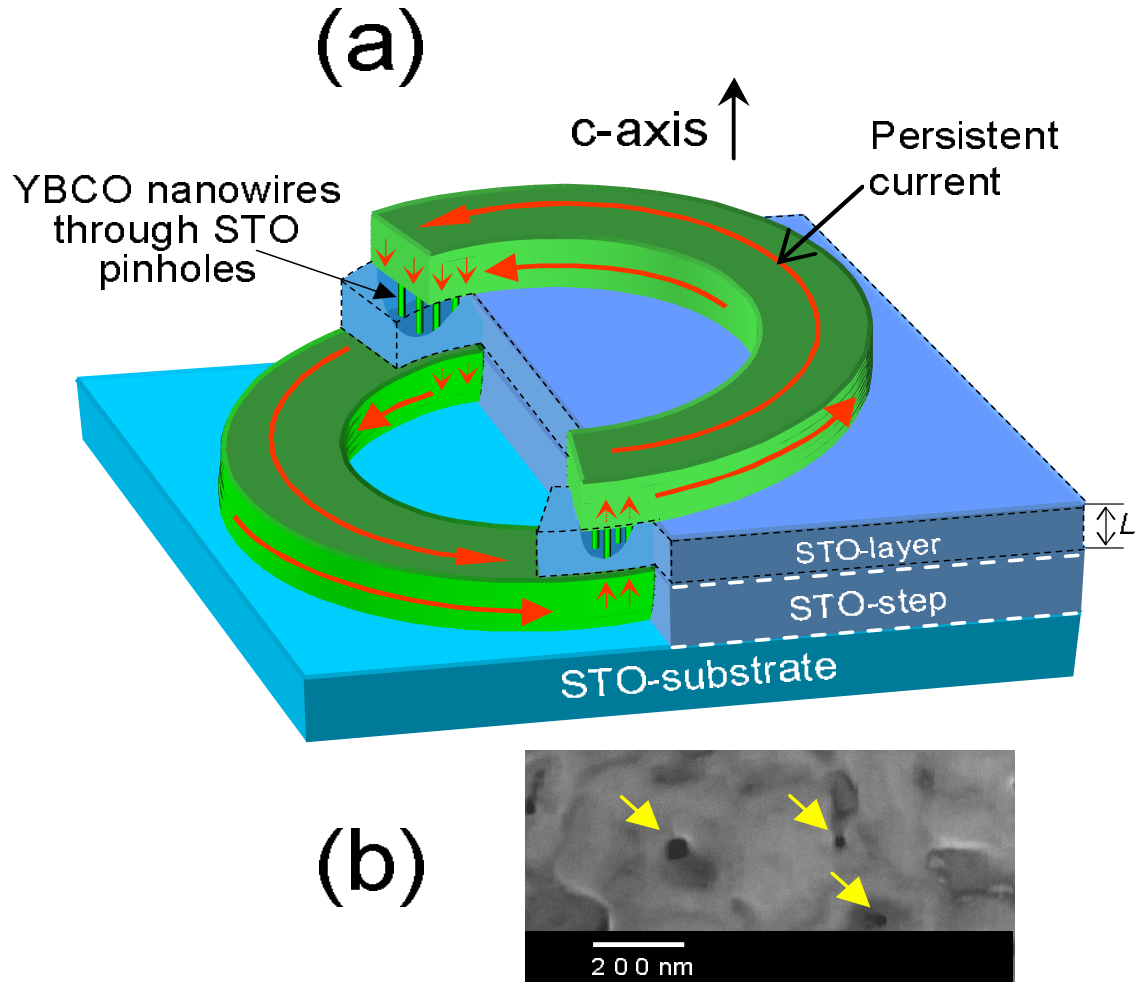

Figure 7.1: (a) Schematic of the fabricated YBCO nanowires integrated into ring-shaped YBCO thin film. The STO-layer of thickness L separating the top and bottom YBCO films is shown with dashed circumference. (b) SEM micrograph showing pinholes (see the arrows) in the STO-layer through which YBCO nanowires grow.

temperature range from 10 K up to T_c. In order to separate the self-magnetic field due to the critical persistent current from that due to the trapped vortices in the ring's bulk, the ring was cut (hence preventing the flow of persistent current) and the measurements were repeated at the same value of the external applied magnetic field. (Detailed explanation of this step can be found in Chapter 5.) The difference of these trapped fields gives the self-field $B_z^p(\mathrm{r})$ of the pure critical persistent current. The value of the critical current was obtained from $B_z^p(\mathrm{r})$ using the Biot-Savart's law. The persistent current flowing in the ring is determined by the critical supercurrent tunnelling through the nanowires, hence the measured persistent critical current is that of the nanowires.

7.3 Results and discussion

7.3.1 Temperature dependence of the c-axis persistent critical current of the YBCO nanowires with varying lengths

The temperature dependence of $[J_c(T)/J_c(10K)]^{2/3}$ of the persistent critical current density (J_c) of the nanowires is shown in Fig. 7.2. The four samples show the same Ginzburg-Landau like (GL) temperature dependence [20] of J_c over a wide range of low temperatures. In general, $J_c(T)$ is in clear deviation from the Ambegaokar-Baratoff (AB) dependence [21] that has been observed in underdoped intrinsic Josephson junctions of YBCO [22], and in other superconductors like BSCCO [23], Sn and Pb [24]. The GL temperature dependence ($J_c(T) \propto (T_c - T)^{3/2}$) at low temperatures indicates that the current is flowing in filamentary pathways [25, 26] which is consistent with the filamentary nature of the superconducting nanowires. The 3/2 power de-

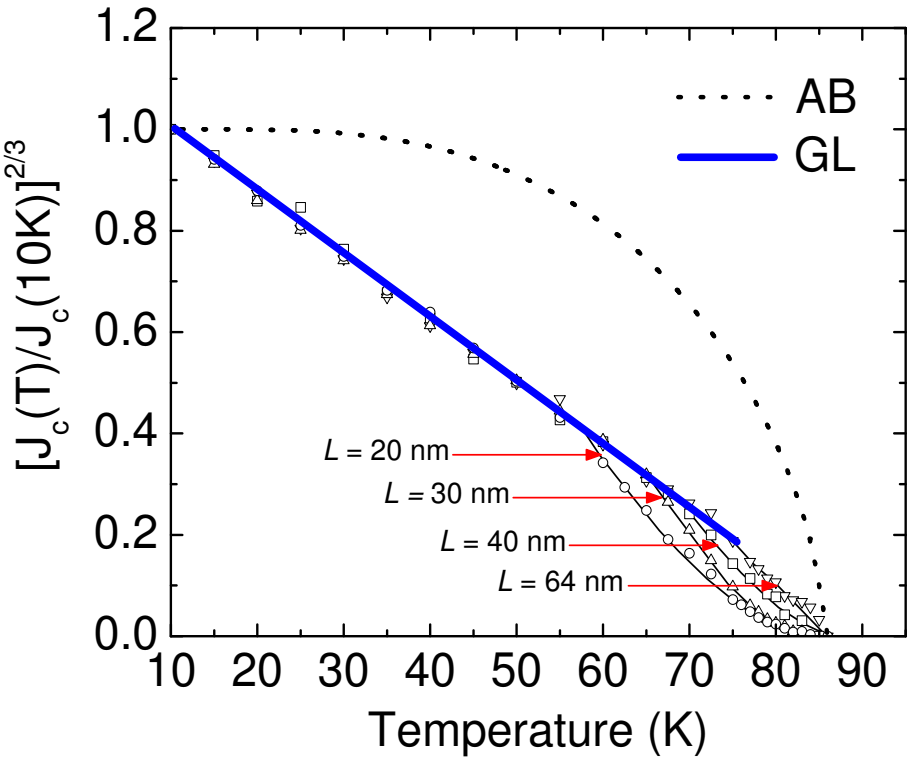

Figure 7.2: Temperature dependence of the persistent current $[J_c(T)/J_c(10K)]^{2/3}$, with nanowires lengths 20 nm, 30 nm, 40 nm, and 64 nm, showing a clear deviation from the Ambeagokar-Baratoff (AB) dependence (dotted curve). For all nanowires lengths, the low temperature part of J_c follows Ginzburg-Landau (GL) dependence (thick solid straight line). (The thin solid curves are guides to the eyes, the fittings are shown in Fig. 7.3.)

pendence (GL-dependence) also indicates that the suppressed superconducting order parameter smoothly retains its bulk (maximum) value at the ends of the nanowires [27, 28, 29]. At high temperatures, $J_c(T)$ deviates from the GL-dependence where each sample follows a particular power law dependence ($J_c(T) \propto (T_c - T)^{\alpha}$, with $\alpha > 3/2$) depending on the length of the nanowires.

7.3.2 Effect of vortex depinning and dissipative motion on the temperature dependence of the persistent current of the nanowires

In Figures 7.3(a-d), we show the temperature dependence of the persistent critical current $[J_c(T)/J_c(10K)]^{2/3}$ of the four samples with varying nanowire lengths. The best fits of $J_c(T)/J_c(10K)$ to the empirical relation $(T_c - T)^{\alpha}$ at high temperatures are shown as red (thin) curves, and the GL dependence at low temperatures is shown as straight blue (thick) line, where the cross-over temperature (T^*) between these two temperature dependences is indicated. In each sample, the changes in $J_c(T)$ dependence at T^* can be related to the dissipative vortex motion due to depinning of vortices/flux-lines that are trying to escape from the ring's center through the junction areas (weakest spots in the ring). It is known that when a vortex crosses a supercurrent pathway in the transverse direction, it induces electric field components parallel to the direction of the supercurrent flow. This, in turn, results in ohmic losses leading to the suppression of the flowing supercurrent. The dissipative motion of the vortices seems to start up at higher temperatures (higher T^*) in longer nanowires. This could be due to the weaker coupling in long nanowires that can provide strong vortex pinning centers compared to shorter nanowires characterized with stronger coupling, i.e., weaker pinning centers. Thus one expects the vortex depinning process to set up at higher temperatures in longer nanowires as we observed. The difference in the coupling strength between short and long nanowires is consistent with the observed decrease of α from 2.7 to 1.65. This decrease in α indicates that the behavior of the nanowires at high temperatures changes from SNS-like junctions (strong cou-

pling) to SIS-like junctions [30, 31, 32] (weak coupling) as the length of the nanowire increases.

It is worth mentioning that measurements of the persistent critical current in samples without an STO-layer, i.e., in YBCO intrinsic Josephson junctions without nanowires, revealed a linear temperature dependence of J_c without any indications of suppressions (see Fig. 3 of Ref.[17]).

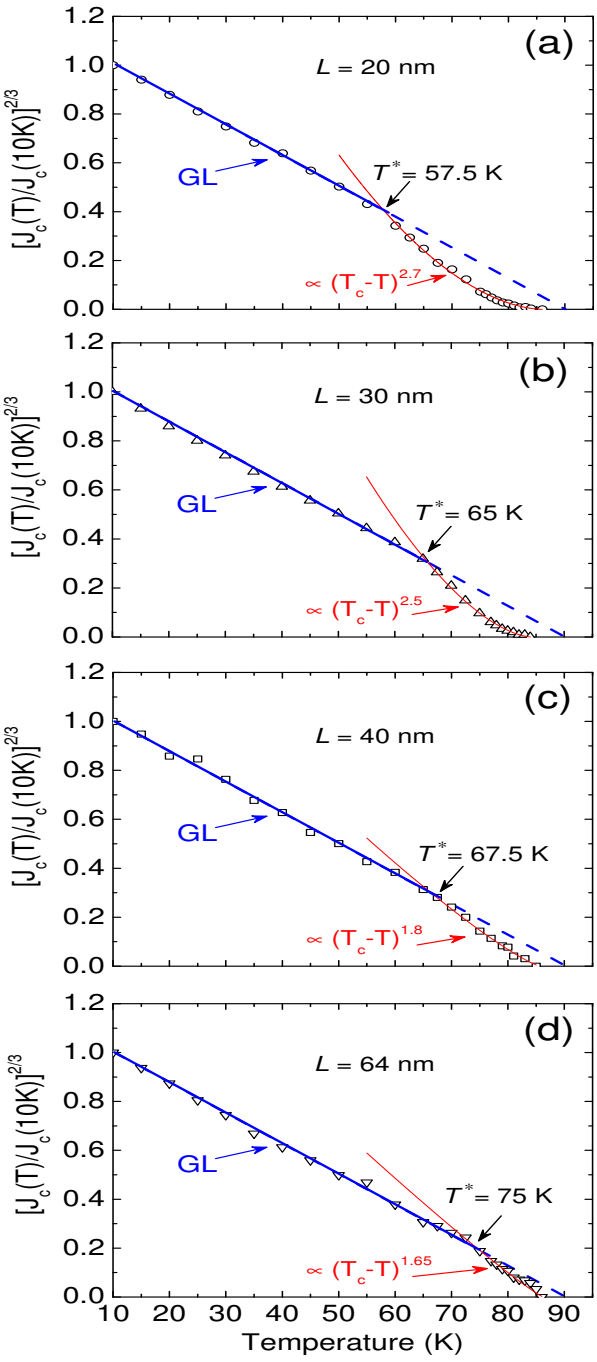

Figure 7.3: Temperature dependence of the persistent current $[J_c(T)/J_c(10K)]^{2/3}$, with nanowires lengths L (a) 20 nm, (b) 30 nm, (c) 40 nm, and (d) 64 nm. The best fit of the region close to T_c to the power law dependence $(T_c - T)^{\alpha}$ is shown as thin red curves. The cross-over temperatures T^*, below which the temperature dependence of J_c is purely GL, are also indicated for each case.

7.4 Conclusion

We integrated superconducting YBCO nanowires into ring-shaped YBCO thin films and varied the lengths of the nanowires. This enabled us to study the temperature dependence of the persistent critical current J_c of the nanowires. Two different temperature dependences of J_c are manifested: a GL-dependence ($J_c(T) \propto (T_c - T)^{3/2}$) at low temperatures which is common between all the studied samples, and another power law dependence ($J_c(T) \propto (T_c - T)^{\alpha>3/2}$) at high temperatures which depends on the length of the nanowire. We attribute the crossover between these two dependences to an onset of a vortex dissipative motion that limits the supercurrent flow in the nanowires.

Bibliography

[1] J. E. Mooij and Yu. V. Nazarov, Nature Phys. **2**, 169 (2006); M. Zgirski *et al.*, Nano Lett. **5**, 1029 (2005).

[2] J. Zhang, W. Slysz, A. Verevkin, O. Okunev, G. Chulkova, A. Korneev, A. Lipatov, G. N. Goltsman, and Roman Sobolewski, IEEE Trans. Appl. Supercond. **13**, 180 (2003).

[3] A. J. Kerman, Eric A. Dauler, William E. Keicher, Joel K. W. Yang, Karl K. Berggren, G. Goltsman, and B. Voronov, Appl. Phys. Lett. **88**, 111116 (2006).

[4] J.S. Langer and V. Ambegaokar, Phys. Rev. **164**, 498 (1967).

[5] A.G. Sivakov *et al.*, Phys. Rev. Lett. **91**, 267001 (2003).

[6] F.-R. Ladan *et al.*, J. Low Temp. Phys. **153**, 103 (2008).

[7] S. Reymond *et al.*, Phys. Rev. B **66**, 014522 (2002) and references therein.

[8] F.S. Jelila *et al.*, Phys. Rev. Lett. **81**, 1933 (1998).

[9] R.B. Laibowitz *et al.*, Appl. Phys. Lett. **35**, 891 (1979).

[10] B.I. Ivlev and N.B. Kopnin, Adv. Phys. **33**, 114 (1984).

[11] A. Bezryadin *et al.*, Nature **404**, 971 (2000).

[12] A. Korneev *et al.*, Microelectron. Eng. **69**, 274 (2003).

[13] M. Tinkham, *Introduction to Superconductivity* (McGraw-Hill, New York, 1996) 2nd edition.

[14] G. Zhang *et al.*, Nanotechnology **17**, 4252 (2006).

[15] Y. L. Cheung, I. P. Jones, J. S. Abell, T. WButton, and E. F. Maher, Supercond. Sci. Technol. **20**, 216 (2007).

[16] E. Olsson and K. Char, Interface Science **1,** 371 (1993).

[17] A. I. Mansour, M. Saber, K. H. Chow, and J. Jung, Appl. Phys. Lett. **93**, 142509 (2008).

[18] J. J. Toppari, T. K¨hn, A. P. Halvari, J. Kinnunen, M. Leskinen, and G. S. Paraoanu, Phys. Rev. B **76**, 172505 (2007).

[19] A. Odagawa, M. Sakaih, H. Adachai, and K. Setsune, Jpn. J. App. Phys. **37**, 486 (1998).

[20] J. R. Clem, B. Bumble, S. I. Raider, W. J. Gallagher, and Y. C. Shih, Phys. Rev. B **35**, 6637 (1987).

[21] V. Ambegaokar and A. Baratoff, Phys. Rev. Lett. **10**, 486 (1963); Phys. Rev. Lett. **11**, 104 (1963).

[22] T. Kawae, M. Nagao, Y. Takano, H.B. Wang, T. Hatano, and T. Yamashita, Physica C **426**, 1479 (2005).

[23] R. Kleiner, F. Steinmeyer. G. Kunkel, and P. Müller, Phys. Rev. Lett. **68**, 2394 (1992).

[24] M. D. Fiske, Rev. Mod. Phys. **36**, 221 (1964).

[25] H. Darhmaoui, J. Jung, J. Talvacchio, M. A-K. Mohamed, and L. Friedrich, Phys. Rev. B **53**, 12330 (1996); A. I. Mansour, M. Egilmez, I. Fan, K. H. Chow, J. Jung, E. M. Choi, H. S. Lee, S. I. Lee, and H. Darhmaoui, Appl. Phys. Lett. **90**, 162511 (2007); A. I. Mansour, Rongchao Ma, M. Egilmez, M. Elsayed, I. Fan, K. H. Chow, and J. Jung, Phys. Rev. B **79**, 172504 (2009).

[26] J.C. Phillips and J. Jung, Phil. Mag. B **81,** 745 (2001); Phil. Mag. B **82,** 1163 (2002); J. Jung, K. H. Chow, M. Egilmez, and A. Welsh, Appl. Phys. Lett. **87,** 262506 (2005); H. Darhmaoui and J Jung, Phys. Rev. B **53**, 14621 (1996).

[27] A. Baratoff, J. A. Blackburn, and B. B. Schwartz, Phys. Rev. Lett. **25**, 1096 (1970).

[28] M. T. Jahn and Y. H. Kao, J. Low Temp. Phys. **13**, 175 (1973).

[29] Y.-du Song and G. I. Rochlin, Phys. Rev. Lett. **29**, 416 (1972).

[30] T. R. Finlayson, D.A. Garvie, D.B. Lowe, Z. Przelozny and T.E Smith, Cryogenics **30**, 467 (1990).

[31] P. Pereyra, Josè L. Cardoso, Luis E. Amezcua, and A. Kunold, Physica C **266**, 81 (1996).

[32] J. L. Cardoso and P. Pereyra, Phys. Rev. B **61**, 6360 (2000)

Chapter 8

Summary of Contributions

In this thesis, we investigated the intrinsic disorder effects and the intrinsic transport and magnetic properties of thin films and tunnel junctions of the high temperature superconductor $YBa_2Cu_3O_{7-\delta}$ (YBCO). We used a special contactless technique that allowed us to measure the temperature and time dependences of the critical persistent current of superconducting rings. Our technique is superior to the four-probe transport method which suffers from the non-zero voltage criterion and Joule heating effects. Moreover, the latter technique was also proven unable to separate the Cooper-pair tunnelling contribution from that of the quasiparticle tunnelling to the observed critical current in superconducting tunnel junctions (STJs).

Different forms of epitaxial *c*-axis oriented YBCO ring-shaped thin films were made, depending on whether the *ab*-plane or *c*-axis persistent critical current is the property to be investigated. An intrinsic type of disorder, namely oxygen vacancies, was gently and slowly introduced into the YBCO rings. This allowed us to study the correlation between the hole doping level, the persistent current flow, and the vortex structure in the *ab*-plane of YBCO rings. Also, we developed a special form

of superconducting rings which enabled us to study the intrinsic behavior of the c-axis persistent critical current of YBCO. More specifically, we integrated stacks of intrinsic Josephson junctions into ring-shaped YBCO thin films, and this allowed us to study the temperature dependence of the persistent current that is due to Cooper-pairs' tunneling along the c-axis of YBCO. Then we studied the c-axis persistent critical current of YBCO nanowires and the effect of nanowires length on their superconducting properties. The nanowires were embedded in insulating thin layers of $SrTiO_3$ (STO) sandwiched artificial barriers between two semi-ring-shaped YBCO films. Previous transmission electron microscopy (TEM) studies [E. Olsson and K. Char, Interface Science **1,** 371 (1993)] confirmed the formation of YBCO nanowires through pinholes in the sandwiched STO-layer of the YBCO/STO/YBCO system. Thus we were able to form YBCO superconducting nanowires connecting the two YBCO films through pinholes in the STO-barrier. This allowed us to observe the effect of vortex depinning and dissipative motion on the temperature dependence of the persistent critical current in YBCO nanowires.

The rest of this chapter summarizes the experimental observations discussed in this thesis, and provides some insight regarding potential extensions of the present work.

8.1 Oxygen-vacancy effects on the persistent current flow and on the vortex structure of YBCO

A detailed analysis of the temperature dependence of the persistent critical current was made, where we detected an anomalous behavior of the persistent current flow

within a certain concentration range of oxygen vacancies in YBCO. The anomaly in the persistent current flow was found to be directly related to the appearance of a spinodal decomposition in the oxygen content of YBCO. This spinodal phase represents a competition between two coexisting phases, oxygen rich and oxygen deficient, as the concentration of oxygen vacancies was increased. We explained the mechanism of this competition as an oxygen redistribution inside the sample, where an internal flow of oxygen atoms from the oxygen rich domains (superconducting grains) to the oxygen deficient domains (grain boundaries) takes place. In fact, this is the first observation that reveals the sensitivity of the persistent current to the oxygen content and distribution in YBCO, and constitutes the first evidence of the ability of the transport current to detect the occurrence of spinodal decomposition in the oxygen content of YBCO.

The detailed analysis of the time dependence of the persistent critical current, using Maley's scheme, allowed us to monitor the evolution of the vortex structure of $YBa_2Cu_3O_{7-\delta}$ as the concentration of oxygen vacancies was increased. We found that the vortex structure strongly correlates with the changes in the hole doping level in the CuO_2 planes. In fact, as δ increases, the collective lattice self-organization of the as-grown sample decreases, leading to the formation of vortex-glass and vortex-pinned-liquid phases. These vortex phases form in regions between step-like changes in the dependence of the hole doping on disorder.

By conducting this study, we answer a 15-year old request that was raised in 1994 when Blatter *et al.* [Rev. Mod. Phys. **66,** 1125 (1994)] said that "a systematic

experimental study of the correlation between oxygen defect concentration and the critical current density [in single crystals] would be highly desirable." We believe that our fundamental results will stimulate further development and renewed interest in theories of the vortex structure and its response to intrinsic lattice disorder and/or a hole doping level in high temperature superconductors.

8.2 Transport properties of YBCO intrinsic Josephson junctions and superconducting nanowires

In order to explore the intrinsic properties of the c-axis persistent critical current, we manufactured stacks of c-axis intrinsic Josephson junctions incorporated into ring-shaped YBCO films. The contact-less and resistance-less technique that we used allowed us to measure the c-axis persistent critical current I_{cj} that is due to the Cooper pair tunnelling through these junctions, and which exhibited a linear dependence ($I_{cj} \propto (T_c - T)$) on temperature, clearly deviating from the AB-dependence. We observed the linear dependence of I_{cj} on temperature in different samples which confirms the reproducibility of the fabrication and the results. This study reports the first direct measurement of the persistent critical current that is due to tunnelling Cooper-pairs only, i.e., excluding any contribution from the quasiparticles' tunnelling.

Having established that, we then explored the Cooper-pairs' tunnelling mechanism through YBCO nanowires. For this purpose, we integrated $YBa_2Cu_3O_{7-\delta}/SrTiO_3/YBa_2Cu_3O_{7-}$ superconductor tunnel junctions into ring-shaped YBCO thin films, where the thickness of the STO-layer was varied systematically. In this way we were able to form YBCO nanowires connecting the top and bottom YBCO layers through pinholes in

the STO-layer. Thus by changing the thickness of the STO-layer we changed the length of the nanowires. Our studies of the temperature dependence of the c-axis persistent critical current J_c across the YBCO nanowires revealed that J_c has two different temperature dependences: a GL-dependence ($J_c \propto (T_c - T)^{3/2}$) at low temperatures which we found the same in all studied samples, and another power law dependence ($J_c \propto (T_c - T)^{\alpha > 3/2}$) at high temperatures which turned out to depend on the length of the nanowires. We attributed the cross-over between these two temperature dependences to vortex depinning and the resulting dissipative motion.

8.3 Extension of Current Studies

The extensive studies reported in this thesis are not limited to YBCO, but rather they can be applied to any type of superconductor and its heterostructures. For instance, the study of the effect of oxygen vacancies on the flow of the persistent current and the structure of the vortex mater can be conducted in Bi- and Tl-based cuprate superconductors. These superconducting systems are more anisotropic than YBCO and, therefore, might exhibit interesting transformations in the vortex matter.

The method that we developed in this thesis concerning the fabrication and measurement of the c-axis persistent current which is purely due to tunnelling Cooper-pairs, can also be extended to all other types of superconductors. Of particular interest, are the non-cuprate high temperature superconductors such as MgB_2 and the newly discovered Fe-based superconductors. Moreover, one can investigate the rich physics that arises from forming interfaces between different condensed mat-

ter systems by incorporating superconducting tunnel junctions into ring-shaped thin films. For example, one can explore the supercondutor/manganite/superconductor junctions, where the metal-insulator transition temperature of the manganite layer falls within the superconducting state of superconducting electrodes.

In conclusion, this thesis establishes experimental approaches and new techniques, thus opening endless avenues yet to be explored in the field of superconductivity and its heterostructures.

Appendix A

Temperature dependence of the persistent critical current and instabilities in MgB_2 thin films

A.1 Introduction

Thin films of the superconductor MgB_2 have critical temperatures (T_c) as high as 39 K and critical current density J_c as high as $4 \times 10^7 A/cm^2$ at 5 K [1]. Such materials are good candidates for applications such as superconducting thin film devices including superconducting quantum interference devices [2]. One way to understand the superconducting transport properties of MgB_2 films is to measure the temperature dependence of the critical current.

The properties of particular interest are the effects of microstructure on the flow of the current and on the magnetic vortex pinning. An important feature of MgB_2 films at low temperatures is an abrupt suppression (instability) of the supercurrent below 10 - 11 K [3]. Such behavior is believed to arise from a highly non-uniform dendritic-like flow of magnetic vortices in the sample that leads to energy dissipation and supercurrent suppression in the film [4, 5]. Magneto optical imaging (MOI) studies

have enabled the dendritic flow (avalanche) of vortices at temperatures below 11 K in MgB_2 films (see Fig. A.1) to be observed *in-situ* [5]. This vortex avalanche appears to be an intrinsic property of the films [3], and will certainly affect their applications at low temperatures. A related issue is the role of Mg deficiency on T_c and J_c in MgB_2 films. In particular, it is known that T_c is reduced in magnesium-deficient MgB_2 films [6]. However, the effect of the magnesium deficiency on the dendritic flow instability at low temperature is not known.

Hence, previous studies performed on MgB_2 films raise a number of questions which are relevant for technological applications. What is the detailed temperature dependence of the critical current $J_c(T)$ and how is it affected by the motion of magnetic vortices? What is the effect of a reduction in T_c on $J_c(T)$ and the low temperature vortex flow instability? In order to answer these questions we investigated $J_c(T)$ and the time decay of the supercurrent $J(t)$ from its critical value for MgB_2 films with various transition temperatures.

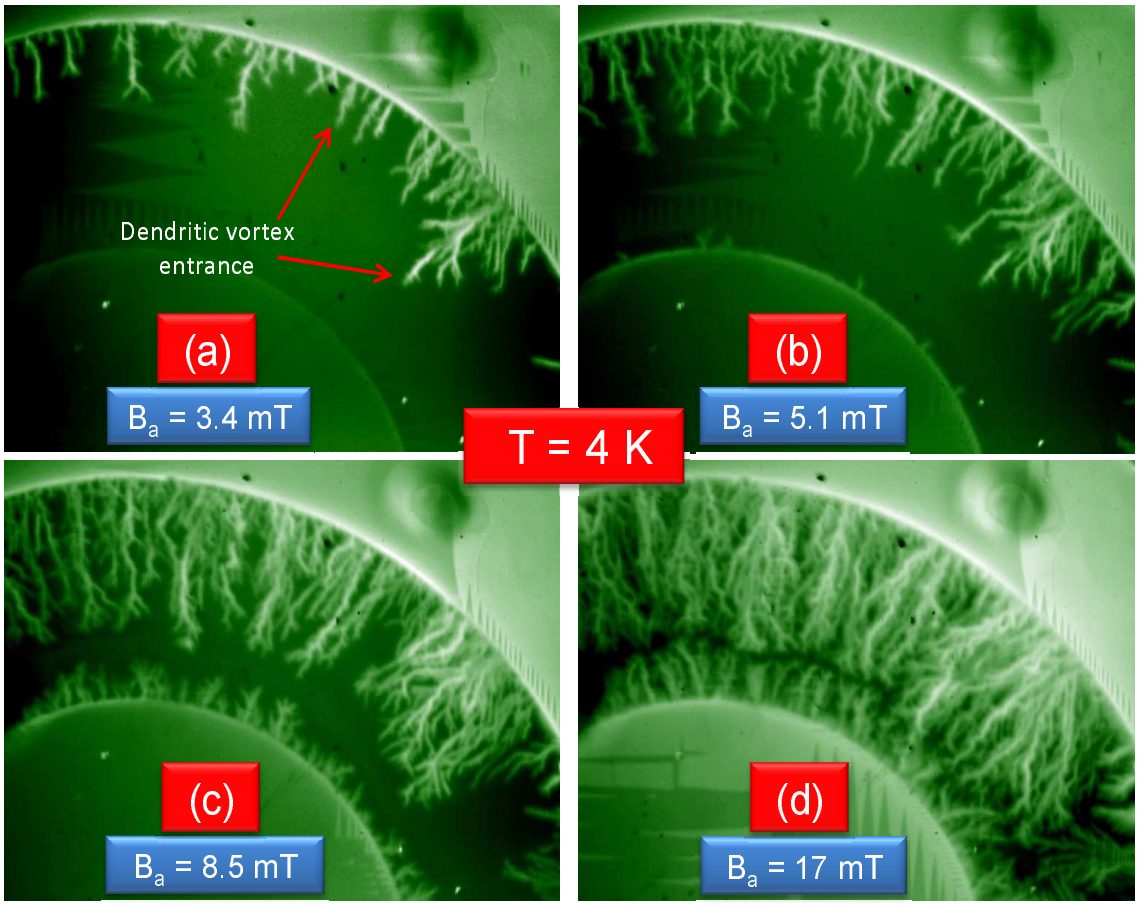

Figure A.1: Magneto Optical Images of a part of MgB_2 ring-shaped film zero-field-cooled to a temperature of 4 K. The applied magnetic field B_a was increased from 3.4 to 17 mT (170 Gauss) as is shown. The magnetic flux distribution is revealed as bright areas, where the dendritic vortex entrance is indicated.

A.2 Experimental details

A.2.1 Fabrication of the MgB_2 films and measurements of the temperature dependence of the persistent current

Most of the measurements in this paper were carried out on ring-shaped films (of inner diameters ranging from 1 to 4 mm). Persistent circulating supercurrents were induced in the ring by first zero-field cooling it to the temperature of interest (below T_c), then applying an external magnetic field along the ring's axis and subsequently reducing it to a zero. The axial profile of the magnetic self-field $B_z(r)$ of the persistent current was then measured across the ring with a travelling Hall sensor. The Hall sensor was positioned in air at room temperature at a distance of 2.5 mm above the sample surface. The magnitude of the current was obtained from $B_z(r)$ using the Biot-Savart equations [7]. The critical value of the persistent current was reached when $B_z(r)$ became independent of the applied magnetic field. This technique allows one to distinguish between the magnetic field due to the circulating persistent current and that due to magnetic vortices trapped in the the ring's bulk (see Ref. [8, 9] for more technical details). This cannot be achieved by standard magnetization or four-probe measurements of the critical current.

Six MgB_2 thin film samples were studied. These films were deposited on sapphire substrates. Films S1-S3 were prepared at Postech using a two-step method; the detailed process is described elsewhere [1, 10]. Amorphous boron films were first deposited on (1102) sapphire substrates at room temperature by pulsed laser deposition. The boron film and high purity magnesium were then inserted into a sealed

Table A.1: Parameters that describe MgB_2 films S1-S6. T_c^p is the transition temperature, determined as the temperature at which the supercurrent disappears (see Ref. [11]), J_c is the critical current density at 10.5 K, and d is the thickness. Reduced T_c^p of sample S3 is caused by aging in air at room temperature for two years [12]. PLD+PA is the pulsed laser deposition followed by post annealing in a magnesium vapor. RF-MAG is the rf magnetron sputter deposition method.

Sample	T_c^p (K)	$J_c(10.5K)$ (A/cm^2)	d (μm)	Deposition Method
S1 (ring)	36.5	3.55×10^6	0.4	PLD+PA
S2 (ring)	35.0	3.00×10^6	0.4	PLD+PA
S3 (ring)	32.0	2.60×10^6	0.4	PLD+PA
S4 (ring)	29.5	9.64×10^6	0.4	RF-MAG
S5 (ring)	25.5	3.60×10^4	1.2	RF-MAG
S6 (disk)	20.5	1.42×10^4	0.6	RF-MAG

tantalum tube. The heat treatment was performed at 900°. The remaining three films S4-S6 were deposited on (0001) sapphire substrates using dc and rf magnetron co-sputtering techniques in high purity argon at 600°C from MgB_2/Mg and Mg targets. These films were post-annealed *in-situ* at the same temperature in a Mg flux. The properties of the films investigated such as T_c, J_c, thickness and deposition methods are summarized in Table A.1.

A.3 Experimental results and discussion

The experimental results are presented in Figures A.2 and A.3. The temperature dependence of J_c for all six MgB_2 thin films of T_c between 20.5 and 36.5 K is shown in Figure A.2(a), for temperatures between 10.5 K and T_c. $J_c(T)$ of films S4-S6, i.e. those with the lowest T_c, can be described by a function $J_c(T) \sim (T_c - T)^{3/2}$ at temperatures below $0.8T_c$ (see Figure A.2(b)). The temperature dependence of resistivity for films S5 and S6 with the lowest T_c is plotted in Figure A.2(c). The time dependence of the decay of the persistent current from the critical level was measured for four films S1 and S3-S5 over a time period of 1-10^4 seconds between 10.5 K and T_c. The decays are logarithmic with time. The decay rate S = d(lnJ)/d(lnt), which is a measure of the strength of the vortex pinning, is plotted in Figure A.2(d) as a function of temperature for four of the films. $J_c(T)$ of films S1-S3 exhibits an instability (suppression of the critical current density) at temperatures below 10.5 K; see Figure A.3(a) (the lowest temperature of the measurement was 7.8-8.0 K). This instability can be also seen in the measurements of the persistent current self-field (a magnetic field trapped at the ring's center) as a function of the applied external field (see Figure A.3(b)). The data reveal significant scattering in the magnitude of the trapped field at temperatures below 10.5 K but not at higher temperatures. We did not observe similar instability in films S4-S6 of lower T_c at temperatures down to 8 K.

We now discuss possible reasons for the changes in $J_c(T)$ observed in MgB_2 films. There are two major mechanisms that determine the magnitude of J_c and its tem-

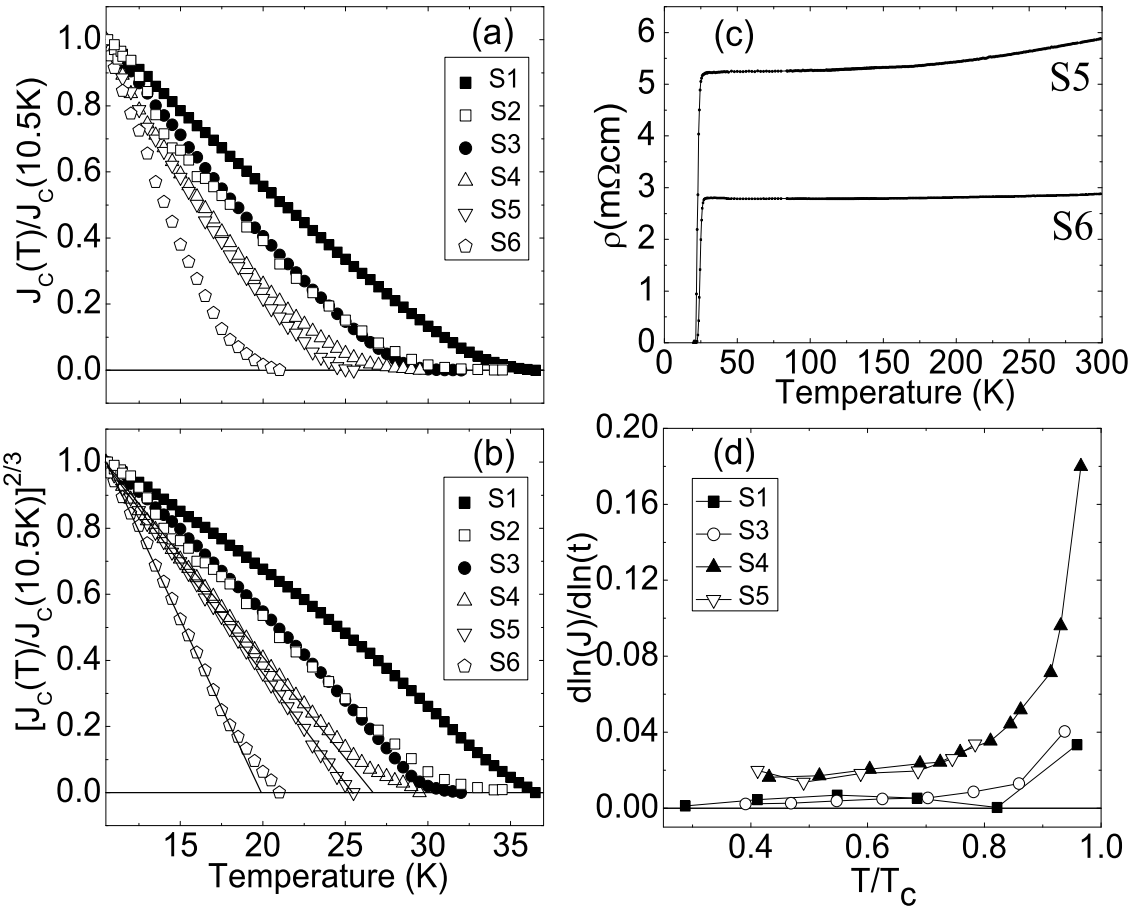

Figure A.2: a) Critical current density $J_c(T)$ normalized to J_c at 10.5 K, as a function of temperature for all films S1-S6. (b) Temperature dependence of $[J_c(T)/J_c(10.5\text{K})]^{2/3}$ which shows a gradual transition of $J_c(T)$ to the Ginzburg-Landau-like temperature dependence (seen for films S5 and S6) with a decreasing T_c. (c) Temperature dependence of resistivity for films S5 and S6. (d) Persistent current dissipation rate $S = d(lnJ)/d(lnt)$ as a function of the normalized temperature T/T_c for MgB_2 films S1 and S3-S5.

perature dependence, namely magnetic vortex pinning and non-uniform (percolative) flow of the current. We believe that the temperature dependence of J_c of the form $J_c(T) \sim (T_c - T)^{3/2}$ and the non-observation of a low temperature instability, found in MgB_2 films S4-S6 of low T_c, is the result of changes in the microstructure of these films caused by magnesium deficiency. In such Mg-deficient films, the supercurrent is expected to flow (percolate) through filamentary paths. Kresin [13] suggested that the temperature dependence of the critical current in quasi-one dimensional superconducting wires (filaments) with a reduced order parameter should be described by a Ginzburg-Landau-like dependence of $J_c(T)$ ($\sim (T_c - T)^{3/2}$). Hence, our observation that $J_c(T) \sim (T_c - T)^{3/2}$ over a wide temperature range in films S5 and S6 is attributed to percolative flow of supercurrents. Additional insight can be gained by analyzing the resistivity in the *normal* state within the context of Halbritter's model [14, 15]. According to this model, the change in the resistivity of the percolative film $\Delta\rho(T)$ over a certain temperature range is proportional to the change of the resistivity $\Delta\rho_{sc}(T)$ of a MgB_2 single crystal over the same temperature range. The proportionality constant is the percolative geometrical factor p whose value depends on the length and the width of the percolative paths. By using $\rho(T)$ for our samples (see Figure A.2(c)) and the $\Delta\rho_{sc}(T)$ from Ref. [16], we estimated that p is in the range of 130-150 and 12-15 for films S5 and S6, respectively. (The value of p varies slightly with the temperature range used in the calculation.) The corresponding percolation parameter $R_{bn}/a_j = \rho(0) - p\rho_{sc}(0)$ (where R_{bn} is the island/grain boundary resistance and a_j the mean weak-link distance) has values around 5 $m\Omega cm$ and 2 $m\Omega cm$ for

S5 and S6, respectively. Film S5 appears to be more percolative than S6. This film also exhibits a $J_c(T) \sim (T_c - T)^{3/2}$ dependence over a wider temperature range than S6. By contrast, films with the highest T_c (including S1) have $\rho(T)$ similar to that of a single crystal, with $p \simeq 2$ and $R_{bn}/a_j \simeq$ 1-2 $\mu\Omega cm$. Interestingly, the effect of vortex pinning appears to be minimal since no correlation between the magnitude of J_c and our decay rate S has been observed. For example, the shapes of the curves of the normalized J_c versus temperature are very similar (see Fig. A.2(a,b)) for films S4 and S5, as are their decay rates (see Fig. A.2(d)), yet the low temperature values of J_c for these two films differ by more than two orders of magnitude.

The instability (suppression of the supercurrent) seen in films S1-S3 below 10.5 K (Figure A.3(a)) is consistent with the magneto-optical observation of a dendritic-like flow of vortices in similar films at the same temperatures [3, 17, 18]. Our data confirm that this instability (dendritic flow) arises during applying or removing the external applied field. The magnitude of the persistent current generated in a ring fluctuates when the external magnetic field is applied and subsequently turned off at temperatures below 10.5 K (see Figure A.3(b)). The instability, i.e., reduction in the magnitude of the persistent current, does not occur if a persistent current is first produced at temperatures higher than 10.5 K and the film subsequently cooled below this temperature (see the arrow in Figure A.3(a)). Fluctuations of the magnitude of the persistent current could be caused by an irregular dendritic flow of vortices into and out of the ring. On the other hand, no instabilities have been observed in magnesium deficient films S4-S6 at temperatures down to 8 K, the lowest temperature

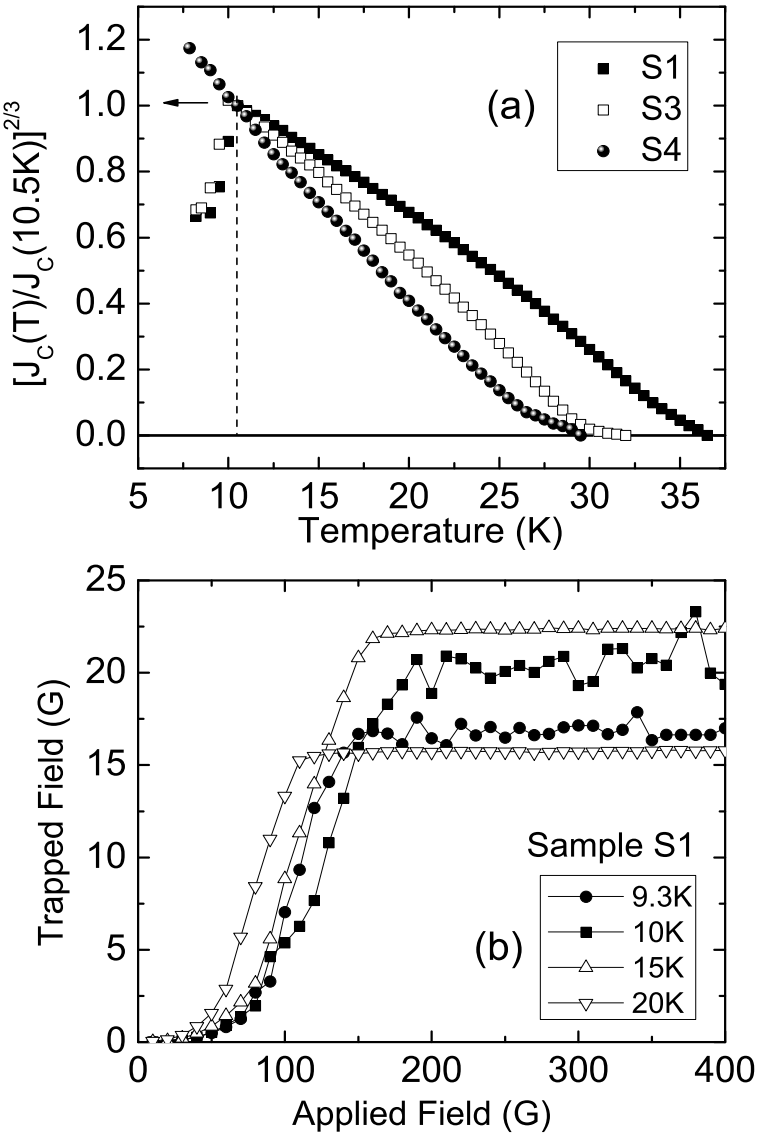

Figure A.3: (a) Temperature dependence of $[J_c(T)/\ J_c(10.5\text{K})]^{2/3}$ for films S1, S3 and S4. Suppression of the persistent current is seen in films S1 and S3, both with T_c larger than 32 K, below 10.5 K. If the persistent current is first generated in the film at 10.5 K and then cooled below 10.5 K, there is no change in the magnitude of the persistent circulation current, as indicated by the arrow. (b) Dependence of the persistent current self-field (field trapped at the ring's center) measured for film S1 as a function of the applied external magnetic field. The saturation value of the trapped field is proportional to the magnitude of the critical current density. The trapped field is unstable at 9.3 K and 10 K, but not at temperatures above 10 K.

of the measurement. This suggests that the non-observation of the instability in these films is related to changes in the film's microstructure. In order to confirm this, film S3 ($T_c^p = 32$ K) was annealed several times in vacuum at a temperature of 600°C. This type of annealing makes the film Mg-deficient. Measurements of $J_c(T)$ followed each thermal treatment [19]. We found that a drop in the transition temperature by 2.0 K reduced J_c ten times, shifted the onset of the instability below 8 K and converted the entire temperature dependence of J_c to a Ginzburg-Landau-like dependence of $J_c(T) = J_{co}(T_c - T)^{3/2}$. Hence, an increasing disorder in the film is most likely responsible for the observed changes in the transport properties of this sample.

In MgB_2 with large J_c and T_c (for example without grain boundaries), the sudden drop of the persistent current density J_c at temperatures below 10.5 K (i.e., the instability region) is related to an ultra-fast magnetic flux flow. This flow likely originates on the surface defects and spontaneously propagates into the sample along dendritic paths. This is consistent with the magneto-optical observations (Ref. [3]). In MgB_2 with grain boundaries J_c is also limited by the grain boundary junctions. Vacuum annealing of film S3 leads to Mg deficiency and consequently to more disorder, causing a filamentary flow of the current and a large reduction of $J_{cJ} \sim \Delta/eR_{bn}$ (an increase of R_{bn}). In this case the persistent current density below 10.5 K is reduced by two effects, the dendritic flux flow (which might be enhanced by disorder) and the drop of the grain boundary J_{cJ}. However, in film S3 where large disorder has been introduced we do not observe the instability. We believe this indicates that J_{cJ} has been reduced below the minimum value of the dendritic-flux-flow-suppressed critical

current density in the instability region.

A.4 Conclusion

In summary, we investigated the effects of disorder and a dendritic-vortex-flow-instability on the temperature dependence of the critical persistent current $J_c(T)$ in MgB_2 films with different T_c. An increasing disorder, likely due to Mg deficiencies, shifts the onset of instability to lower temperatures and converts $J_c(T)$ into a Ginzburg-Landau-like dependence. Hence, Mg deficient MgB_2 films may be preferred in applications that require high critical currents at low temperatures.

Bibliography

[1] H. J. Kim, W. N. Kang, E. M. Choi, M. S. Kim, K. H. P. Kim, and S. I. Lee, Phys. Rev. Lett. **87**, 087002 (2001).

[2] A. Gupta, J. Z. Sun, C. C. Tsuei, Science **265**, 1075 (1994).

[3] T. H. Johansen, M. Baziljevich, D. V. Shantsev, P. E. Goa, Y. M. Galperin, W. N. Kang, H. J. Kim, E. M. Choi, M. S. Kim, and S. I. Lee, Europhys. Lett. **59**, 599 (2002).

[4] R. G. Mints and A. L. Rakhmanov, Rev. Mod. Phys. **53**, 551 (1981).

[5] F. L. Barkov, D. V. Shantsev, T. H. Johansen, P. E. Goa, W. N. Kang, H. J. Kim, E. H. Choi, and S. I. Lee, Phys. Rev. B **67**, 064513 (2003).

[6] H. M. Christen, H.Y. Zhai, C. Cantoni, M. Paranthaman, B.C. Sales, C. Rouleau, D. P. Norton, D. K. Christen, and D. H. Lowndes, Physica C **353**, 157 (2004).

[7] H. Darhmaoui, and J. Jung, IEEE Trans. Appl. Supercond. **13**, 2897 (2003).

[8] J. Jung, K. H. Chow, M. Egilmez, and A. Welsh, Appl. Phys. Lett. **87**, 262506 (2005).

[9] H. Darhmaoui, and J. Jung, Phys. Rev. B **57**, 8009 (1997).

[10] W. N. Kang, H. J. Kim, E. M. Choi, C. U. Jung, and S. I. Lee, Science **292**, 1521 (2001).

[11] The values of T_c and $J_c(T)$ estimated using persistent circulating supercurrents are usually lower than those determined from magnetization or resistivity measurements. In magnetization measurements additional fields trapped by sample defects contribute to the magnetization (persistent supercurrent bypasses these defects). In resistivity measurements the measured value of $J_c(T)$ and T_c is usually overestimated due to the non-zero voltage criterion. Due to these reasons persistent current measurements typically give T_c about 1-2 K lower than that obtained by other methods. $J_c(T)$ measured using persistent currents could be several times less than that obtained from other measurements.

[12] K. A. Yates, Z. Lockman, A. Kursumovic, G. Burnell, N. A. Stelmashenko, J. L. MacManus, and M. G. Blamire, Appl. Phys. Lett. **86**, 022502 (2005).

[13] V. Z. Kresin, LBNL, private communication.

[14] J. Halbritter, Phys. Rev. B **48**, 9735 (1993).

[15] J. Halbritter, Mat. Res. Soc. Symp. Proc. **EXS-3**, EE9.9.1 (1993).

[16] Y. Eltsev, S. Lee, K. Nakao, N. Chikumoto, S. Tajima, N. Koshizuka, and M. Murakami, Phys. Rev. B **65**, 140501 (2002).

[17] A. V. Bobyl, D. V. Shantsev, Y. M. Galperin, A. F. Olsen, T. H. Johansen, W. N. Kang, and S. I. Lee, Physica C **408-410**, 508 (2004).

[18] A. F. Olsen, T. H. Johansen, D. Shantsev, E. M. Choi, H. S. Lee, H. J. Kim, and S. I. Lee, Phys. Rev. B **74**, 064506 (2006).

[19] A. I. Mansour, M. Egilmez, K. H. Chow, and J. Jung, unpublished.